Experimental Investigation of Self Sustained Lean Premixed Prevaporized Combustion Instabilities by Phase Averaged Laser Diagnostic Techniques

by
Jacob Edwin Gerken Temme

A dissertation submitted in partial fulfillment
of the requirements for the degree of
Doctor of Philosophy
(Aerospace Engineering)
in The University of Michigan
2012

Doctoral Committee:

Professor James F. Driscoll, Chair
Professor Volker Sick
Associate Professor Luis P. Bernal
Assistant Professor Matthias Ihme

For Stephanie,
Yours.

ACKNOWLEDGEMENTS

My completion of this thesis in due in no small part to the support I received from a number of people. First and foremost, I owe a large debt of gratitude to my advisor Professor James F. Driscoll. Not only did he provide me with the opportunity to study at the University of Michigan with it's world class experimental facilities, but he has always been ready to give sound advice and insight into problems encountered in the lab and theoretical discussions.

The group of students in the Propulsion and Combustion Engineering Laboratory when I arrived at graduate school taught me the ins and outs of the lasers and combustors. Sulabh Dhanuka showed me how to run my burner and helped me learn PIV and PLIF. I would like to thank Andy Lapsa for his help in the design and manufacture of my current flame tube. Adam Steinberg, Alex Schumaker, and Danny Micka also were very welcoming and helpful as I began my studies.

I also need to thank the current students of the lab without whose help the experiments would not have been run. Since the experimental setup require three operators, I am deeply indebted to Matt Fotia, Patton Allison, and David Rosenberg for all the times they ran the heater and pushed buttons for me. They have also been indispensable in discussing the meaning of the latest lab results. Two other individuals greatly assisted me in the daily operation of the experiment, Nansi Xue and Justin Bass.

The support staff in the Aerospace department helped me immeasurably. This

experiment would not have run at all without the efforts of Eric Kirk who kept the air pump running and fulfilled many last minute air requests. Terry Larrow's highly skilled craftsmanship in the machine shop created the many parts and modifications needed to keep the experiment functional and allow all of the different measurement techniques to operate with this combustor. Tom Griffin, Chris Chartier, Dave McLean and Aaron Borgman also provided technical and operational support. Denise Phelps guided me through all of the paper work and bureaucracy of being a grad student allowing me to spend more time taking and analyzing my data.

I would like to thank General Electric Aviation for their generous funding which was provided through the GE-USA program.

Throughout this whole process I have been blessed to have the encouragement of my family. My parents and siblings have consistently been an important source of strength and support. Finally, I am most indebted to my loving wife Stephanie. She has always been a steady pillar during the many frustrations of broken lab equipment and noisy data sets. She has also equally been a welcome companion at the moments of triumph over the vagaries of a temperamental experimental rig. I would not have finished this thesis in the same amount of time at the same mental state without her efforts.

TABLE OF CONTENTS

LIST OF FIGURES

Figure

LIST OF TABLES

Table

NOMENCLATURE

Symbols	
A	Cross-sectional Area
C	Spatial Cross-correlation Coefficient
c	Speed of Sound
f	Frequency
L	Length
$\dot{m}$	Mass Flow-rate
P	Pressure
R	Specific Gas Constant for Air
RI	Rayleigh Index
T	Temperature
U	Flow Velocity
V	Volume
Greek	
γ	Ratio of Specific Heats
ϕ	Equivalence Ratio of Jet-A and Air
τ	Time Lag
ζ	Non-dimensional Ratio of Fuel Fraction Split Between Pilot Flows
Subscript	
b	Burning
rms	Root Mean Square
Superscript	
$'$	Fluctuation Around the Mean Value
$\bar{}$	Mean Value
$<>$	Spatially Averaged Value Near Jet Base
Acronyms	
FOV	Field of view
ICCD	Intensified charge-coupled device camera
LES	Large eddy simulations

LIF	Laser-induced fluorescence
PAH	Polycyclic aromatic hydrocarbons
PLIF	Planar laser-induced fluorescence
PSD	Power spectral density
TAPS	Twin annular premixed swirler
UMGTC	University of Michigan Gas Turbine Combustor

CHAPTER I

Introduction

1.1 Background

One of the most promising technologies being pursued in the aircraft engine industry, as well as the land based power industry, is Lean Premixed Prevaporized (LPP) combustion. This method of combustion hold great promise in reducing emissions in gas turbine engines. Pollutant emissions are increasingly becoming a main factor in aircraft engine design. In addition to needing to satisfy current legal pollutant emission limits, the engine must be able to meet future regulations which propose to lower these limits further. One of the main regulated groups of pollutants from aircraft engines is the oxides of nitrogen, NO and NO_2, which are abbreviated as NO_X. At typical cruise conditions up to 90% of the regulated emissions from a twin engine airplane is NO_X [32]. NO_X emissions at low altitudes contribute to smog and acid rain and emissions at high altitude contribute to ozone depletion. The Committee on Aircraft Environment Protection (CAEP) has established guidelines for the regulation of NO_X emissions with increasingly lower targets over the last decade and a half [43] , [69]. Therefore any practical new engine design must be able to meet proposed pollution targets while still maintaining or increasing its efficiency.

1.2 Lean Premixed Prevaporized Combustion

Lean premixed (LP) or lean premixed prevaporized (LPP) combustion refers to methods for burning gaseous or liquid fuels respectively. In this type of combustion, a large fraction of the fuel is premixed with the air flow and burned in a lean fashion. The remaining fuel is often burned as a rich pilot flame to stabilize the lean main flame. Additional flame stabilization is often provided by using swirling air flow. With this method of combustion, peak temperatures are lowered and the thermal NO_X is reduced.

However, LPP combustion presents many challenges which arise from the same aspects that lead to performance benefits. In general LPP systems operate near the lean blowout limit to maximize the NO_X pollution reduction benefits. This leaves the system prone to incipient blowout and flashback into the premixed reactant stream. Additionally, the complex geometries of the LPP injectors can give rise to other instability modes. Swirl stabilized systems inherently have a vortical structure which precesses around the centerline, creating a unique cyclical source that can couple with combustion acoustics. These combustion instabilities can cause significant damage to gas turbines as well as cause engine blowout [34].

1.3 Combustion Instabilities

Complex combustion systems are susceptible to instabilities which can lead to engine blowout and catastrophic failure of engine components [44]. Combustion instabilities have been studied for over 80 years [7]. In 1928, Chamberlain and Rose photographed "flicker" in a Bunsen burner with a variety of gaseous fuels and noted a 10 Hz oscillation with the speed of the downstream motion occurring slower than the speed of the return upstream motion. In 1949, Park [48] described incipient blowout

instabilities in a propane flame and attempted to determine instability limits based on hot-wire anemometer data. Both of these results are still relevant in current investigations into combustion instabilities and are discussed further in the current study.

Combustion instabilities occur when the heat release from the flame oscillates in phase with and amplifies a naturally occurring acoustic frequency mode in the combustor. These natural modes can be broken into three major types: organ tone, Helmholtz, and convective-acoustic modes. The heat release from combustion can vary in time due to a number of factors, but two factors which often lead to instability are equivalence ratio oscillations and flame front area oscillations.

1.3.1 Organ Tone Instabilities

Organ tone oscillations refer to standing waves in a pipe. The boundary conditions of the system determine if a half or quarter wave mode exists. For most combustion systems, the quarter wave boundary conditions best represent the combustor, as seen in Figure 1.1, with a frequency given by Equation 1.1.

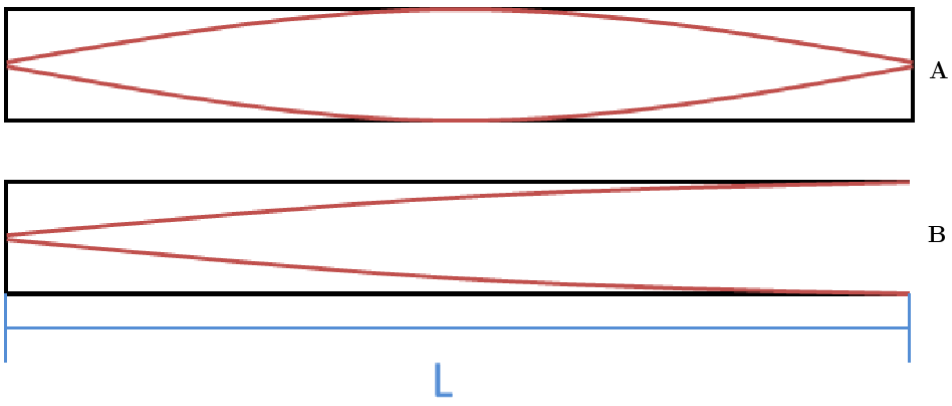

Figure 1.1: Typical organ tone mode with A- Two closed ends resulting in a standing half wave mode and B- A closed and an open end resulting in a standing quarter wave mode

$$f = \frac{C}{4L} = \frac{\sqrt{\gamma RT}}{4L} \tag{1.1}$$

The length scale of the quarter wave mode is most often the length of the combustion chamber. However, it can also be the length of the entire engine system [17]. These lengths are on the order of meters and can result in low frequency pressure oscillations under 100 Hz. Rodriguez-Martinez et al. [59] report a half wave mode over the length of a whole combustor resulting in a 41 Hz in a natural gas LP swirl burner. They also conclude that these pressure fluctuations result in flow reversal.

1.3.2 Helmholtz Resonators

Helmholtz resonance occurs in a large volume that is connected to a smaller neck region. The mass of air in this neck region oscillates and compresses the fluid in the volume. It is commonly experienced as the tone heard when blowing over the mouth of a bottle. The physics of a Helmholtz resonator are analogous to a simple harmonic oscillator system, as shown in Figure 1.2. The volume of air acts as a spring on the mass of air in the neck.

$$f = \frac{c}{2\pi}\sqrt{\frac{A}{VL}} \tag{1.2}$$

In combustion experiments, the facility can operate like a pair of coupled Helmholtz resonators [39], [55]. Pritz developed low order combustion models for an LES simulation based on coupled Helmholtz oscillators representing the plenum and combustion chamber sections of an experiment shown in Figure 1.3. This models predicts a 25 Hz oscillation in agreement with experimental results.

Uhm and Acharya [72] also observe combustion instabilities which are associated with a Helmholtz resonance of the upstream cavity. They measured pressure and

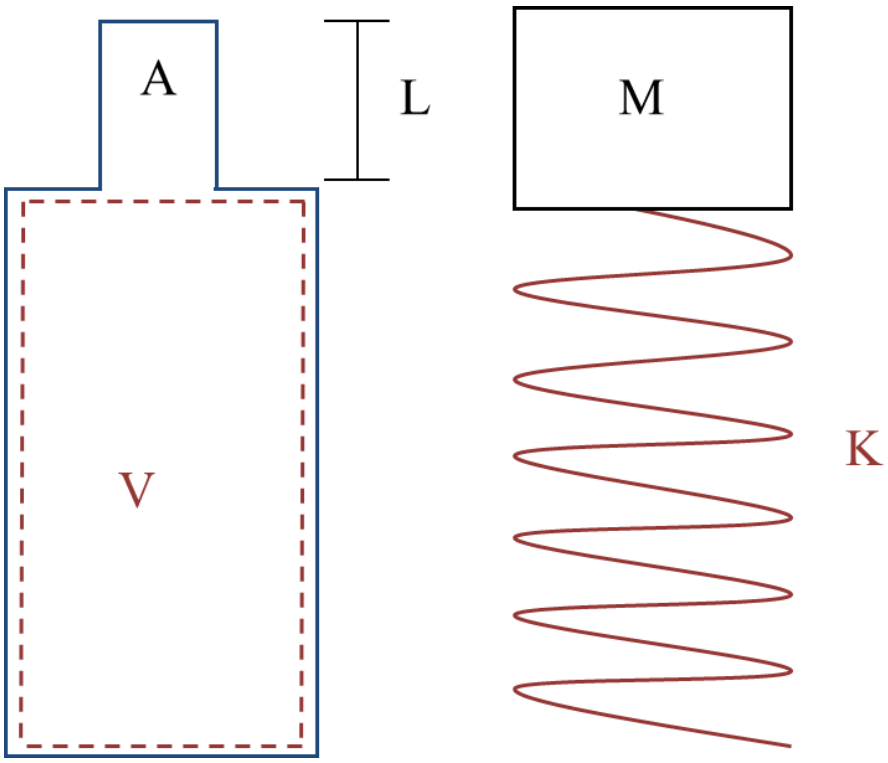

Figure 1.2: Description of Helmholtz resonator and analogous simple harmonic oscillator

phase locked CH* images during combustion instabilities under 50 Hz in an liquid ethanol burner. Methods to control these instabilities were investigated based on information from the Rayleigh Index measurements.

Helmholtz mode oscillations are also investigated in realistic LPP combustors using natural gas and liquid diesel fuels [10] using understanding from mathematical models [52].

Research in Meier's lab at DLR Stuttgart has reported instabilities in a gaseous LP swirl burner which are governed by a Helmholtz like bulk mode [67]. However, they also note that the precessing vortex core (PVC) plays a role in setting the observed frequency [68].

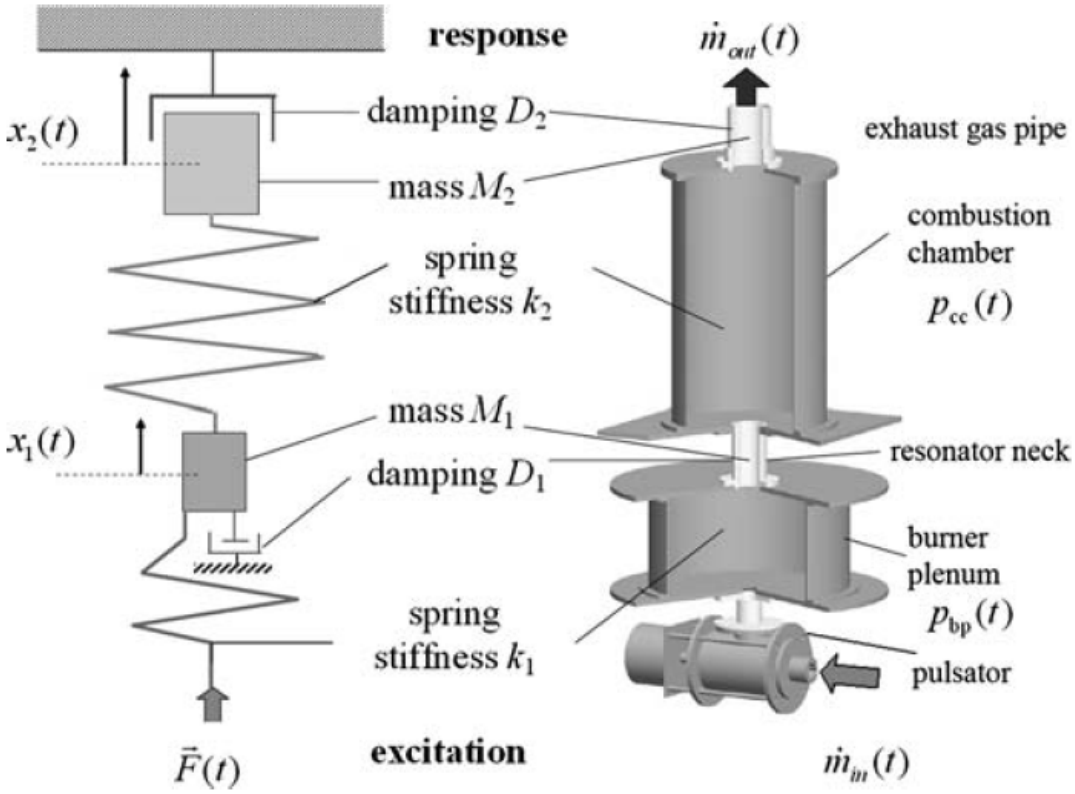

Figure 1.3: Description of coupled Helmholtz oscillator model for a generic combustion experiment from [55].

1.3.3 Convective Acoustic Instability

Convective Acoustic instabilities are oscillations which occur when a flow disturbance is convected downstream at the flow velocity U and then couples with an acoustic mode of the system. As such the characteristic frequency is given by Equation 1.3 where L is the characteristic length scale.

$$f = \frac{U}{L} \tag{1.3}$$

Yu et al. [76] show convective acoustic instabilities in their dump combustor and show that there is a standing wave in the upstream plenum with shedding vortices

in the combustion chamber.

Bernier et al. [3] also report convective acoustic modes in a swirl stabilized LPP burner using liquid heptane fuel. They find that having counter-swirling air flows results in equivalence ratio oscillation amplification and co-swirling air flows results in flame surface area changes through vortex rollup.

1.3.4 Other Instability Mechanisms

Several other instability mechanisms are presented in various works which are relevant to the current work. de la Cruz García et al. [11] ran liquid Jet-A fueled LPP combustor and observed low frequency instabilities that they ascribe to spray characteristics and time lags in droplet evaporation. Li and Gutmark [33] also report spray characteristics as the driver for instabilities in their liquid Jet-A LPP swirl burner.

Near lean blowout limits, an instability known as incipient blowout occurs. Huang and Yang [22] describe this instability in their LES computation and experimental data set. In this burner, the flame cyclically flashes back into a corner recirculation zone.

In swirl stabilized flames, the swirling air flow creates a central pair of vortical structures. These structures precess in the circumferential direction of the combustion chamber. The frequency of the precession is roughly linear with flow rate.

$$f \alpha \dot{m} \tag{1.4}$$

This precessing vortex core (PVC) can directly effect the local mixing, flame surface area, and heat release of the flame, thereby impacting the combustion instabilities [70]. Steinberg et al. [68] showed that the observed combustion instability

and the frequency of oscillation of the centroid of heat release are both affected by the PVC frequency.

1.3.5 Equivalence Ratio Oscillations

One of the main sources of amplification of the natural acoustic modes is termed equivalence ratio oscillation. Perturbations in the incoming fuel or air streams result in local changes in the equivalence ratio which result in oscillating heat release rates. When these oscillations occur in phase with the acoustic pressure waves amplification occurs [35]. These types of oscillations were first studied in the fuel feed systems of liquid fueled rocket engines. It was found that they can be avoided by having the fuel feed pressure higher than twice the combustion chamber pressure [2].

In more recent work, this type of instability has been seen in gas turbines. Weigand et al. [73] conducted 3D high speed LDV, OH* chemiluminescence and Raman scattering on a gaseous LP swirl burner. They found that the air flow rate was varying with time creating an equivalence ratio oscillation but did not identify the acoustic mode that it amplified.

In the system researched by Cohen, equivalence ratio oscillations are experimentally found to amplify the Helmholtz frequencies in the combustor[29].

Lee et al. [31] directly measured the equivalence ratio oscillations in a natural gas LP burner. They found that while the equivalence ratio instability forced the pressure and heat release oscillations at the system's natural frequency, the equivalence ratio instability occurred at a higher harmonic frequency.

1.3.6 Flame Surface Area Oscillations

Another source of heat release oscillations is the variation in the flame surface area. This can be due to interactions between the flame and vortices shed upstream

resulting in acoustic convective instabilities, or due to flame surface destruction at an obstruction in the flow ([18], [64]). As discussed previously, Bernier et al.[3] observed instability amplification from this mechanism when investigating co-swirling air flow LPP burners.

1.4 NO_X Pollution

NO_X formation in a combustion system is primarily from three sources: thermal NO_X, prompt NO_X, and fuel bound NO_X. Of these, thermal NO_X is by far the largest [28]. The thermal NO_X or Zel'dovich mechanism produces NO_X through three main reactions:

$$N_2 + O \rightleftharpoons NO + N \tag{1.5}$$

$$O_2 + N \rightleftharpoons NO + O \tag{1.6}$$

$$N + OH \rightleftharpoons NO + H \tag{1.7}$$

These reactions rely on high temperatures to provide enough energy to start the first reaction and as such they generally occur at temperatures above 1700K. Thus a major strategy to reduce the thermal NO_X is to reduce peak temperatures below this value and/or to limit the residence time above these temperatures.

1.5 Related Previous Work

Combustion instabilities have been widely studied. Main efforts in the area have been led by the labs of Candel, Lieuwen, Meier, Santavicca, Dowling, and Gutmark. The greater majority of the work has been done with gaseous fuels. Table 1.6 is a list of the previous relevant studies; in all cases laser diagnostics were applied to understand combustion instabilities in swirl flames. The four studies listed beneath the present work were done with liquid fuel and the last four were done with gaseous

fuels. Notice that of the four that were done with liquid fuels, only two used realistic fuel injectors (Li/Gutmark [33] and Bernier/Candel [3]). The other two (Garcia et al. [11] and Uhm and Acharya [72]) used a university designed liquid fuel injector. All four of these liquid fuel studies were done at atmospheric pressure with no valve downstream to choke the flow, so their open-ended experiments tend to create a quarter resonance that may not be realistic of an engine, since the end of an engine combustor is not open to the atmosphere.

Candel has looked at many side dump combustors with vortex shedding instabilities [54]. In general for side dump combustors, convective acoustic instabilities are found which are amplified by flame area oscillations due to flame vortex interaction [40, 61]. Additionally, his lab has conducted numerous studies on control of combustion instabilities and pressure oscillations [6, 53]. Boudy et al. [4] investigated non-linear triggering and mode switching between the different types of instabilities present in a single burner. Durox et al. [19] also look at the Rayleigh Criterion and its application to unconstrained systems, with specific interest in a Helmholtz resonator in the plenum and how it interacts with the flame and Rayleigh Criterion. Schuller et al. [65] investigated flame response decoupling between the plenum and combustion chamber acoustics and found that a geometric coupling index could dictate if the flame locked into a specific mode out of a set of acoustic parameters.

Lieuwen has been instrumental in describing equivalence ratio oscillations and how this mechanism is related to the onset and growth of combustion instabilities [35, 36]. However, most of this work is only pressure or pressure and chemiluminescence measurements. Additionally, Lieuwen generally finds equivalence ratio oscillations based on fuel feed line fluctuations. Cho and Lieuwen developed a model for Laminar flames which describes how the equivalence ratio oscillations affect heat release, flame

speed and flame surface area [8]. Lieuwen found that for self-excited combustion oscillations, the pressure traces exhibit phase shifting due to random noise as the number of cycles grows [37].

Meier has taken highly detailed measurements with high speed PIV and PLIF and characterized the interaction of the PVC and the Helmholtz frequencies of the burner [41]. The observed pressure instabilities correspond to frequencies which are determined by the difference between the PVC frequency and the Helmholtz mode [68, 67].

Santavicca has done work with the center of heat release, and Rayleigh index plots. Kim et al. [27] used information from experimental measurements of heat release to create a spatially distributed flame transfer function. Additionally, his lab has investigated self excited instabilities in both equivalence ratio oscillation and vortex shedding/flame surface area destruction modes [26, 31]. The lab has also looked at how these combustion instabilities affect the formation of NO_X pollution [66].

Ann Dowling has contributed significantly to the modeling and theory of combustion instabilities and also instabilities in of the engine as a whole system not just combustor section [16, 17, 45]. Kato et al. [25] created an improved model for equivalence ratio oscillations which allows the flame to move creating spatial distributions of heat release. Macquisten and Dowling [38] investigated low frequency oscillations in afterburner geometries experimentally and developed theoretical models.

Gutmark has studied a very similar burner, called the Triple Annular Research Swirler (TARS) [33]. Fureby et al. [21] ran both experiments and LES models of the TARS injector and found that the precessing vortex core created the dominant instability. Gutmark has also conducted many studies on control of combustion

instabilities [46, 50] with particular interest in control of vortex shedding instabilities [63, 77]. Paschereit and Gutmark studied vortex flame instabilities and developed mini-vortex generators which reduced both high and low frequency oscillations as well as reducing NO_X emissions [51]. Yi and Gutmark have also developed a model which predicts the onset of combustion instabilities by calculating damping ratios in real time [75].

The stable aspects of the burner studied in this dissertation were previously investigated by Sulabh Dhanuka [12, 13, 15]. The main focus of that work was to characterize the reacting, stable conditions using PIV and flame front measurements from PLIF of formaldehyde.

In terms of liquid fuels four studies are highly relevant. In the first, Uhm and Acharya [72] studied a swirl stabilized burner using liquid ethanol fuel. They only took pressure and chemiluminescence measurements and determined that the combustion instability was due to a Helmholtz mode of the plenum.

In the second, de la Cruz García et al. [11], working with Ann Dowling, ran a liquid Jet-A fueled LPP combustor and observed low frequency instabilities that they determined to be a half wave mode of the plenum and a three quarter wave mode of the combustion chamber. They ascribe the flame coupling with these acoustics to spray characteristics and time lags in droplet evaporation. They measured pressure, CH* chemiluminescence and particle droplet anemometry of the fuel spray.

In the third study, Bernier et al. [3] in Candel's lab researched a LPP swirl stabilized burner using liquid heptane fuel. This burner used a slightly simplified realistic fuel injector and swirler setup. They recorded pressure and CH* chemiluminescence. They found a quarter wave mode instability of the combustion chamber that was either of two modes depending on if the air swirlers were counter- or co-swirling.

The first was amplification by a flame surface area oscillation through flame vortex interaction for co-swirling flow. The second was amplification through equivalence ratio oscillations in the fuel line for counter-swirling flow.

In the fourth study, Li and Gutmark [33] operated the experiment most similar to the current work. Using a very similar LPP swirl stabilized fuel injector also provided by GE, they studied combustion instabilities at atmospheric pressures using liquid Jet A fuel. They determined that fuel feed line based equivalence ratio oscillations were amplifying a quarter wave mode of the combustion chamber.

1.6 Uniqueness of the Current Work

The current study differs from the previous works in a number of ways as detailed in Table 1.6. While numerous studies have been conducted in the field of combustion instabilities, none combine advanced diagnostics with self excited oscillations in a realistic geometry with liquid fuels. The studies which are most similar to this thesis are the second and third entry on the table conducted by Li and Gutmark [33] and Bernier et al. [3] respectively. However, neither study measured the flow field velocities or ran at elevated pressures. Furthermore, neither study made an attempt to verify the proposed geometric acoustics by systematic variation of the setup.

Additionally, this study differs from many previous efforts in that the system exhibited self sustained oscillations which needed to be identified, rather than designing a burner which has a predominant type of acoustics and investigating how the flame forcing couples with this acoustic mode. This study provides crucial information about how the findings of small scale burners with a single, forced response relate to the larger scale systems in industrial applications. The current work determined that the instability was created by the geometry of the fuel injector, whereas the

other studies listed all found the instability to be a function of the upstream plenum or combustion chamber geometries.

The present work addresses the important question: which of the five known sources of combustion instabilities dominates when a realistic fuel injector is used? Previous studies have shown that the following five mechanisms can create instabilities within simple laboratory-scale, gaseous-fueled "unit-physics" swirl burners: (a) periodic precession of the vortex core [68] [5] , (b) unsteady liftoff and flashback of the flame base [3] [12], (c) "puffing" of the air supply system that creates periodic vortex rings [76], (d) the time delay introduced by the droplet burn time [11] [20], and (e) Helmholtz resonance within the air or fuel supply [72] [71]. The present work identified the source of combustor “growl” for a commercial multi-swirl injector that was operated at realistic engine idle conditions (Jet-A liquid fuel, realistic mass flow rates, elevated pressures and preheated air temperatures). Because a real injector is used, the present work has engine-like levels of vortex shedding, swirl, recirculation zone strength, spray properties, and flame geometries, all of which can play a role in combustion instabilities.

Study	Liquid Fuel	Realistic Fuel Injector	Elevated Chamber Pressure	Phase Averaged or High speed Velocity	Phase Averaged or High speed Chemiluminescence	Vary Geometry	Self Excited	Type of Acoustic	Type of Flame Coupling
Current Study	Yes	Yes	Yes	Yes	Yes	Yes	Yes	HH	ERO
Li/Gutmark	Yes	Yes	No	No	OH* PL	No	Yes	QW	Fuel Line ERO
Bernier/Candel	Yes	Yes	No	No	CH PL	Only injector	Yes	QW	ERO and VS
Garcia/Dowling	Yes	No	No	PDA	Yes	No	Yes	HW	Possibly Spray
Uhm/Acharya	Yes	No	No	No	CH PA	No	Yes	HH	Not stated
Meier	No	Yes	No	Yes	Yes	No	Yes	HH	ERO
Lieuwen	No	No	No	No	Yes	No	Yes/No	HH	ERO
Santavicca	No	Yes	Yes	No	Yes	No	No	QW	ERO
Candel*	No	No	No	Yes	Yes	Yes	Yes	CA/HH	ERO

Table 1.1: Comparison of related works and current study. CA=Convective Acoustic, ERO= equivalence ratio oscillation, HH= Helmholtz, HW=Half wave, PL= phase locked, PA= phase averaged, QW= quarter wave mode, VS= Vortex Shedding

1.7 Thesis Goals

The goal of the current study is to investigate the combustion instabilities occurring in a realistic gas turbine system. The University of Michigan Gas Turbine Combustor (UMGTC) facility was modified to allow two similar commercial LPP fuel injectors provided by GE Aviation to be installed interchangeably. The experiments were run at elevated pressures (up to 5 bar) and preheat temperatures (up to 500K) with large air flow rates (up to 0.4 kg/s). These parameters correspond to engine idle and taxi. Full cruise conditions could not be achieved due to limitations in the pre-heating components of the experiment. The first objective of the study was to measure the instabilities occurring during the operation of the burner. The low frequency component of these oscillations can be especially damaging to gas turbines in operation. Therefore, the second objective was to investigate both very low frequency (less than 50 Hz) oscillations near incipient blowout and low frequency (less than 250 Hz) oscillations through the use of pressure field, high speed video and phase averaged particle image velocimetry. Finally, the third objective was to determine the mechanisms responsible for each type of low frequency oscillation.

1.8 Outline

Chapter 2 describes the experimental techniques and facilities used during this study. The modifications to the UMGTC are described as well as its operational procedure. The simultaneous high speed video and particle image velocimetry systems are described. Chapter 3 discusses the very low frequency oscillations found near incipient blowout conditions. Chapter 4 presents the results from the pressure field measurements. The main instabilities are characterized and the effects on these instabilities of varying physical parameters are discussed. Chapter 5 presents the

results for the simultaneous pressure and high speed video measurements. Several important quantities are measure from the video and provide information about potential instability mechanisms. Chapter 6 includes a mathematical analysis of the source of the low frequency instabilities. Chapter 7 presents the phase averaged PIV results. These data provide solid evidence for the cause of the low frequency combustion instability. Chapter 8 summarizes the main conclusions from the thesis.

CHAPTER II

Experimental Facilities

2.1 Experimental Facilities

2.1.1 University of Michigan Gas Turbine Combustor

The University of Michigan Gas Turbine Combustor (UMGTC) was modified in several ways for this work. A larger diameter fuel injector (GE GEnx TAPS) replaced the smaller diameter GE CFM TAPS fuel injector used by Dhanuka [15]. A rectangular glass flame tube was designed with input from GE to provide a larger field of view which includes the corner re-circulation zones. Most importantly a set of operating conditions was determined that provided a maximum intensity low frequency combustion instability commonly called "growl". New experimental methods were developed to obtain phase-averaged PIV data.

In order to mimic realistic gas turbine conditions, the University of Michigan Gas Turbine Combustor (UMGTC) was operated at high flow rates of pre-heated air with liquid Jet-A fueling. The main layout of the combustor is shown in Figure 2.1 and is nearly identical to the setup of the previous work [15]. Two major components are exterior to the lab: an air supply and an electrical heater. The air is supplied by an Ingersoll Rand compressor which pressurizes four large air tanks to about 12.4 MPa. At typical flow rates for the experiments this allowed for operation times of approximately one and a half hours. The air is preheated in the nearby the UM

Supersonic Combustion Lab by a 250 kW Hynes electric heater. The heater can produce preheat temperatures up to 550 K at the desired flow rates. The air is regulated down to 1.38 MPa before entering the heater, which sets the upper limit on flow rates possible in the UMGTC. In the Gas Turbine Combustor Lab the heated flow is metered with a custom built choked flow orifice from Fox Valve. The throat area of the orifice is 13.97 mm. As long as the upstream pressure is sufficiently high the mass flow rate through this orifice is then determined from Equation 2.1.

$$\dot{m} = \sqrt{\frac{\gamma}{R}\left(\frac{2}{\gamma+1}\right)^{\frac{\gamma+1}{\gamma-1}}}\frac{P_o A^*}{\sqrt{T_o}} \tag{2.1}$$

A choked flow orifice allows the mass flow rate to remain constant even with a changing combustion chamber pressure, which is vital for the instabilities that were studied. The mean combustion chamber pressure is set with a gate valve downstream of the combustor. The PIV seeding system is discussed in more detail in Section 2.4.

2.1.2 Combustion Pressure Vessel

In order to test the fuel injector at elevated pressures, a combustion pressure vessel was designed to contain the TAPS fuel injector and flame tube. A schematic of the pressure vessel and plenum is shown in Figure 2.2. The plenum is similar to the one used in a previous study [14], but the hole pattern on the plate was re-drilled to be symmetric and then partially covered to produce uniform flow, as shown in Figure 2.3. The pressure vessel was re-designed and differs from the previous work. It is still an 20.3 cm diameter schedule 40 stainless steel pipe rated to 10 bar. However, instead of three identical 12.7 cm diameter sight windows, optical access is provided by two 17.1 cm x 2.5 cm slot windows for the laser sheet and an 20.3 cm diameter circular observation window as seen in Figure 2.4. A 12.7 cm diameter pipe was

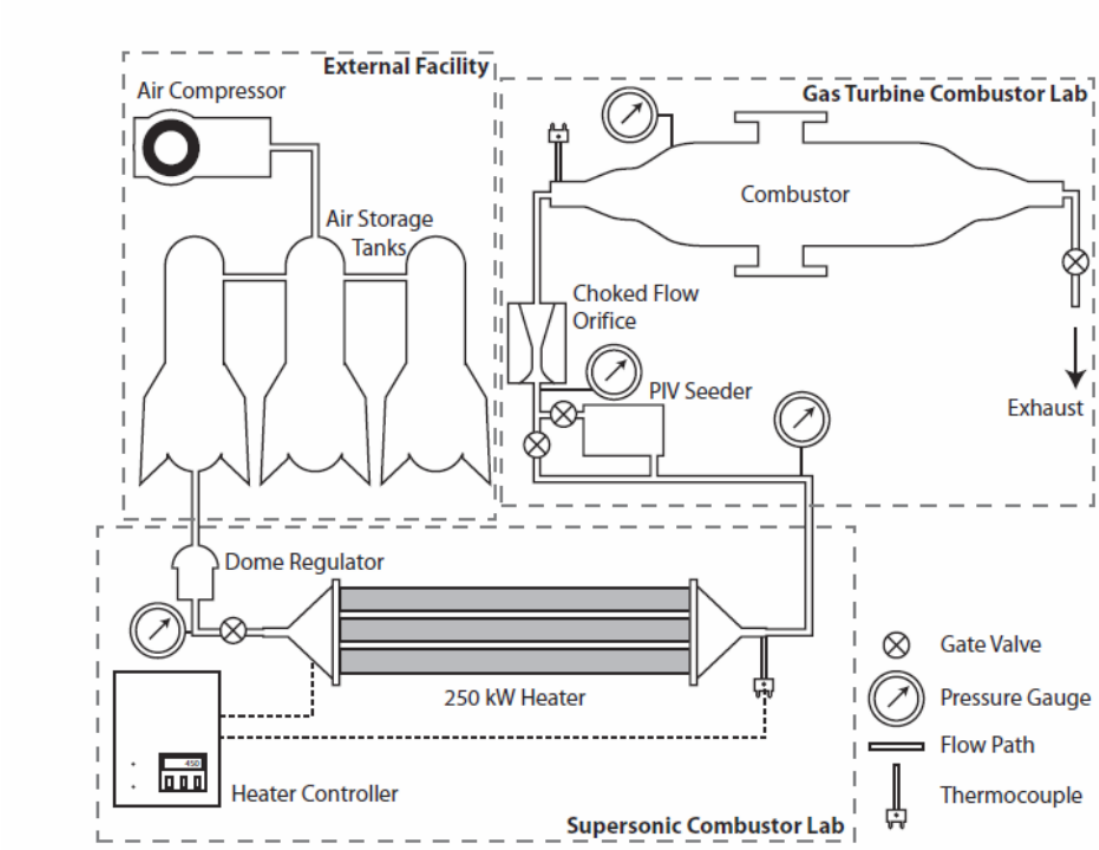

Figure 2.1: The air flow feeding system in the University of Michigan Gas Turbine Combustor Lab from the previous work [15] was also used for the current research. The only changes are to the pressure vessel itself.

fitted on the bottom of the vessel to allow access for the TAPS fuel injector and the fuel lines. A photograph of the experimental setup in use is shown in Figure 2.5. The test section is mounted on a rail system to allow easy access for cleaning the windows and altering the physical dimensions as discussed in Section 4.6.

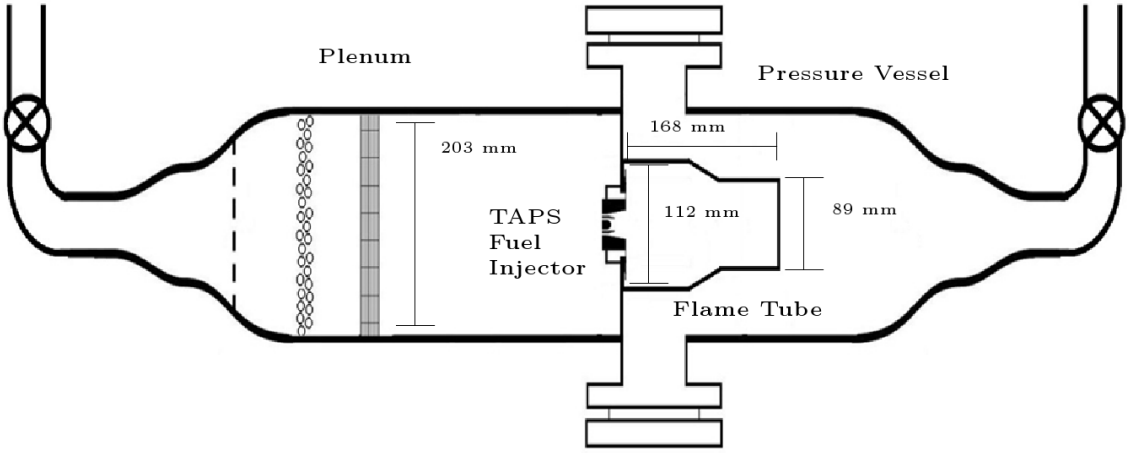

Figure 2.2: Plenum and Combustion Chamber. The plenum contains three levels of flow straightening devices: a plate with non-symmetric hole pattern, half inch marbles, and honeycomb. The pressure vessel has optical access on 3 sides.

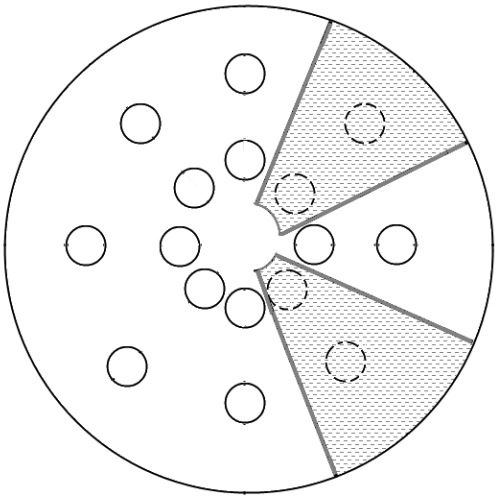

Figure 2.3: The flow straightening plate consisting of a plate with symmetric holes that have been selectively covered to produce uniform flow.

Figure 2.4: Photographs of the new pressure vessel from top and side views. Note the two laser slot windows and the 20.3 cm observation window. The new square flame tube is to the right of the second photograph.

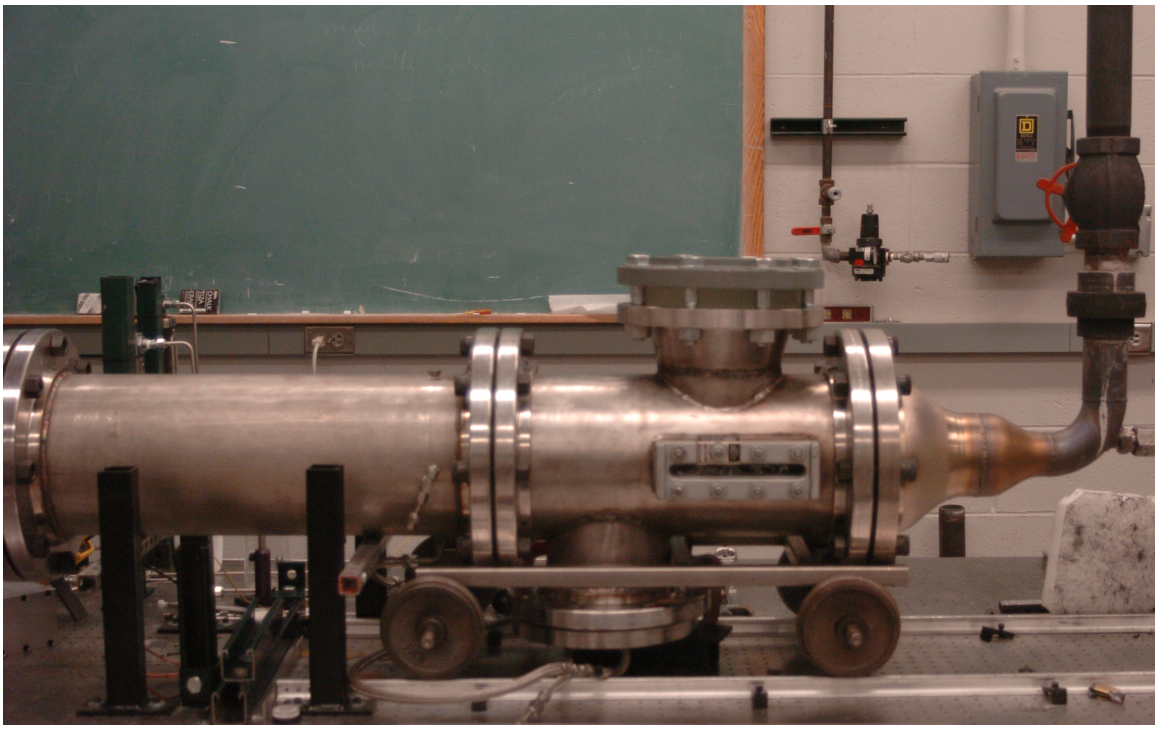

Figure 2.5: Photograph of experimental setup. The test section is mounted on a rail system on the optical table for mobility when cleaning and varying physical parameters.

Liquid Jet-A fuel supplied by AvFuel at the local airport was used for all of the experiments. Similarly to previous work [15], a pressure driven feed system was utilized, shown in Figure 2.6. A tank was filled with Jet-A and pressurized with nitrogen to about 750 kPa. Three calibrated rotameters allow for separate fueling rates for the two pilots and main fuel lines.

2.1.3 Fuel Injector and Flame Tube

The inner flame tube is substantially changed from the previous studies in the lab. The previous works utilized a cylindrical tube with air bypass to cool the liner. The current work uses a variable area tube with a rectangular cross section with no bypass air. Additionally, it is designed such that it provides 100% optical access. The previous combustor did not allow visual access to the corner recirculation zones

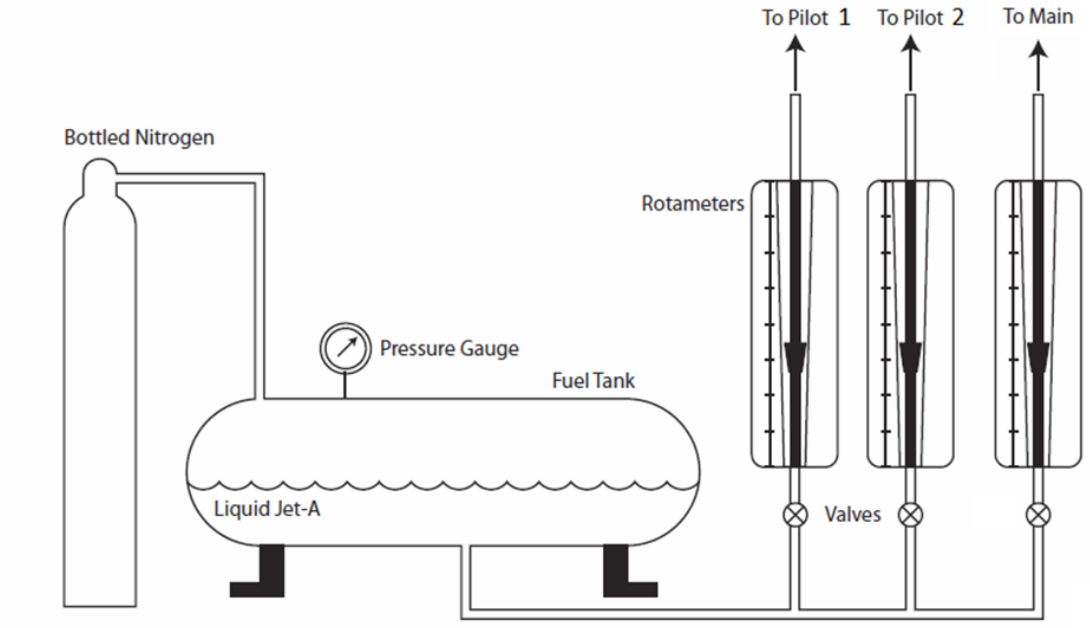

Figure 2.6: Fuel Feed System. Nitrogen pressurizes a tank to 750 kPa. Three rotameters allow independent control of the three fueling ports in the injector.

which play an important role in the observed instabilities. Photographs of the flame tube are shown in Figure 2.7. The flame tube was designed with interchangeable metal blanks and fused silica glass sections. In actual operation, metal blanks were used on one of the four sides to allow access for pressure probes and the hydrogen sparker with the remaining three walls having windows. In this flame tube there is no coolant air bypass, rather all of the air goes through the face plate with a small portion being redirected along the interior of the windows to form a thin film.

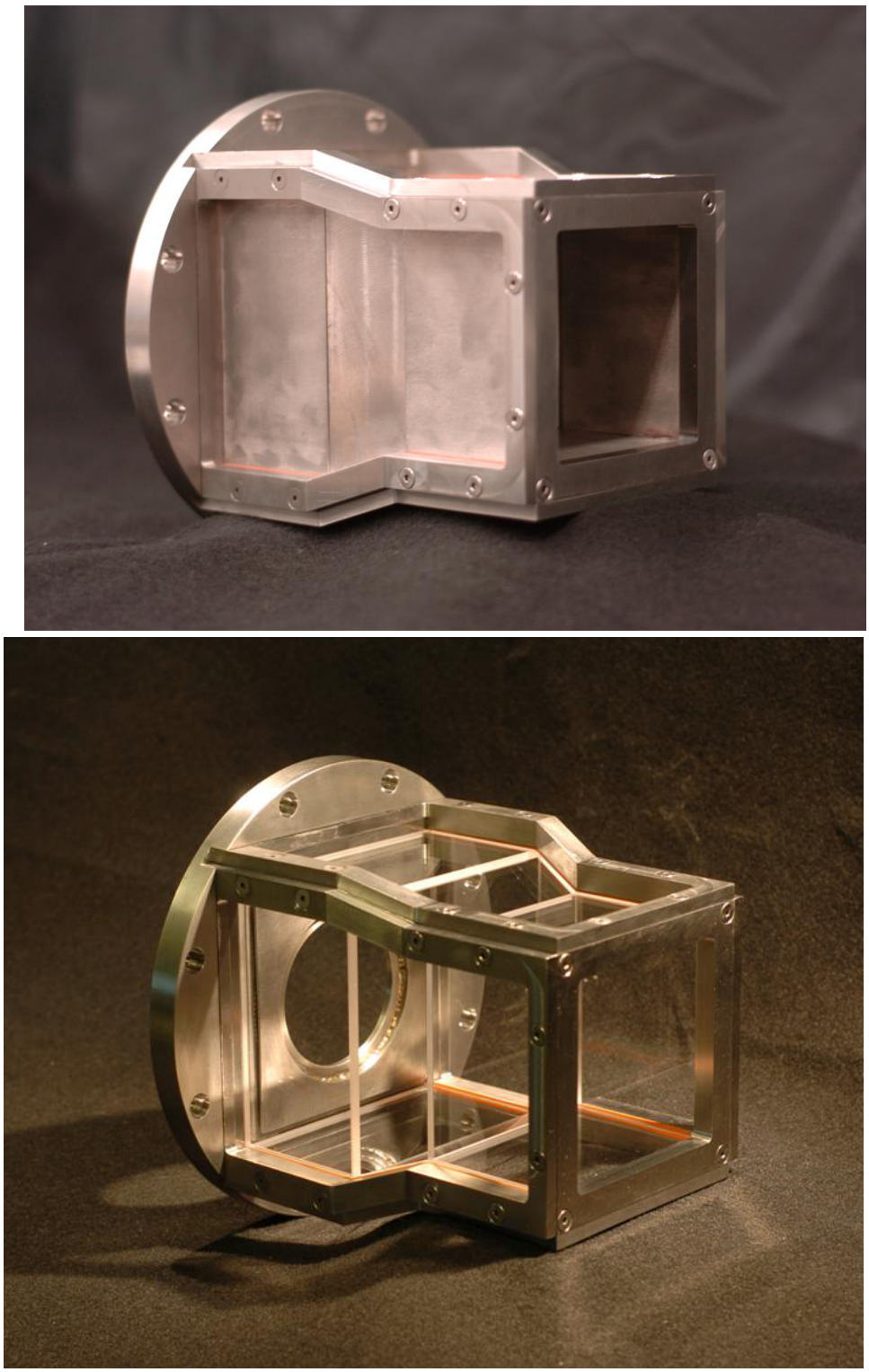

Figure 2.7: Photographs of the rectangular flame tube. Note the full optical access and the interchangeable metal blanks and window sections.

The LPP injectors are commercial models which stabilize the flame using two co-swirling annuli. Figure 2.8 shows a diagram of the main components of the injector design. The air flow is split into three streams which travel through swirl vanes to produce a co-swirling flow. Two of the streams are around the pilot fueling point and the third is the outer main stream. The main fuel is injected tangentially into the main air flow in order to increase droplet breakup and prevaporization of the liquid fuel. The main difference between the two fuel injectors used in this study is the addition of a second pilot fueling location in the injector used for the low frequency investigation. This secondary pilot is a co-axial injector around the primary pilot. Figure 2.9 shows the main dimensions for the separate annuli of interest in the fuel injector. A photograph of the injector mounted in the test section is shown in Figure 2.10. This photo is looking upstream from the exhaust and both the inner and outer swirlers are visible. Additionally the pilot fuel injectors can be seen at the center.

Figure 2.11 shows a simplified description of the flow structures that arise from the use of these LPP fuel injectors [15]. The swirling air flows create a primary recirculation zone (PRZ) in the center of the flow field. This low speed region helps the pilot flame to anchor. Two other recirculation zones form near the steps around the main air swirler. Nearer to the centerline is the lip recirculation zone (LRZ). This recirculation zone helps to stabilize the main flame by introducing hot combustion products from the pilot to the base of the main flame. The corner recirculation zone (CRZ) forms in the outer corners of the flame tube. This zone forms a crucial part of the incipient blowout phenomenon discussed in Chapter III. The premixed main flame is anchored in the shear layer which forms off the inner edge of the main air annulus.

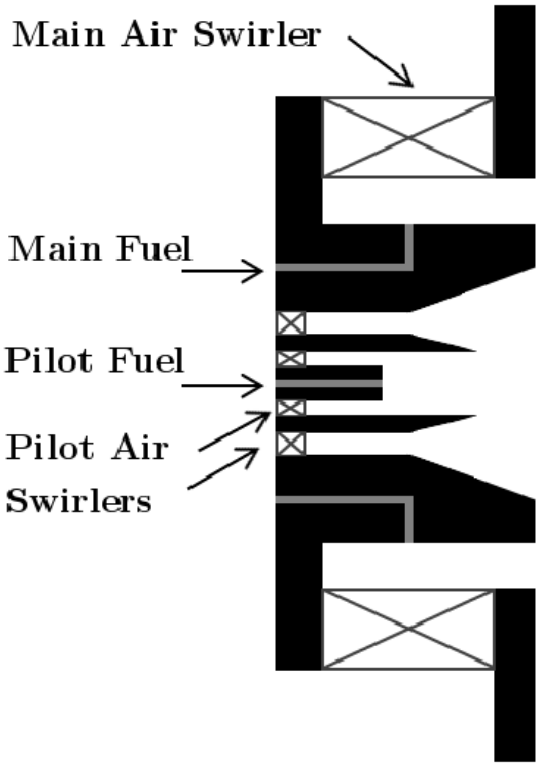

Figure 2.8: Diagram of the main components of the LPP fuel injectors used in this study.

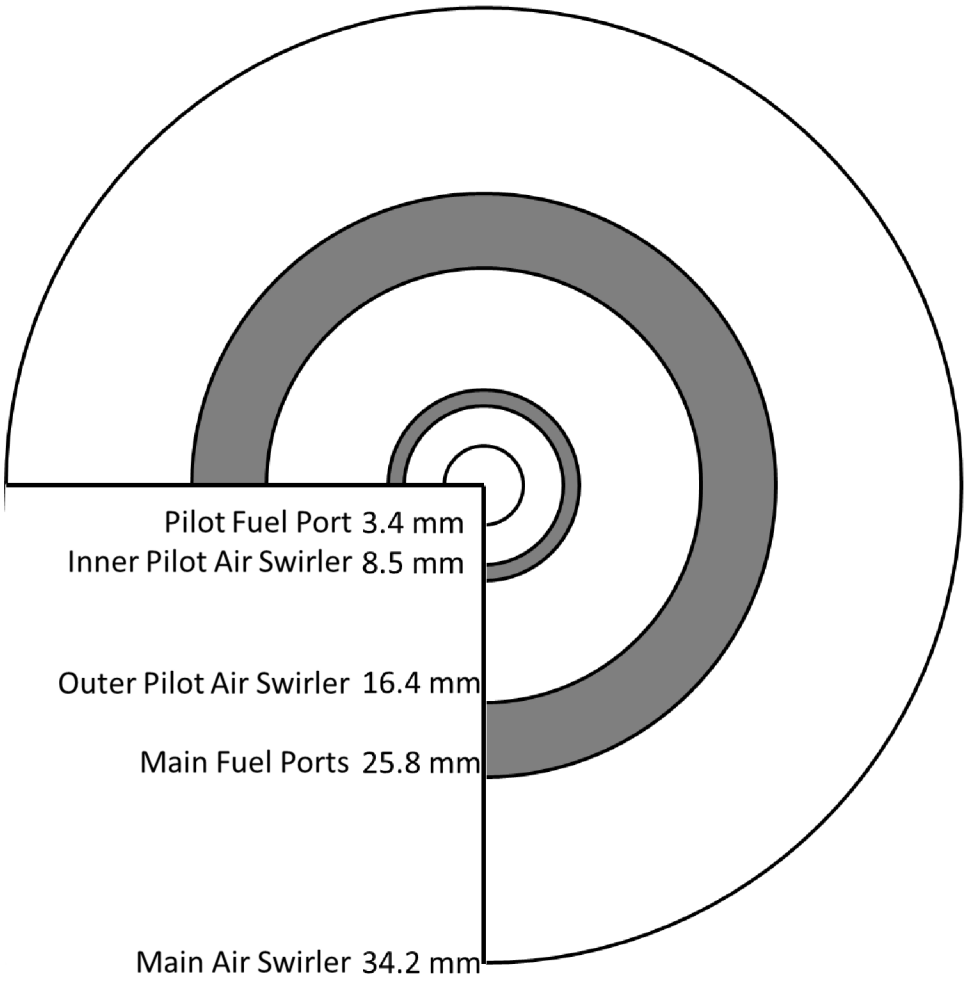

Figure 2.9: Dimensions of the main components of the TAPS annuli.

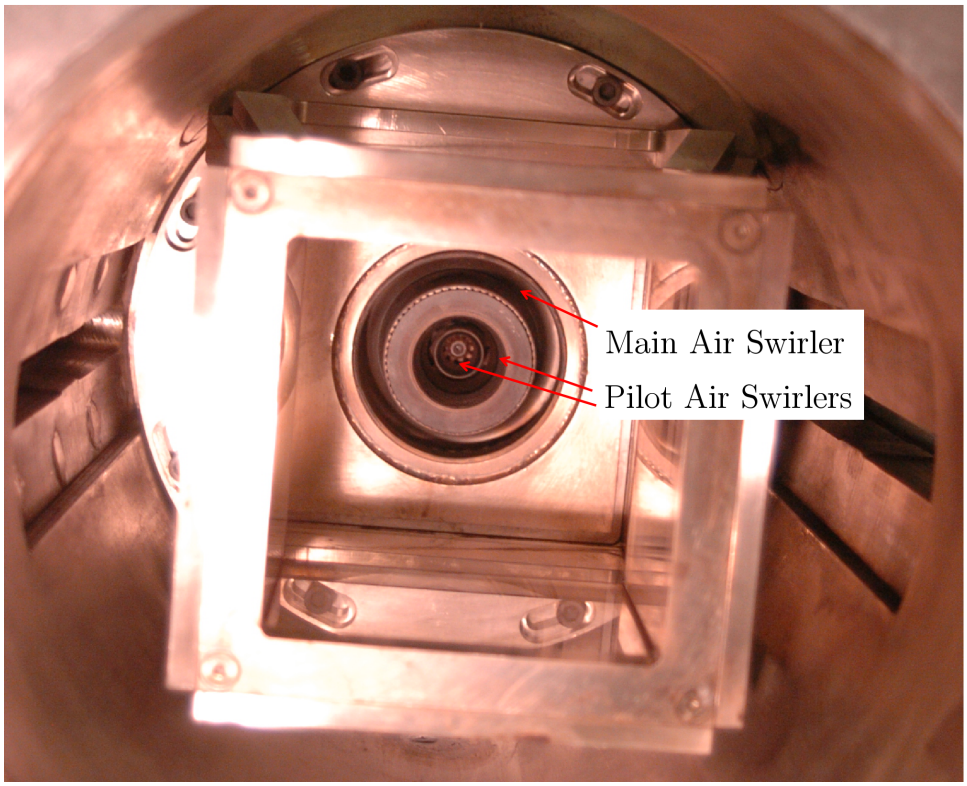

Figure 2.10: Photograph of the fuel injector mounted in the test section. The two air swirlers are visible as well as the pilot fuel injectors.

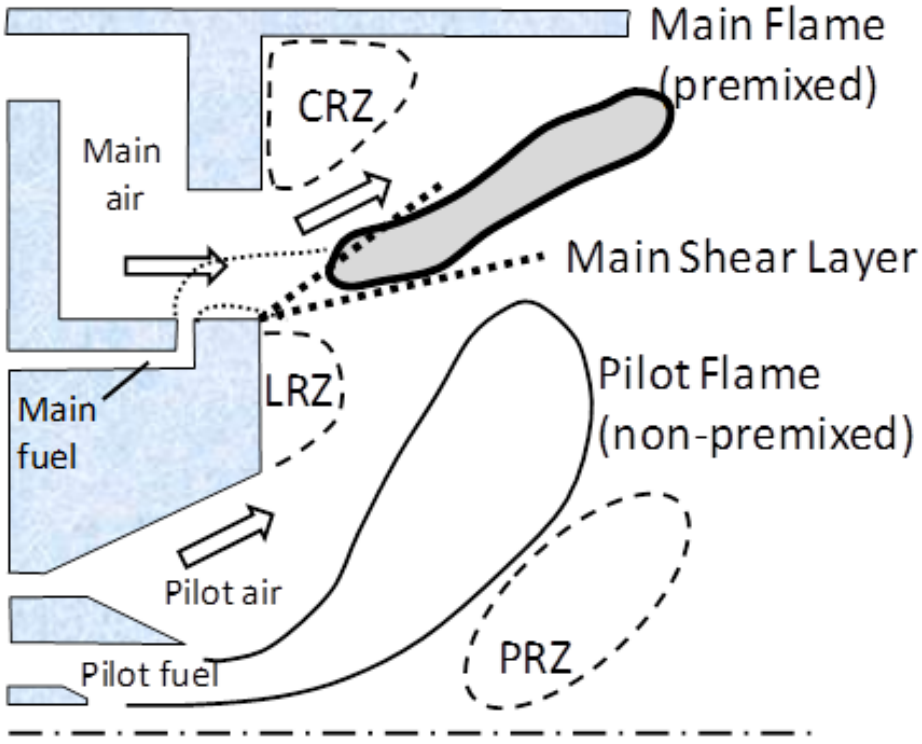

Figure 2.11: Illustration of the main flow features that arise in this fuel injector and flame tube combination. These features were measured using PIV and Formaldehyde PLIF and were published in [12]

2.1.4 Operation of the Combustor

Run times in the UMGTC were limited by the amount of compressed air in the exterior supply tanks. At typical flow rates and pre-run pressures of 12.4 MPa, these tanks provided enough air for one and a half hours of operation. However, that time was divided into three unequal parts: pre-heat, experiments with data collection, and cool down. Due to the large distance of piping between the electrical heater and the UMGTC, a general run took approximately 25 minutes to reach a stable pre-heat temperature of 460 K. Furthermore the cool down period at the end of the experiment took about 30 minutes to bring temperatures in the combustor and electrical heater to safe temperatures. This leaves approximately 35 minutes for actual data collection in any given run.

An experiment with this facility requires two to three people. While the controls for the electric heater are digital, the response time of the heater to reach a set point is very slow. Thus during the initial part of the pre-heat an artificially high set point is used which is relaxed as the temperature approaches the desired value. Additionally there is some amount of drift, typically +/- 6 K, which needs to be corrected in real time. Finally, the person in the Supersonic Combustion Lab can shut off both the air and the heater in case of emergency. The new flame tube and pressure vessel improved the ignition system from the previous work. Where previously a one meter long hydrogen torch had to be moved by hand into and out of the flame tube, in the new system this was replaced with a 10 cm long fixed position torch in the bottom of the pressure vessel shown in Figure 2.12. This allowed the UMGTC to be run by a single person in the room with the combustor, or when a second operator was present, more complicated types of data acquisition could be performed.

Similarly to the previous work [15] the hydrogen torch was ignited with an elec-

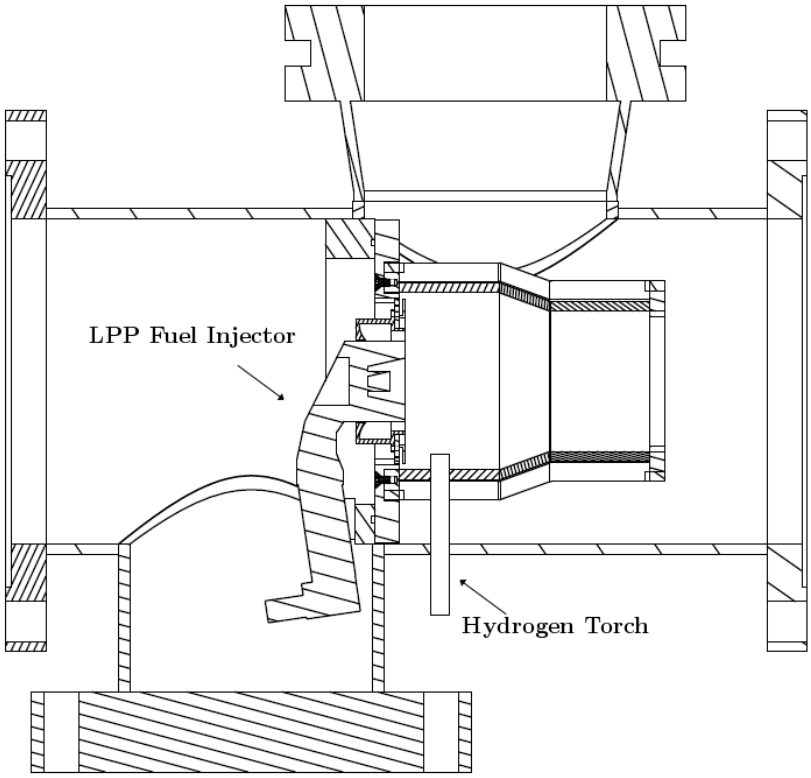

Figure 2.12: Improved hydrogen torch ignition source mounted in the bottom panel of the rectangular flame tube.

trical spark, which in turn lit the primary and secondary Jet-A pilots. After a period of a few seconds, self-sustaining combustion of the pilot flames was achieved and the hydrogen torch was turned off. The ignition of the flame typically caused a pressure rise in the combustor of approximately 17 psig. Therefore, the downstream valve was set such that the pressure before ignition was lower than the desired test condition and adjusted if needed after self-sustaining combustion was achieved.

Case	Pilot 1 Fuel Flow Rate	Pilot 2 Fuel Flow Rate	Main Fuel Flow Rate	Air Flow Rate	Temperature	Chamber Pressure
	g/s	g/s	g/s	g/s	K	bar
1	8.5	0.0	0.0	328	455	3
2	3.8	4.7	0.0	328	455	3
3	3.8	2.2	2.5	328	455	3
4	3.8	4.7	0.0	246	455	3
A	1.1	N/A	2.3	228	505	1
B	1.4	N/A	2.5	228	505	2
C	1.4	N/A	3.5	228	505	3

Table 2.1: Operating conditions for the two types of instabilities investigated.

2.1.5 Operating Conditions

Table 2.1.5 lists the operating conditions for the two instabilities types investigated in this study. The investigation into the low frequency oscillations started at conditions provided by GE listed as Cases 1, 2 and 3. Most of the subsequent runs were made at Case 4 that was produced the "maximum growl"; the Case 4 conditions were found to create a maximum power spectral density peak of the pressure fluctuations at 80 and 160 Hz.

A second instability type was called "Incipient blowout" and this condition led to large magnitude, very low frequency pressure oscillations. This type of instability was observed at Cases A, B and C.

2.2 Pressure Recordings

Pressure data was recorded using an Omegadyne PX01C1-100A5T pressure transducer which outputs a 0-5 V signal to a Waverunner 6000 oscilloscope. The transducer can measure up to 10 kHz frequency response, but experiences sharp drop off in gain after 1 kHz as shown in Figure 2.13.

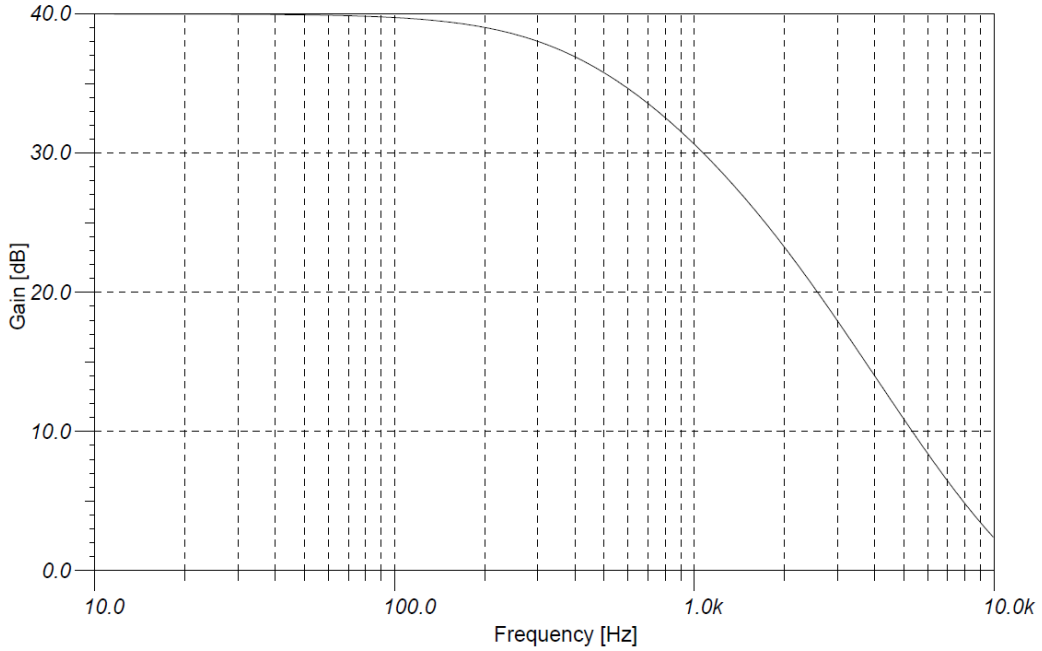

Figure 2.13: Frequency and Gain response of the pressure transducers.

For the majority of the test cases, the pressure was recorded at a single location at the end of the flame tube, which is denoted in Figure 2.14 as the main pressure port. For experiments with two simultaneous pressure readings a second Omegadyne PX01C1-100G5T was used. The difference in model number indicates that the second transducer is calibrated to output gauge pressure rather than absolute pressure. As discussed in Section 4.5 there is a constant phase angle offset between the plenum and combustion chamber and the pressure in each acts in a bulk mode, therefore the single pressure tap is sufficient to provide pressure field information for most of the cases. The pressure ports were located at the axial locations given in Table 2.2 where x=0 is the face of the injector.

Pressure Tap	Axial Location
	cm
1	11.43
2	10.16
3	5.08
4	2.54
5	-16.51
6	-52.07
7	-62.23
8	-77.47
9	-82.55
10	-87.63
11	-92.71

Table 2.2: Axial locations of pressure taps in the plenum and combustion chamber. X=0 is the face of the injector.

2.3 High Speed Videography

Broadband electromagnetic emissions from flames provide a qualitative measure of the spatial and temporal properties of the flame. The visible and near-visible portion of these emissions, which stem from the chemical reactions in the flame front, is termed chemiluminescence. In lean hydrocarbon flames these emissions originate from three radicals CH*, OH* and CO2* [30]. The CO2* emission is broadband over the 300-600nm range and is of higher intensity than the emission from the other two species which emit distinct narrow wavelengths of 309 nm and 431 nm for OH* and CH* respectively [23]. Samaniego et al. [60] and Najm et al. [47] conducted numerical simulations which showed that the OH* and CO2* chemiluminescence was highly correlated to the heat release of the flame. Samaniego further showed that there is a direct proportionality between the overall luminosity and the heat release. Lee and Santavicca [30] found the same correlation in a range of experimental results.

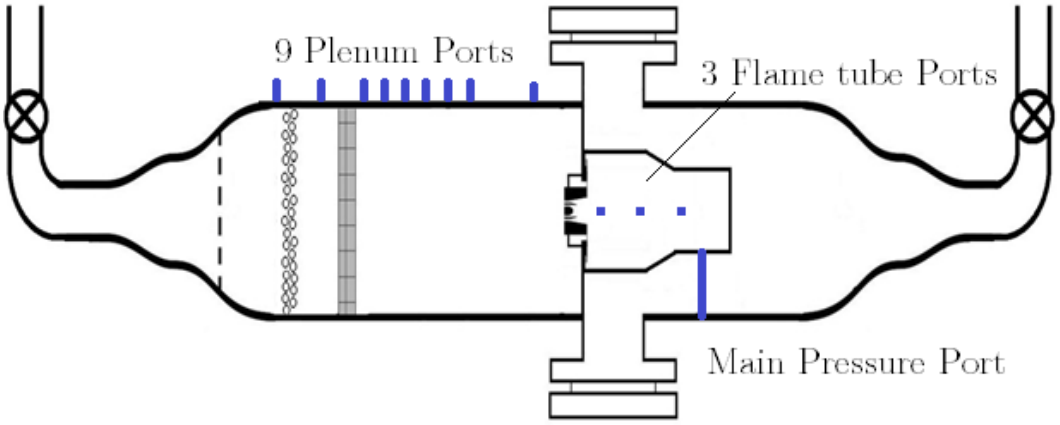

Figure 2.14: Locations of the pressure ports. For the majority of cases data were only recorded from the position at the end of the flame tube labeled main pressure port.

The large CO2* chemiluminescence signal is readily imaged by conventional cameras and can easily provide temporally resolved results with a high speed camera system. However, it is a line of sight measurement which renders the 3D flame structure in a 2D image and care must be exercised in interpreting the resulting data.

In this study, chemiluminescence was recorded by a Phantom v9.0 high speed CCD camera along with simultaneous measurements of pressure as described in Section 2.3. The camera was fit with a 90mm visible range (non-UV) lens and captured the entire flame tube through the 8" observation window. The use of this lens filtered out any OH* signal and the measured data was mostly CO2*. The video and pressure recordings were synchronized with a Stanford Systems DG-535 signal generator.

2.4 Simultaneous Particle Image Velocimetry, Videography and Pressure measurements

Particle Image Velocimetry (PIV) is a widely used diagnostic to record 2D or 3D velocity fields in a variety of flows. It was first utilized to measure velocity in a reacting flow with liquid Jet-A in the previous work in this burner [13]. The setup of the PIV system was nearly identical to that of the previous work and is discussed

here briefly and shown in Figure 2.15. Two laser beams were generated from two Nd:YAG lasers (Spectra Physics GCR-250 and Spectra Physics Lab-150) at 532 nm. These beams were overlapped and passed through sheet forming optics. Similar to the previous study [13] it was necessary to thicken the sheet slightly due to the highly swirling nature of the flow field of interest. In order to increase particle residence time and minimize particle dropout from the swirling flow, the sheet was focused outside of the field of view and expanded across it with an average thickness of about 1 mm. The PIV system was controlled and imaged using a LaVision Programmable Timing Unit v8.0 and LaVision ImagerPro 4M CCD camera. Similar to the previous experiment the flame luminosity presented a large problem while imaging the particles. A 532 nm, 2 nm FWHM band pass filter in line with a mechanical shutter was added to the system. The mechanical shutter reduced the exposure time of the second PIV frame from 100 ms to approximately 5 ms. However, at the much higher fuel flow rates, the chemiluminescence was brighter than the previous work. It overwhelmed the signal in the final two thirds of the combustor, and data were only recorded in the first 60 mm of the flame tube. This was sufficient as it was determined from the high speed video measurements that the majority of the flame motion occurred within this region. The Phantom camera was mounted above the test section at a 30 degree angle to the PIV camera. All three recordings were synchronized with a DG-535 signal generator.

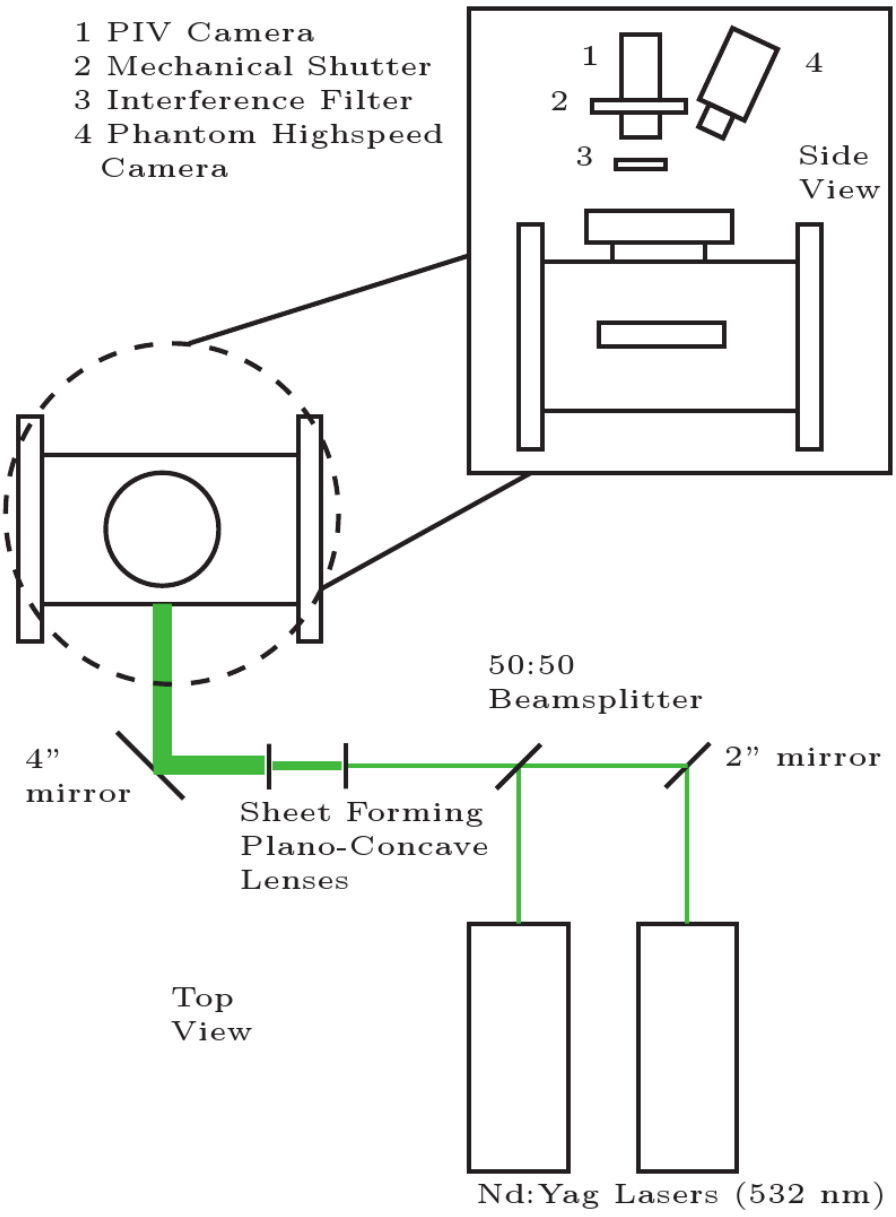

Figure 2.15: Experimental Setup for Particle Image Velocimetry

2.5 Error Analysis

An analysis was performed to estimate the errors associated with measurements of velocity (using PIV), pressure, gas preheat temperature, and mass flow rates of fuel and air. First, the velocity uncertainties are discussed. The PIV measurement technique is based on the assumption that the seed particles correctly track the flow field. Particles which are too large will not respond to large velocity gradients while particles which are too small will provide poor signal due to lower scattering of the laser light. Therefore particle size is chosen to maximize signal return while still tracking the flow. The ability of a particle to follow the flow field can be expressed by the Stokes number (2.2) which is defined as the ratio between a characteristic fluid dynamic response time of the particle, τ_p, and a characteristic time scale of the flow being measured, τ_f [42, 62, 74].

$$St = \frac{\tau_p}{\tau_f} \tag{2.2}$$

The particle's characteristic response time can be derived from the Stokes drag on a spherical particle as

$$\tau_p = \frac{\rho_p d_p^2}{18\mu} \tag{2.3}$$

where ρ_p and d_p are the density and the diameter of the particle respectively and μ is the dynamic viscosity of the surrounding fluid. The flow's characteristic time scale can be expressed as [42]:

$$\tau_f = 10\frac{\delta}{\Delta U} \tag{2.4}$$

where δ is the relevant flow length scale and ΔU is the largest velocity differences in the flow. Based on the previous PIV results [13], the largest expected velocity differences are on the order of 40 m/s and δ was taken as the smallest resolved length scale of 2 mm giving a fluid time scale of approximately $\tau_f \approx 60\ \mu s$. Clemens and Mungal [9] and Samimy and Lele [62] suggest values of St < 0.5 in order for the particle to correctly track the flow. This means the particle's characteristic time must be $< 30\ \mu s$.

As shown in 2.3 the density of the particle is an important factor in its response. An additional constraint on the choice of particle is that it must survive the high flame temperatures generated in the combustion chamber. A variety of metal oxides meet these constraints and have been widely used. In a previous PIV study, it was found that alumina (Al_2O_3) particles worked well in this combustor. These particles were nominally 0.5 μm in diameter, resulting in a characteristic particle time of 2.85 μs and a Stokes number of $5 * 10^{-3}$, both of which satisfy the conditions mentioned previously. Therefore the uncertainty associated with PIV particles not tracking the flow is estimated to be less than 0.05%.

The particles were seeded through the system shown in Figure 2.16 in order to ensure a homogeneous distribution. This seeder was used in the previous experiments and consists of a small chamber which is partially filled with the alumina. Bypass air from the main air supply line enters the chamber at the bottom and the seeded output air is then passed back into the supply line after the main control valve. A small needle valve is used to control the amount of seeding. This results in a large pressure drop creating a high velocity jet at the bottom of the seeder which serves to mix the seed into the air. The seeded air stream is mixed back into the main line before the choked orifice ensuring proper metering. The large distance from

the choked orifice to the combustion chamber and the flow straightening devices in between ensured homogeneous seeding levels in the flame tube.

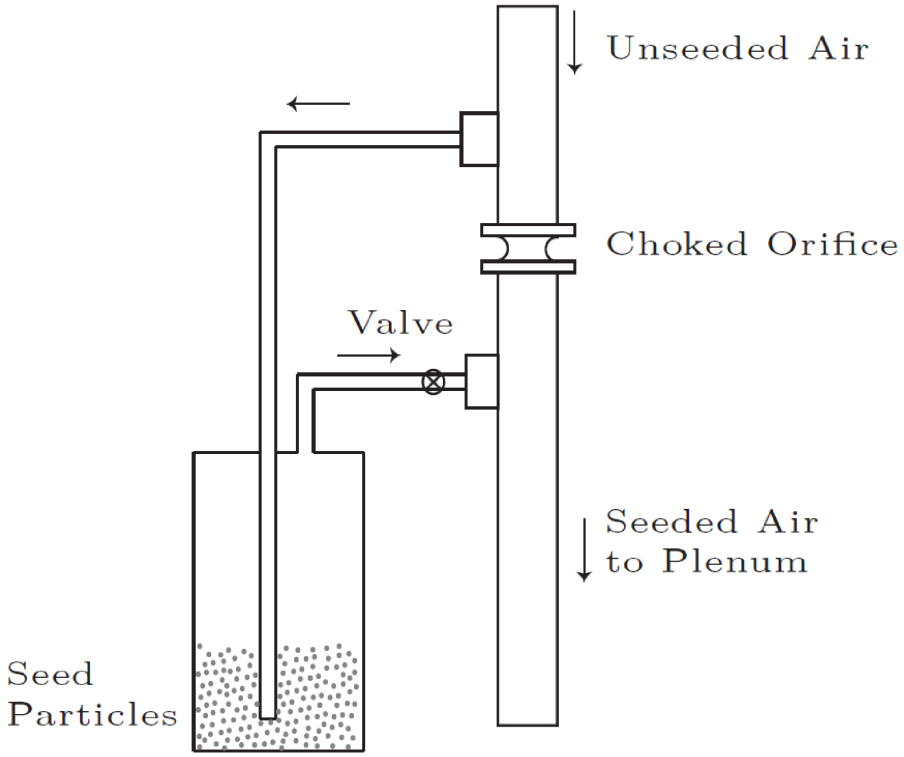

Figure 2.16: Seeding System for Particle Image Velocimetry

Errors in the PIV vector field calculations are calculated in depth in the previous PIV work on this burner [15] and a summary with updated values corresponding to the new experimental design is given here. The errors in calculating vector fields from PIV image pairs are mostly due to three sources: out of plane motion of the particles, uncertainties in peak finding, and displacement gradients within the interrogation window.

Because PIV images are taken at 90 degrees to the laser sheet, any out of plane motion will appear as an in-plane 2D motion. In the current experiment, the high degree of swirling air leads to large out of plane motion and required sheet thickening

as mentioned previously. A worst case error is estimated by assuming a particle at the outer edge of the field of view (r = 55mm) moves at the highest measured velocity of 35 m/s. With the camera located 460 mm away this leads to a worst case error of 0.3 pixels.

Uncertainties in peak finding arise when particles in the first PIV frame move out of the interrogation window in the second frame. This will bias the velocity to lower values due as slower particles are more likely to remain within an interrogation window. Raffel et al. [57] and Westerweel et al. [74] ran Monte-Carlo simulations and find a RMS uncertainty of 0.02 pixels. However, multi-pass processing with shifted interrogation windows will reduce this error and therefore this is a worst case estimate.

Displacement gradients which are smaller than the interrogation window also lead to underestimates of the velocity as higher velocity particles are less well correlated than lower velocity particles. Given a worst case gradient of 0.05 pixels/pixel, Raffel et al. [57] predict an error of 0.3 pixels. In total therefore, the worst case estimate for PIV uncertainty is 0.62 pixels or about 1.6 m/s. The mean velocities of interest range from approximately 20-50 m/s, so at the mid range of 35 m/s this corresponds to a worst case scenario of a PIV systematic uncertainty of 4.5%. From the phase averaged PIV data the r.m.s uncertainty is 5.6 % So the total worst case uncertainty in the PIV data is 7.2 %.

Incomplete vaporization of the fuel also introduces some error within the main and pilot jets. Since the fuel droplets are much larger than the PIV seed they will produce more Mie scattering and will bias the measurement toward the velocity of the droplet rather than that of the seed. However, the region where the velocity was measured is downstream of where most of the drops evaporated, so any error

associated with droplet bias is estimated to be less than 1%.

Air mass flow rate was measured using a choked flow orifice. It was also determined from the PIV information. The uncertainty in the first measurement is given by Equation 2.5 which describes the error contributions of each term in the choked orifice equation where $\Delta\dot{m}_a$ is the mean squared uncertainty in air mass flow rate.

$$\frac{\Delta\dot{m}_a}{\dot{m}_a} = \sqrt{(\frac{\Delta P_o}{P_o})^2 + (\frac{\Delta A^*}{A^*})^2 + \frac{1}{4}(\frac{\Delta T_o}{T_o})^2} \tag{2.5}$$

$\frac{\Delta P_o}{P_o}$ is 0.2 % since the smallest divisions on the gauge were quarter psi. The error in the choked flow area, $\frac{\Delta A^*}{A^*}$, is estimated to be 1 %. The temperature uncertainty, $\frac{\Delta T_o}{T_o}$, is 1 % based on the ability of the heater to maintain a set temperature. Therefore Equation 2.5 yields an uncertainty in the air mass flow rate of 1.4 %.

The air mass flow rate was determined from the PIV data using Equation 2.6. The error in this method of finding the air mass flow rate is given by Equation 2.7 where pressure and temperature uncertainties arise from the perfect gas law assumption in the density term.

$$\dot{m} = \rho\, U\, A \tag{2.6}$$

$$\frac{\Delta\dot{m}_a}{\dot{m}_a} = \sqrt{(\frac{\Delta P_o}{P_o})^2 + (\frac{\Delta T_o}{T_o})^2 + (\frac{\Delta A}{A})^2 + (\frac{\Delta U}{U})^2} \tag{2.7}$$

In this case the pressure was measured with a high accuracy pressure transducer which has a 0.05% error based on the manufacturer's specifications. The temperature uncertainty is again 1%. The uncertainty in the area is less than 1% and the velocity uncertainty is calculated from the PIV data to be between 5.6 and 7.2%. This gives

a total error for this method of finding the air mass flow rate of between 5.8 and 7.3%.

Fuel mass flow rate was measured using a rotameter; the smallest division divided by a typical value gives uncertainties of 5 %.

CHAPTER III

Near Incipient Blowout Combustion Instability

3.1 Introduction

Using the first of the two fuel injectors described previously in Section 2.1.3, incipient blowout oscillations were studied as part of this thesis work in collaboration with Sulabh Dhanuka [12]. These oscillations occur when the pilot flame is not strong enough to anchor the main flame. The main flame lifts off and then flashes back into the corner recirculation zone. After consuming all of the fuel in the corner, it extinguishes and then relights from the pilot flame at the stable position. Simultaneous high speed video and pressure data capture the phenomena. This work presents the mathematical model that was developed to predict the frequency of the instability. The model was published with the joint data in Reference [12]. This data is summarized in Section 3.2 as a reference for the model which is presented in Section 3.3.

3.2 Very Low Frequency Oscillations

The majority of the previous work [15, 14] on this system was for cases that presented no combustion instabilities. However it was observed that when the pilot fuel flow rate was decreased to the operating conditions listed in Table 3.2, a strong lean-limit instability occurs, as shown in Figure 3.1. The instability can be easily

Case	Pilot 1 Fuel	Main Fuel	Air Flow Rate	Temperature	Chamber Pressure
	g/s	g/s	g/s	K	bar
A	1.1	2.3	228	505	1
B	1.4	2.5	228	505	2
C	1.4	3.5	228	505	3

Table 3.1: Test conditions for incipient blowout tests

heard over the 100 dB background noise of the experiment and the pressure oscillates by 2 psi (0.14 kPa), which is 5.5% of the mean pressure (36.5 psia, 255 kPa). The chemiluminescence signal also oscillates. In the first and last frames of Figure 3.1 only the pilot flame is observed; the Main fuel is not burning. The chemiluminescence and thereby the heat release reach a maximum in frame 4. The chemiluminescence leads the pressure signal by 45 degrees. Figure 3.2 shows the time history of the chamber pressure and the total chemiluminescence for Case A and exhibits clear sinusoidal patterns.

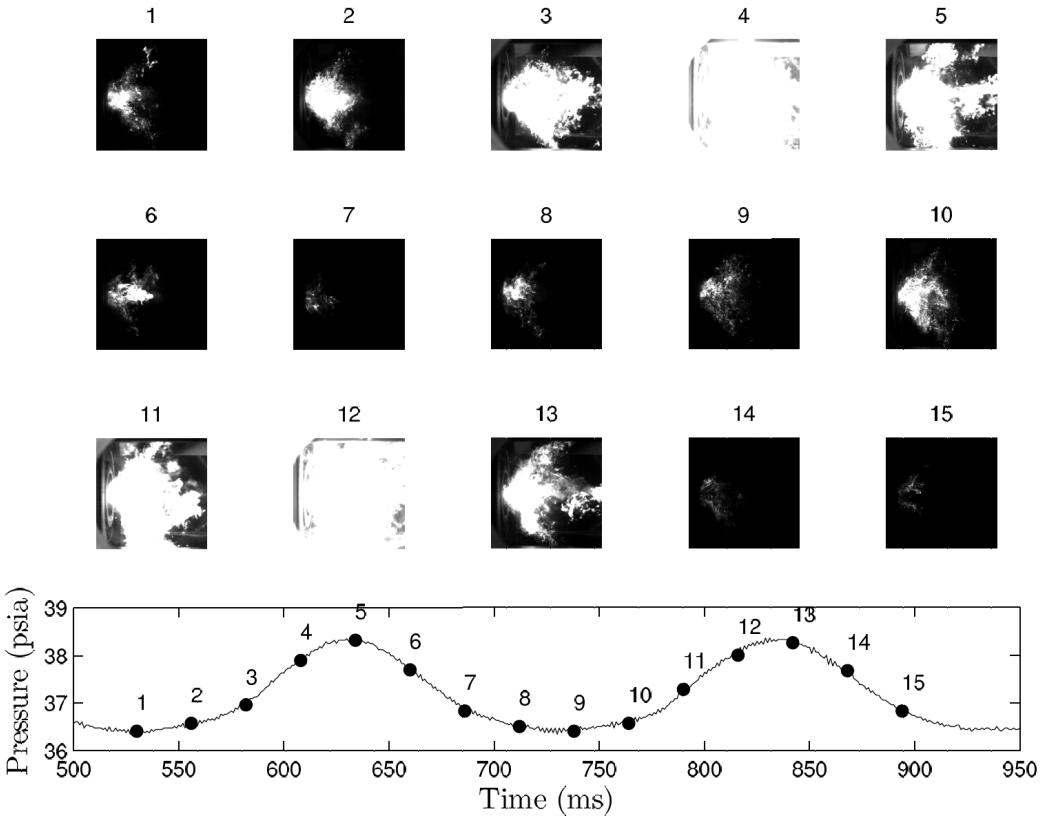

Figure 3.1: Video of Instability and simultaneous pressure trace from [15].

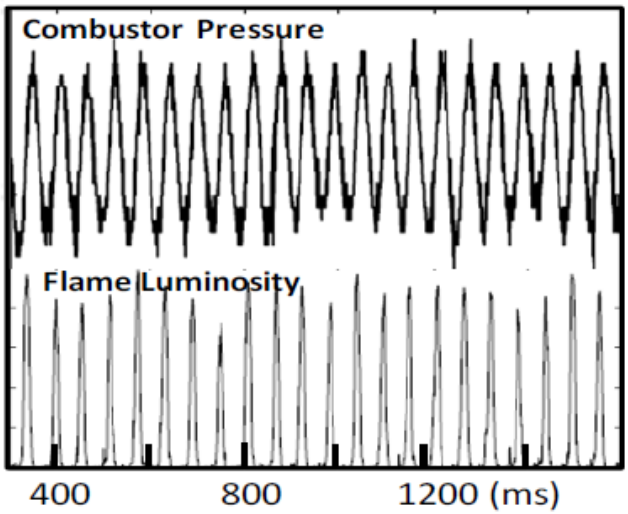

Figure 3.2: Simultaneous traces of chamber pressure and intensity of flame chemiluminescence.[12]

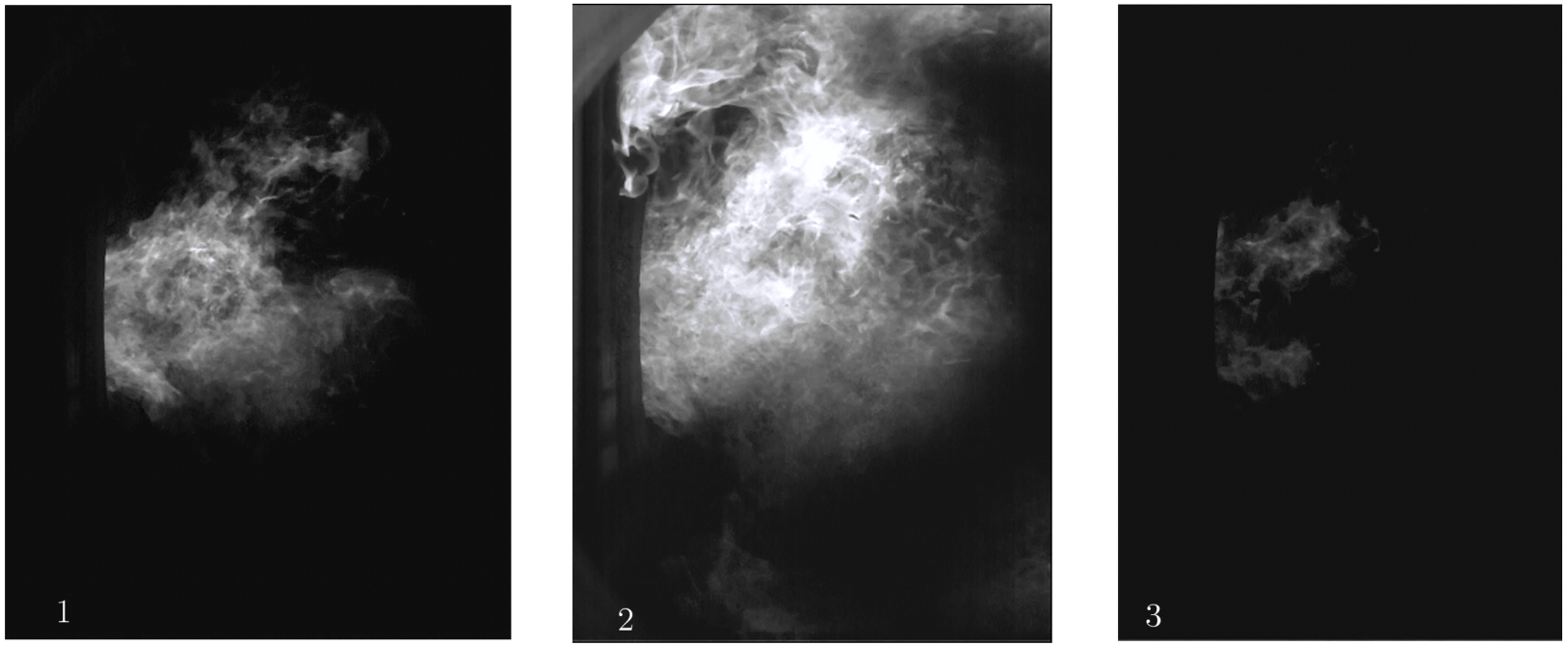

Figure 3.3: Detailed frames of a single instability cycle. The upper recirculation zone in the upper left corner fills with unburned reactants during quasi-steady periods in frame one. Flashback occurs as seen in frame 2 and then quasi-extinction as seen in frame 3.

Figure 3.3 presents more-detailed images from a high-speed movie (taken at 1000 frames/s). Frame 1 shows the flame in between flashback events in a symmetric conical shape. The lower corner of the images are slightly obscured by soot buildup on the window. Here it resembles the flame shape at slightly richer conditions for which the instability does not occur. The corner recirculation zones in the upper and lower left of the figure are filling with unburned reactants from the main fuel and air streams. In Frame 2, the flame flashes back into these unburned reactants. It continues burning against the face of the injector as the pressure rises, until all the reactants in the corner are consumed and the flame quasi-extinguishes as seen in Frame 3. This process repeats in a cyclical pattern throughout the movies.

Figure 3.4 displays some LES computational results of Huang and Yang [22] for a premixed dump combustor. While the flow velocities are larger and dimensions smaller than the current work, the experimental setup contains a similar step geometry. Additionally, the general observations of the physics of their combustion instability have similarities with the present experiment. In the computational results, the flame locally extinguishes near the corner and unburned reactants fill this region. The flame then flashes back through the corner until it reaches the wall and extinguishes. This flashback phenomena produces a periodic pressure rise in the combustor.

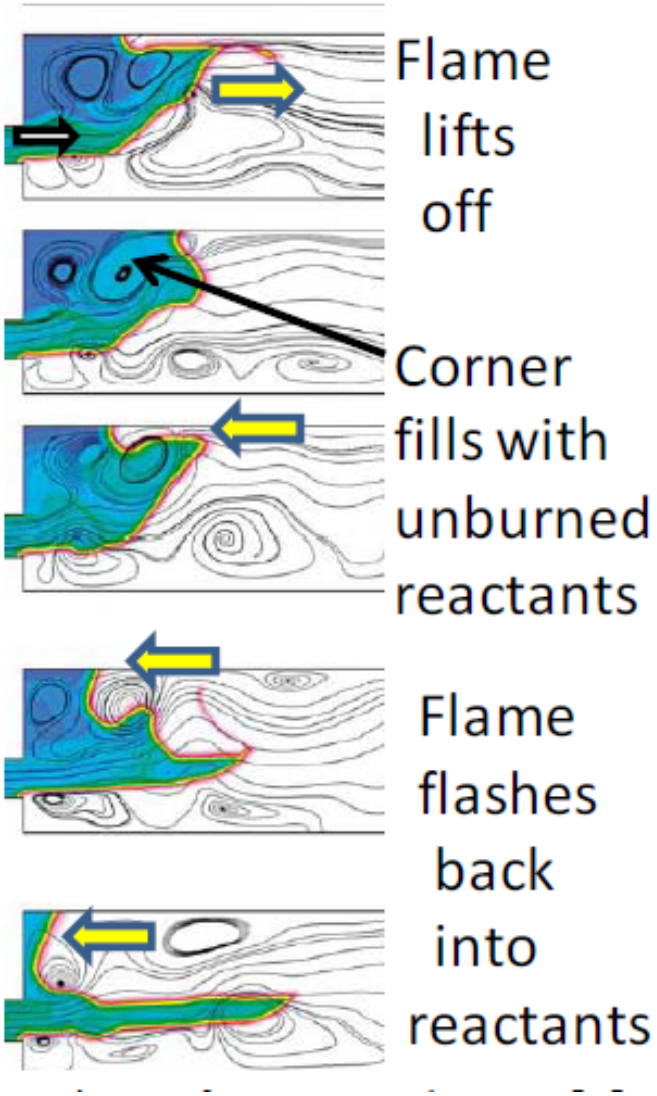

Figure 3.4: LES simulation results showing similar phenomena of corner recirculation zone filling and flashback from Huang and Yang [22]

Figure 3.5 shows one type of phase space representation of the instability data. Each marker indicates one instantaneous measurement of pressure and chemiluminescence intensity on the sinusoidal curves shown in Figure 3.2. Three separate branches are clearly shown in the plot. During Branch A, the main flame flashes back into the corner recirculation zone (as was seen in Frame 2 of Figure 3.3) resulting in a linear increase in pressure and luminosity. During Branch B between the $\phi = 90$ degrees and $\phi = 180$ degrees markers in Figure 3.5, the main flame has consumed all of the fuel and extinguishes so that only the pilot remains lit. Finally, during Branch C, the pilot is constantly lit, but since no main is present the corner volume is refilling with unburned reactants.

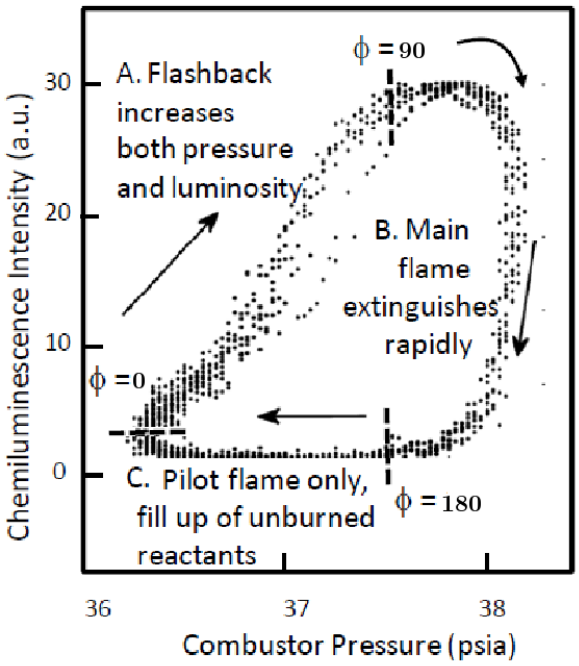

Figure 3.5: Phase space representation of the instability showing the three separate contributing physical phenomena. Time progression is clockwise around the plot.[12]

3.3 Mathematical Model of Incipient Blowout

The driving frequencies of the lean-limit pressure oscillations were measured and a simple analysis was performed that predicts these frequencies. The measured values of the driving frequency of the lean-limit oscillations are shown as the solid symbols in Figure 3.6. Frequencies were found to vary between 5 and 20 Hz and they increased linearly with the burning velocity of the reactants, as shown. The burning velocity was systematically varied by altering the equivalence ratio. Burning velocity was calculated using Equation 3.1 for Jet-A fuel developed by Parsinejad et al.[49]. The equivalence ratio (ϕ) is that of the main fuel and main air flows, since it is this unburned mixture that fills volume where the Main flame has been extinguished.

$$S_b = 62\,(\frac{cm}{s})\,(1 - 1.51(1-\phi) - 1.89(1-\phi)^2)[\frac{T}{450K}]^{2.02}[\frac{P}{1atm}]^{-0.16} \tag{3.1}$$

From observation of the high speed video sequences, the instability is hypothesized to consist of two processes. First, the corner recirculation zone is filled with fuel and second, the flame flashes back through this region. Therefore, the period of the oscillations should be the sum of the time required for each of these two steps. This leads to Equation 3.2.

$$f\alpha(\tau_{fill} + \tau_{burn})^{-1} \tag{3.2}$$

The fill time is the corner volume of the cylindrical combustor that has a length of L, divided by the volumetric flow rate of the Main flow reactants. In the current geometry and flow rates, the fill time (τ_{fill}) was found to be small compared to τ_{burn} but as a general model this term is included. Burn time τ_{burn} is L / S_b where L is

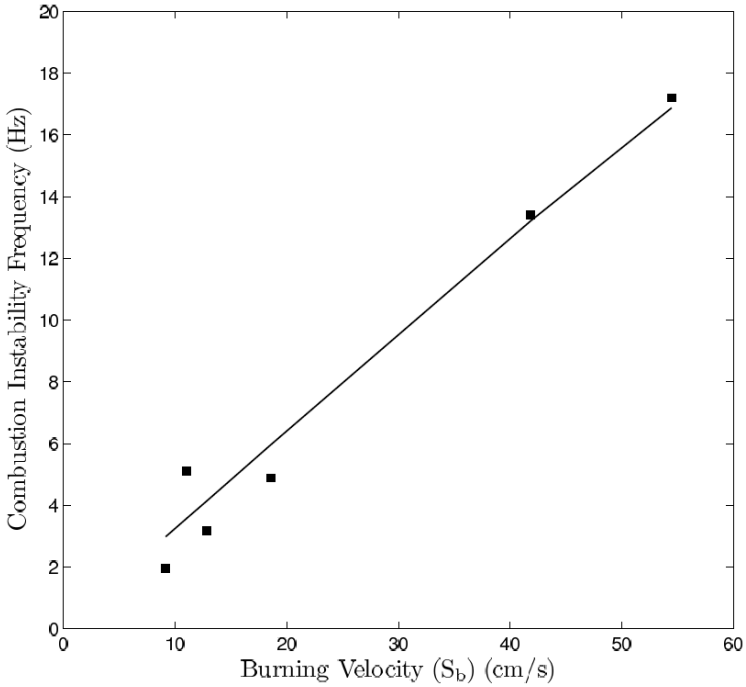

Figure 3.6: Measured frequencies (symbols) compared to proposed model (line).[15]

the length of the volume of region though which there is Main flame flashback. L is set equal to the step height of 3.0 cm (40% of the combustor radius) based on movie images that are similar to Frame 2 of Figure 3.3. For example, for a fuel flow rate of 4.8 g/s, an air volumetric flow rate of 0.045 m^3/s, and a preheat air temperature of 505 K, the calculated value of burning velocity is 55 cm/s, the fill time is 4.2 ms, and the burn time is 55 ms. Thus the driving frequency computed using Equation 3.2 for this example is 17 Hz.

As seen in Figure 3.6), the mathematical model (solid line) agrees well with the measured frequencies (solid symbols). Therefore, it can be concluded that the combustion instability is driven by the filling and flashback mechanism that can occur when the pilot flame is not able to fully stabilize the main flame. This type of instability is similar to the operation of a pulse-jet engine. In the pulse-jet, a new charge

is intentionally added for each combustion cycle; however, in the LPP combustor the fluid mechanics create a similar addition of "charge" to the flow.

CHAPTER IV

Pressure Field Characterization of Unstable Modes

4.1 Introduction

The previous chapter described the lean limit oscillations which occur in the low frequency regime, i.e. at less than 50 Hz. These oscillations caused large pressure fluctuations within the flame tube. This chapter describes the other combustion instabilities that occurred which were in the frequency range of 50 to 1500 Hz. The test cases are detailed in Table 4.3. Flow properties and the physical dimensions of the test rig were then systematically varied to determine the source of these oscillations.

4.2 Representative Pressure Fields and Spectra

Figure 4.1 shows a representative pressure trace taken inside the flame tube. Two important features can be discerned. First, the amplitude of r.m.s. pressure fluctuations was relatively large and was typically 0.75 psi (5 kPa) or approximately 1.7% of the mean pressure. Second, the pressure in the combustor is oscillating in a near sine wave pattern. However, the signal is not a pure sine wave, but rather a fundamental wave with higher frequencies superimposed on top of it. In order to determine the dominant frequencies, Fourier analysis was conducted using Matlab. Power spectral density, PSD, plots were generated using the pwelch command with 10 Hz binning. These plots show the power contributed by each frequency component to

the whole signal. Figure 4.2 shows a representative power spectrum. Of note are the six main frequency peaks. These can be split into two groups of similar magnitudes: the higher frequencies are 560, 860, 1210 Hz, and the low frequencies are 80 and 160 Hz as well as a 240 Hz shoulder. The low frequency peaks are approximately 20 dB larger in magnitude than the higher frequencies. The relative power of each frequency can be found by integrating the area under the peak. This area corresponds to the average power in the pressure fluctuations, expressed as P prime squared bar or $\overline{P'^2}$. Thus the low frequencies can be shown to have 70% to 97% of the total power of the oscillations in the combustor. Explaining the source of both the high frequency and low frequency oscillations is the focus of the current study.

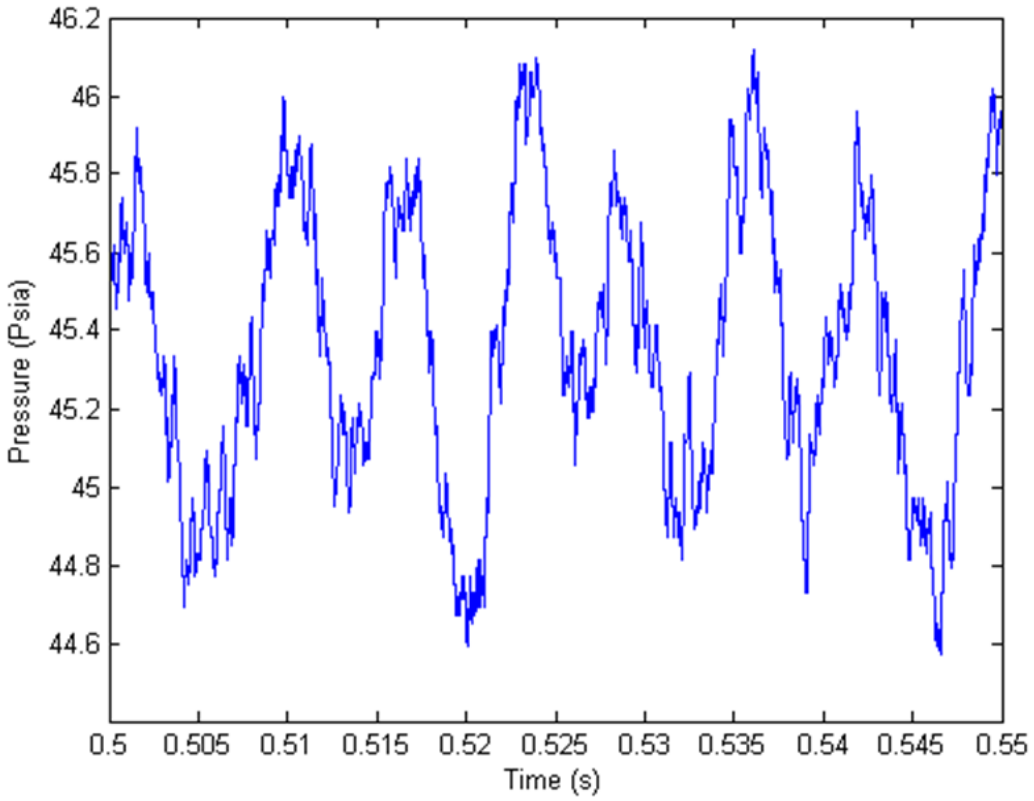

Figure 4.1: Representative pressure trace taken inside the flame tube during combustor operation showing cyclical pressure fluctuations with amplitudes up to 0.75 psi

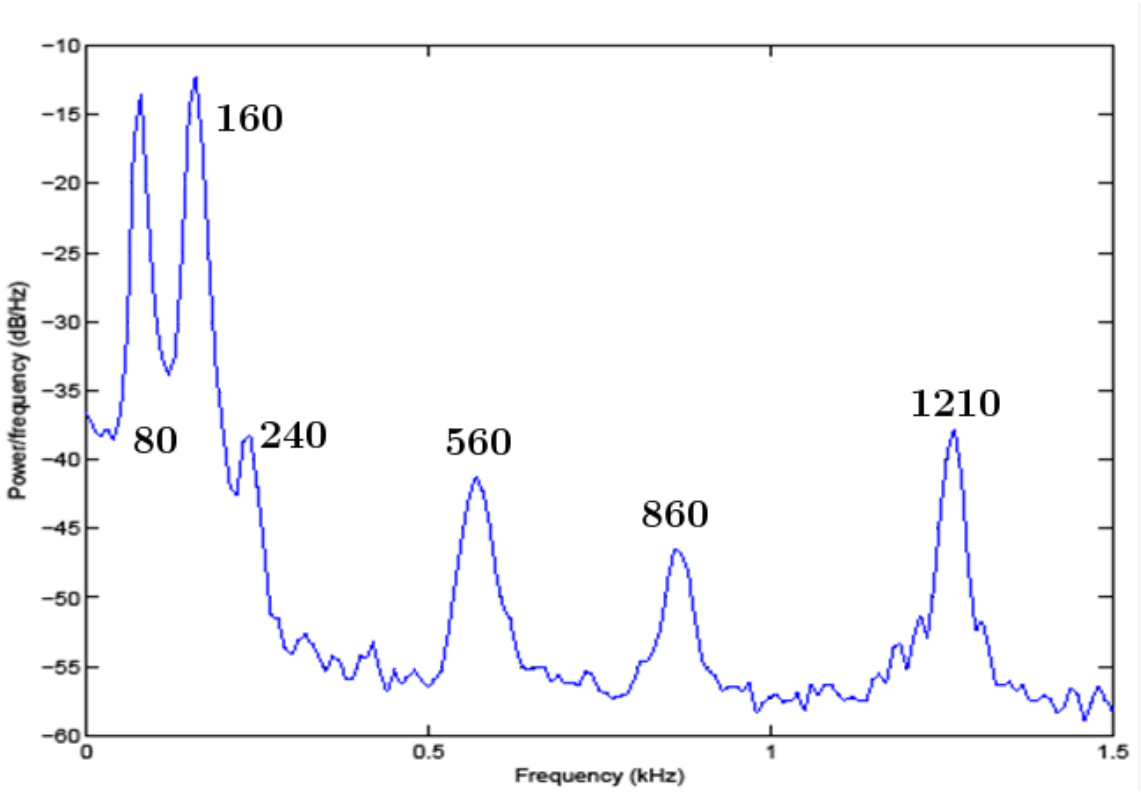

Figure 4.2: Typical power spectrum of a pressure trace. Major peaks of interest are the 80 and 160 Hz which are 20 dB higher in magnitude than the other observed frequencies.

4.3 Fueling Effects

Previous work with a similar LPP injector [12] found that a low frequency oscillation exists which was dependent on fueling conditions. In that study, a low frequency oscillation occurred near the lean blowout limit and the frequency was determined by the local flame speed that was associated with flashback into the corner recirculation zone. The instability was shown to occur only when there was insufficient pilot fuel to stabilize the lean premixed main flame. Due to the similarities in the fuel injectors it was initially proposed that fueling conditions would have a large effect on the instability in the newer configuration. In the current study, GE supplied 3 initial fueling cases, based on observations in full scale rig tests, to determine their effect on

Case	Pilot 1 Fuel Flow Rate	Pilot 2 Fuel Flow Rate	Main Fuel Flow Rate	Air Flow Rate
	g/s	g/s	g/s	g/s
1	8.5	0.0	0.0	328
2	3.8	4.7	0.0	328
3	3.8	2.2	2.5	328

Table 4.1: Provided initial test conditions

the instability. These cases are shown in Table 4.3. All three cases are run at 3 atm with 465 K preheated air with the same equivalence ratio of 0.38. They only differ in which of the three fueling types, detailed in Section 2.1.3, are utilized. Case 1 and Case 2 are pilot fuel only cases, with Case 2 using both pilots and Case 1 using only the primary pilot. Case 3 uses both pilots and also the main fueling ports. In all three cases, the combustion chamber pressure showed oscillatory behavior and the PSD for each case is shown in Figure 4.3 along with a non-reacting baseline case.

As discussed in Sec 4.2, the pressure spectrum shows two main groups of frequencies: a grouping of low frequencies around 80 and 160 Hz, and a group of higher frequencies. In comparison to the non-reacting baseline case, the higher frequency peaks remain at roughly similar magnitude when the flame is ignited. A shift is observed at the highest frequency. This frequency is believed to correspond to a quarter wave mode in the flame tube which has a frequency that is given by Equation 4.1. The speed of sound is c and L is the physical length of the flame tube.

$$f = \frac{c}{4L} = \frac{\sqrt{\gamma RT}}{4L} \tag{4.1}$$

When the flame is ignited, the observed frequency shift is due to the change in temperature, and thus sound speed, within the flame tube. The two rich, pilot only cases produce higher temperatures and thus higher frequencies, while the lean main

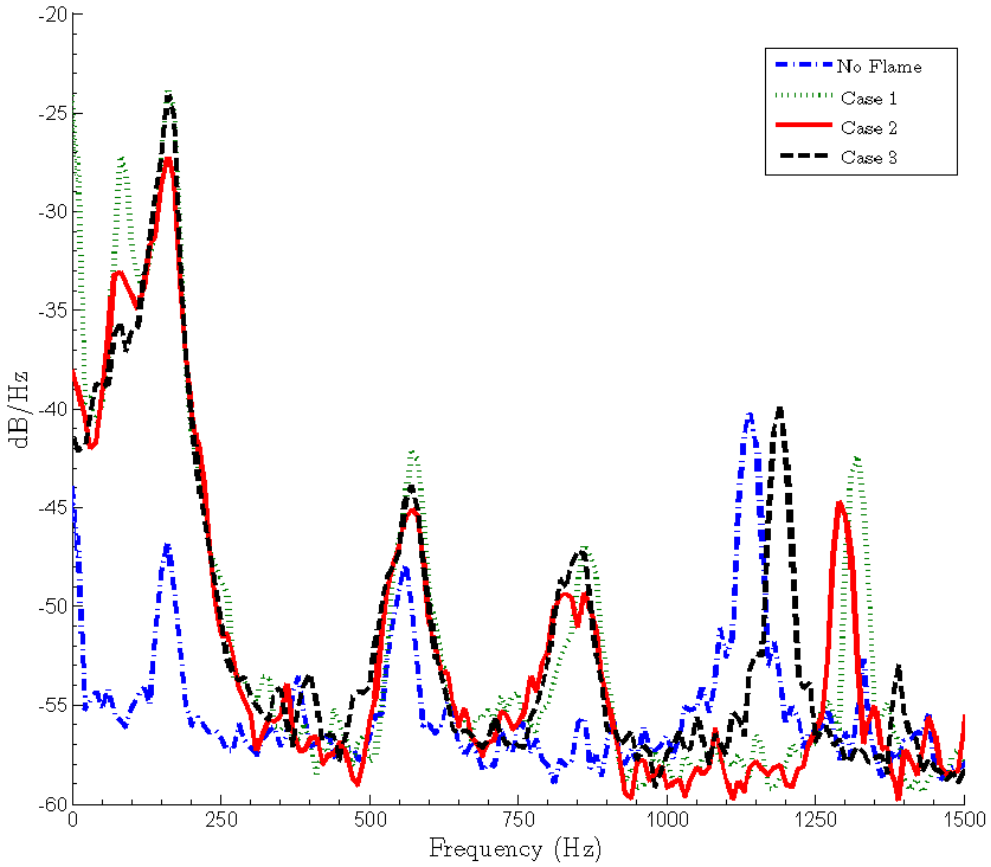

Figure 4.3: Power Spectral Density Plots for three fueling cases and non-reacting baseline. Only the low frequency peaks are amplified by combustion. Note that the frequencies of the 80 and 160 Hz peaks do not vary with type of fueling. The highest frequency peak does show dependence on fueling rates.

flame case produces temperatures much closer to the non-reacting baseline. This is expected because the main feature of LPP combustion is the reduction in peak temperatures by burning a portion of the fuel in the lean main flame[43]. The reacting cases also demonstrate a significant amplification of the low frequency portions of the spectrum. This amplification occurs equally for all three fueling cases. This has two implications. First, the low frequency peaks exist independent of the combustion and are amplified to become the dominant frequencies in the system because of

heat released during the combustion process. Second, while an effect of the lean main flame was observed in the higher frequency peaks, the amplification of the low frequency peaks appears to be unaffected by the presence or lack of a lean premixed main flame. Thus it can be reasonably concluded that the amplification is primarily driven by the rich pilot flame interacting with the system.

Based on these results, a wider range of fueling conditions was tested. Equivalence ratios were varied from 0.2 to 0.54 and the ratio of fuel provided to Pilot 1 and Pilot 2 was varied. In all cases tested the 80 and 160 Hz peaks were observed and they only varied in their respective magnitudes. Figures 4.4 and 4.5 present the results of varying the equivalence ratio. In Figure 4.4 there is a clear trend; as equivalence ratio increases the magnitude of the oscillation increases. This is expected as more heat is released in phase with the pressure wave, which should produce more amplification of the wave. The boundary for growl is defined to occur when the PSD exceeds -35 dB. At this limit, the low frequency peaks begin to dominate the system. In order to run the rig without growl, the results in Figure 4.4 indicate that the equivalence ratio should be set to less than about 0.225. Figure 4.5 separates out the two ways that equivalence ratio can be changed by varying either the fuel flow rate or the air mass flow rate. From the plot it is clear that the effect of the fuel flow rate is much greater than any effect from the air flow rate.

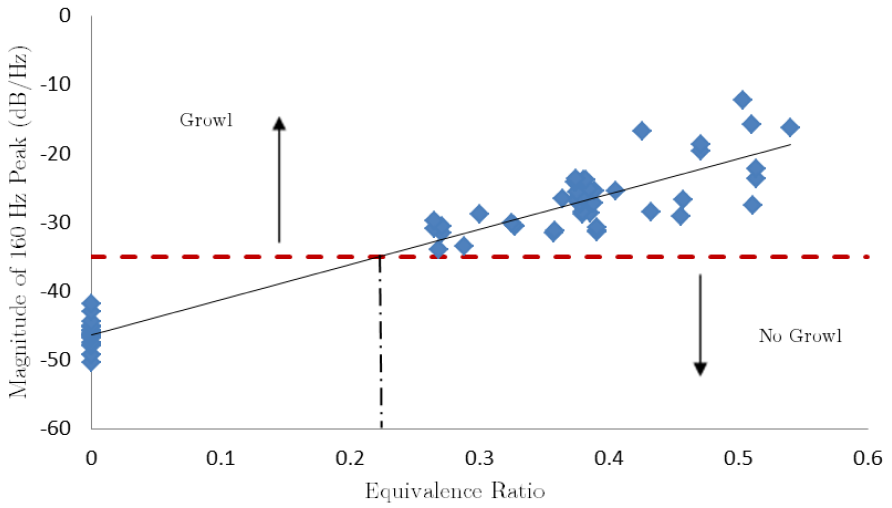

Figure 4.4: Effects of equivalence ratio on the magnitude of the combustion instability. There exists a nearly linear growth in magnitude of the oscillations with equivalence ratio. Stable conditions can be achieved by running at equivalence ratios of less than 0.225

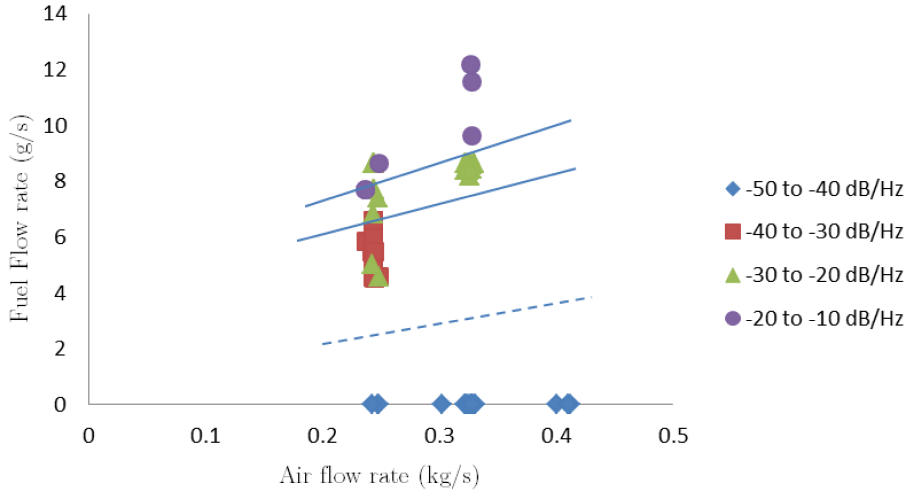

Figure 4.5: Effects of fuel flow rate and air flow rate on the growl instability. The fueling flow rate has a much greater impact on the magnitude of oscillation than the air flow rate. The lines indicate general transitions between decades of magnitude of the power spectrum peaks.

Figures 4.6 and 4.7 show the results of varying the ratio of fueling between Pilot 1 and Pilot 2. In both plots, the x-axis is a non-dimensional parameter ζ given by Equation 4.2. Using this notation, ζ is one when all the fuel is injected through Pilot 1 and ζ is zero when all the fuel is injected through Pilot 2. From the figure, it appears the distribution of fuel between the pilots does not have a significant effect on the magnitude of the instability. This is important because a common industrial practice to minimize the impact of instabilities is to add fueling to a secondary location, and this is the reason for the secondary pilot on the current injector. The current data suggest that this second pilot may be unnecessary for the control of the low frequency instability.

$$\zeta = \frac{\dot{m}_{Pilot1}}{\dot{m}_{Pilot1} + \dot{m}_{Pilot2}} \tag{4.2}$$

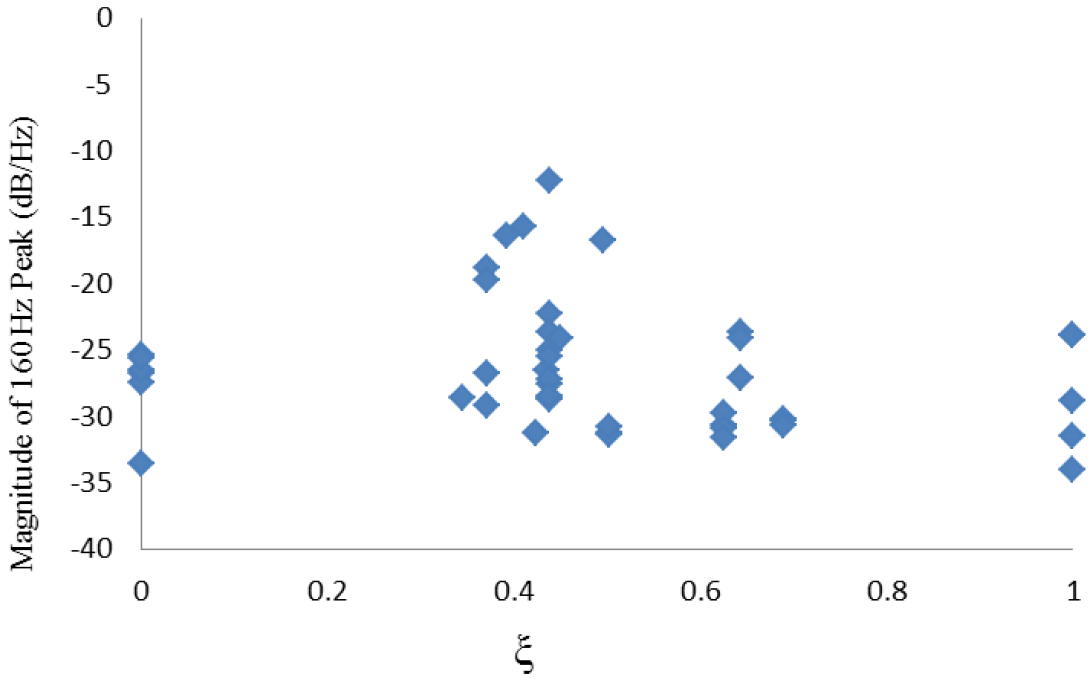

Figure 4.6: Effects of varying the ratio of fuel provided to the two pilot fuel injection locations. No clear trend is seen in the effort to minimize the magnitude of the instability.

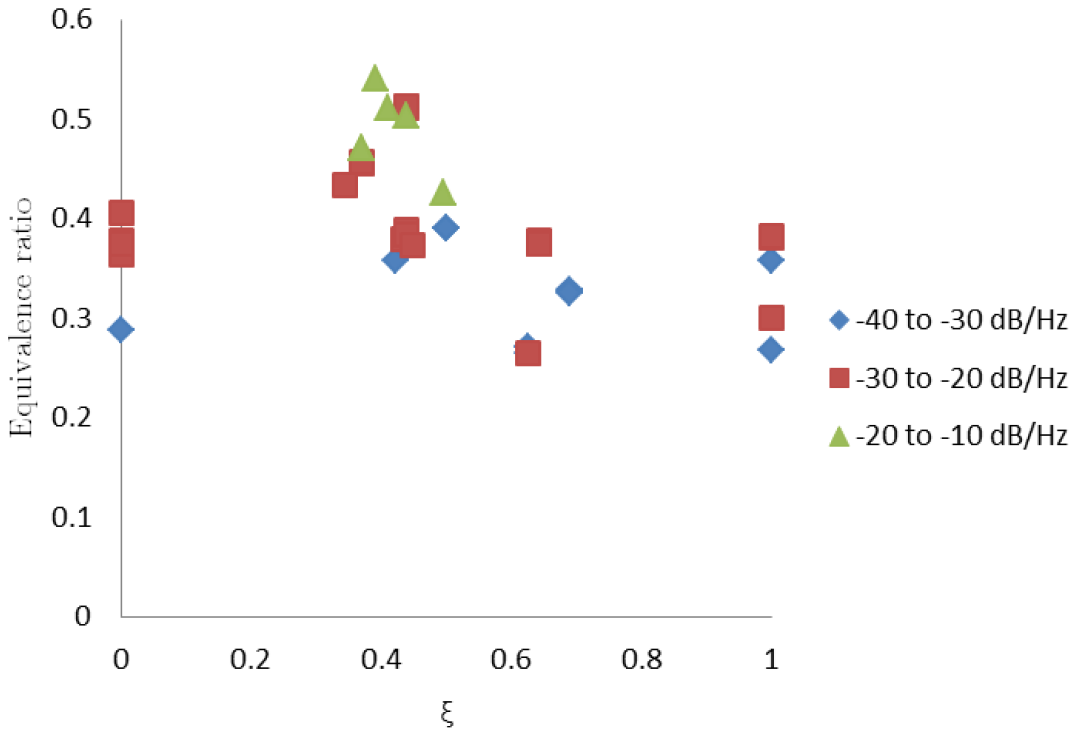

Figure 4.7: Effect of equivalence ratio and fuel distribution on the magnitude of the 80 Hz and 160 Hz instabilities. The fueling ratio (ζ) seems to produce no effect on the magnitude of oscillations.

4.4 Selection of Further Test Cases

Because of the results of the fueling tests, a single fueling case was selected for the remainder of the study. The low frequency oscillations were determined to be driven by the rich pilots rather than the lean main flame, so the new test case was run with pilot fueling only. Additionally, the case that was selected produces the largest magnitude pressure fluctuations, thereby aiding the observation of the phenomena. The test parameters are listed in Table 4.4 and the spectrum for this case is shown in Figure 4.8. The selected case was richer than Case 2; the equivalence ratio was 0.5 while the equivalence ratio of Case 2 was 0.38. This resulted in pressure oscillations that were 10 dB larger than Case 2.

Case	Pilot 1 Fuel Flow Rate	Pilot 2 Fuel Flow Rate	Main Fuel Flow Rate	Air Flow Rate
	g/s	g/s	g/s	g/s
4	3.8	4.7	0.0	246

Table 4.2: Maximum magnitude instability test conditions selected for this study

4.5 Investigation into a Possible Convective Instability

One potential mechanism that could be causing the low frequency oscillations is referred to as a convective acoustic oscillation [76]. This mechanism describes a perturbation in a flow which is convected downstream and then sends pressure disturbances back upstream at the acoustic velocity. In flows undergoing sudden expansion, i.e. flow over a backward step, these flow perturbations are the shedding vortices. Yu et al.[76] showed that the pressure waves propagating upstream would produce a standing wave in the plenum. This can be shown in two separate plots. First, the spatial cross-correlation coefficient, $C(x)$, is defined by Equation 4.3 and

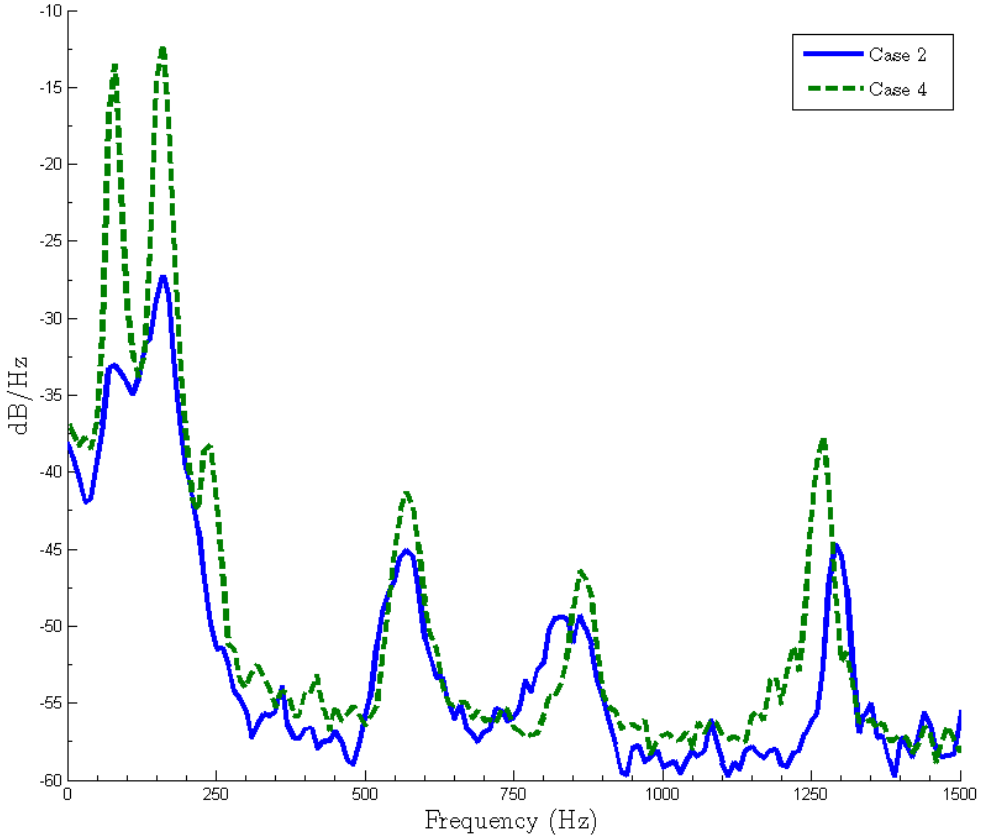

Figure 4.8: Pressure power spectra for Case 2 and Case 4 conditions. The 80 and 160 Hz frequency peaks of Case 4 are very large and this makes it easier to identify any changes in the behavior of the instability.

values of this coefficient measured by Yu et al. are seen in Figure 4.9.

$$C(x) = \frac{\int_0^T P(x_0,t)P(x,t)\,\mathrm{d}t}{(\int_0^T P^2(x_0,t)\,\mathrm{d}t\ \int_0^T P^2(x,t)\,\mathrm{d}t)^{\frac{1}{2}}} \tag{4.3}$$

A standing wave is produced by an acoustic convective oscillation in Yu's work because the spatial correlation coefficient is 1 near the step and is -1 far upstream in the plenum in Figure 4.9. Figure 4.10 shows the measured value of this coefficient based on data from the current study. The face of the burner is at x/h=0. Positive values of x/h occur in the flame tube and negative x/h values occur in the plenum.

For all of the locations in the plenum the coefficient is approximately one in Figure 4.10, indicating that rather than a standing wave, there is a bulk mode oscillation which is typical of a Helmholtz resonator.

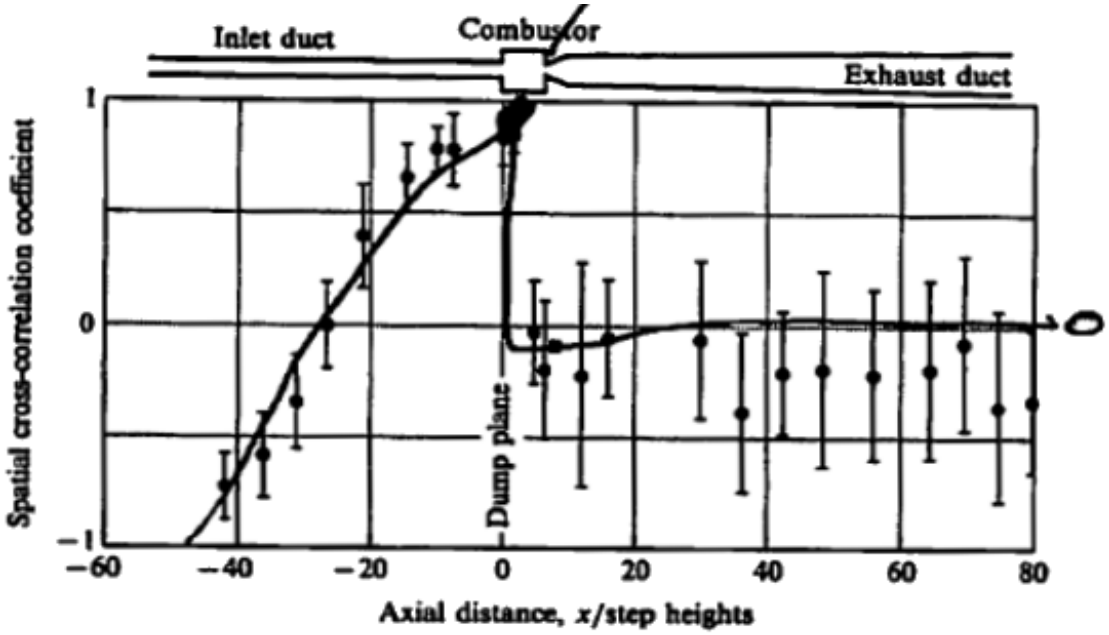

Figure 4.9: Yu et al. [76] plot of spatial cross-correlation. A standing wave in the plenum caused by an acoustic convective instability results in the spatial cross-correlation varying from positive one to negative one.

Figure 4.11 shows the magnitude of the PSD for the main frequency as a function of location in the plenum for Yu's acoustic convective instability. The corresponding plot for the current data is shown in Figure 4.12. Again, the face of the burner is at x/h=0 and positive values identify the flame tube while negative x/h values occur in the plenum. While the shape of Yu's data (Figure 4.11) clearly shows that a standing wave exists throughout the inlet duct, the current data in Figure 4.12 show a step function behavior indicating bulk modes. The flame tube has much stronger oscillations than the plenum.

Figure 4.13 shows the phase lag which arises in Yu's experiment from the standing wave in the plenum. However, in the current study the phase of the pressure in the

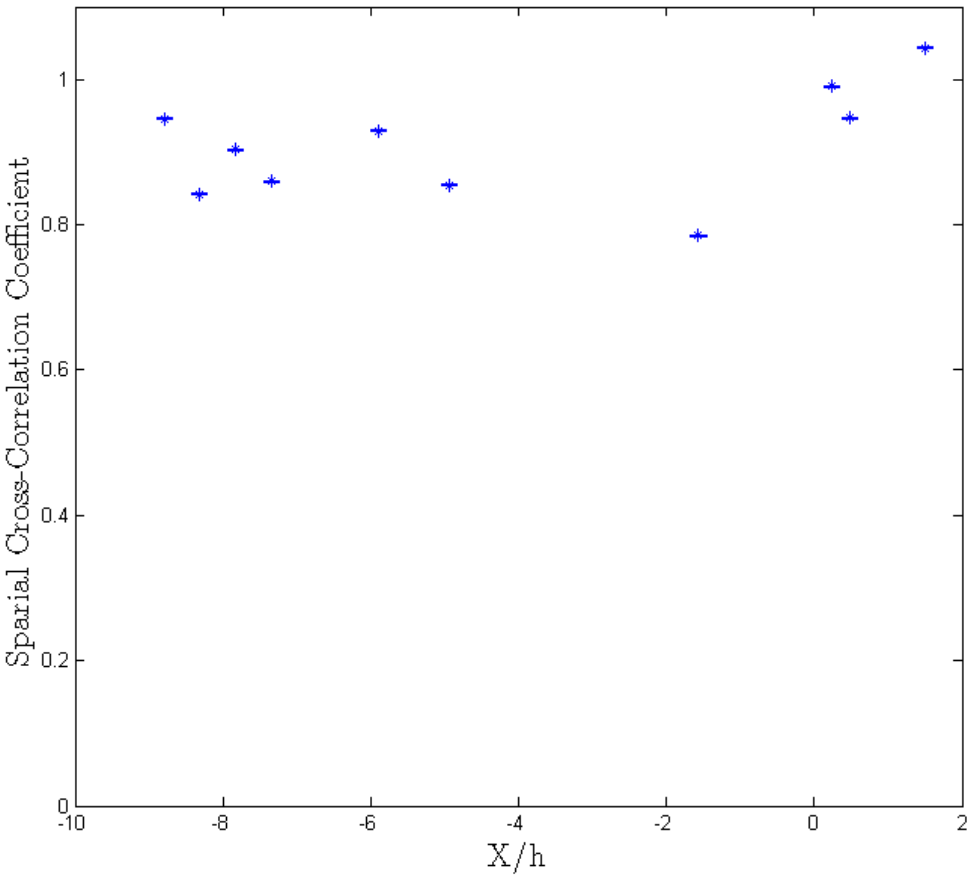

Figure 4.10: Measured spatial cross-correlation, $C(x)$, in the LPP combustor. $C(x)$ is defined by Equation 4.3. The value is effectively one everywhere indicating that the low frequencies are not an acoustic convective oscillation as seen in the Yu et al. data in Figure 4.9

plenum is constant and lags the pressure in the combustor by 45 degrees, shown in Figure 4.14. This is indicative of a Helmholtz-like bulk mode.

Taken together, these comparisons indicate that our observed low frequency oscillations do not appear to be acoustic convective instabilities. Additionally, the bulk mode data, shown in Figure 4.12, and the phase lag data, shown in Figure 4.14, indicate the presence of a Helmholtz type resonator.

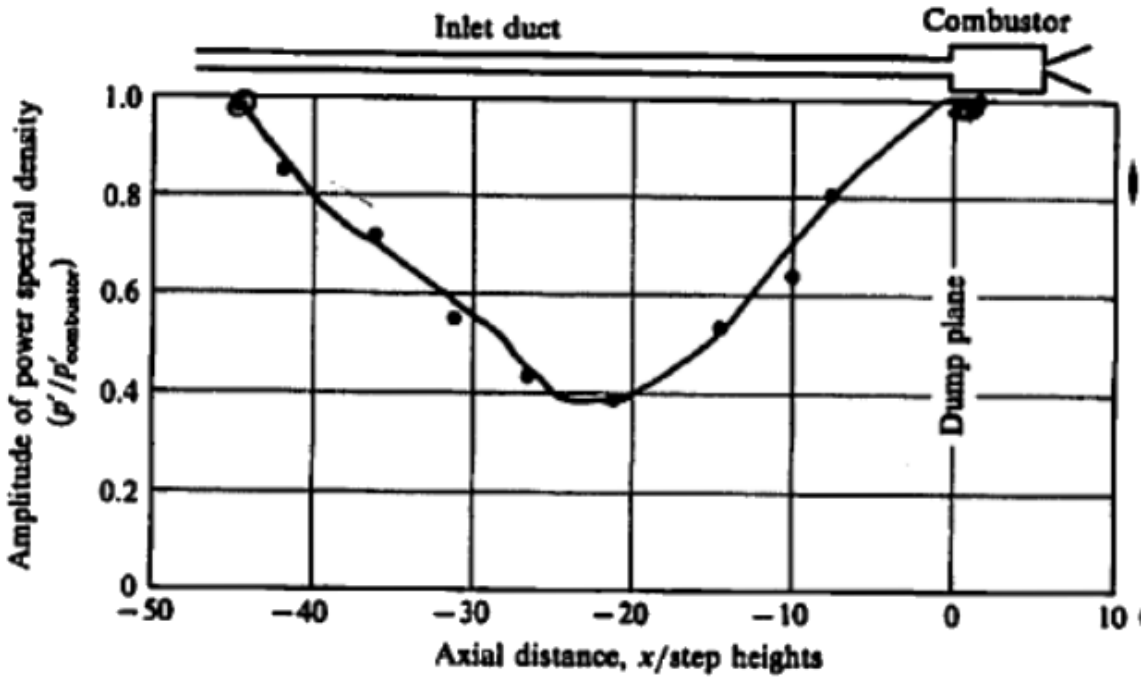

Figure 4.11: Amplitude of the main PSD peak from Yu's paper (Yu et al. [76]) showing that a standing wave exists in their plenum.

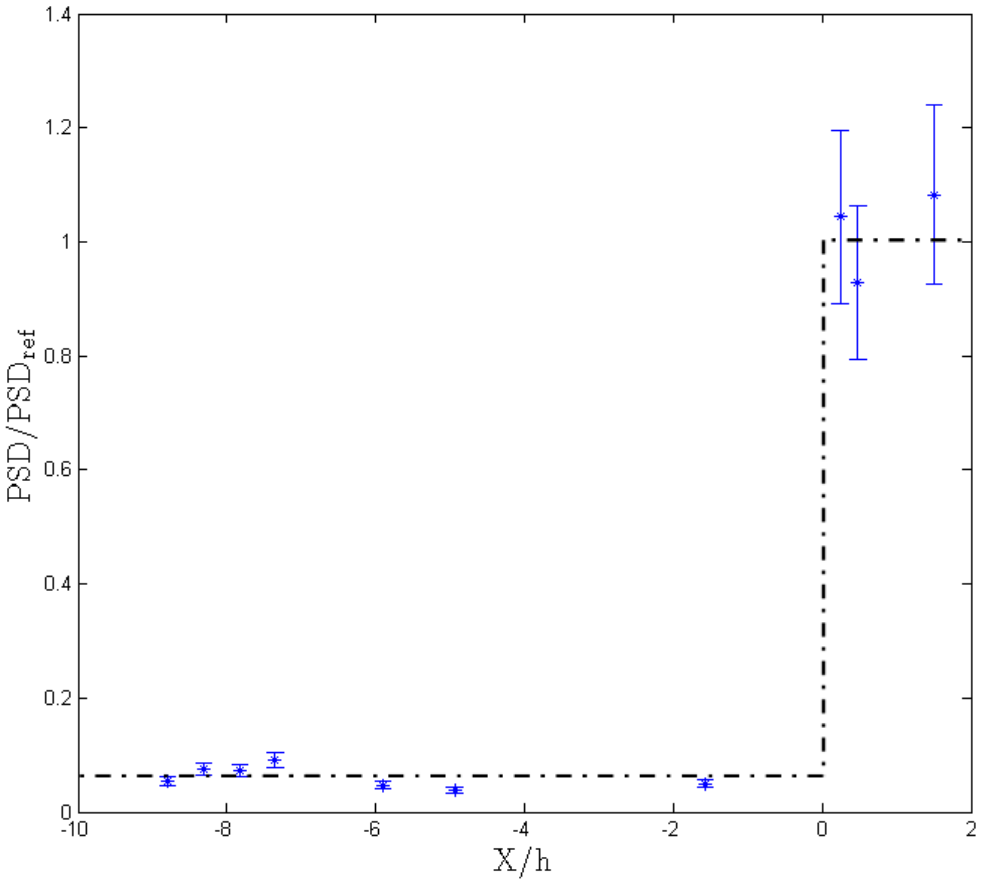

Figure 4.12: Amplitude of PSD for current study showing the presence of two bulk modes. The injector face is at x/h=0

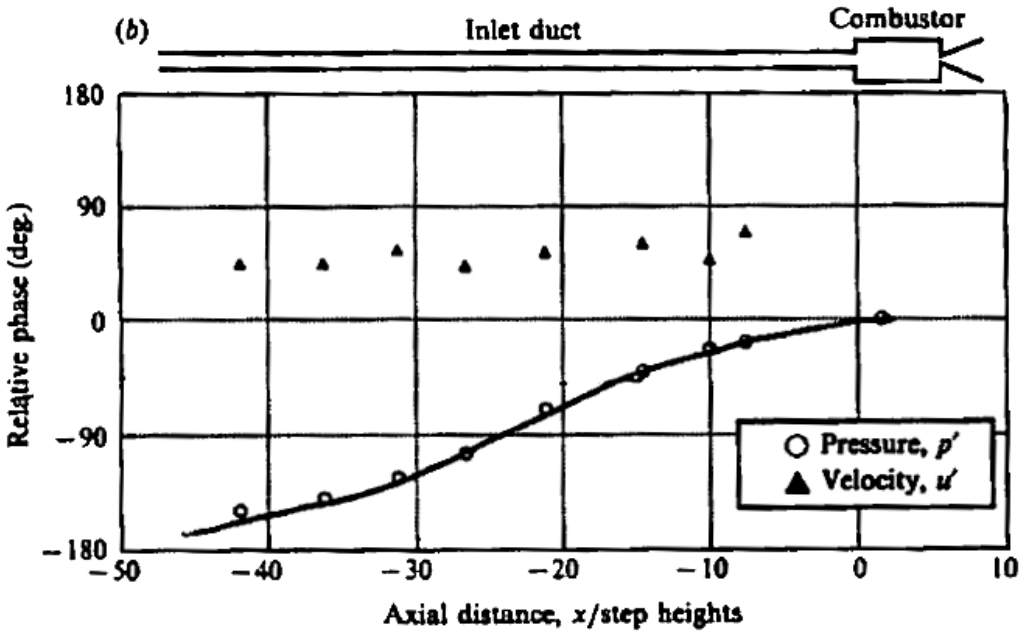

Figure 4.13: Phase lag plot from Yu et al.[76] which shows a changing phase lag between the plenum and combustion chamber pressures due to a standing wave in the plenum.

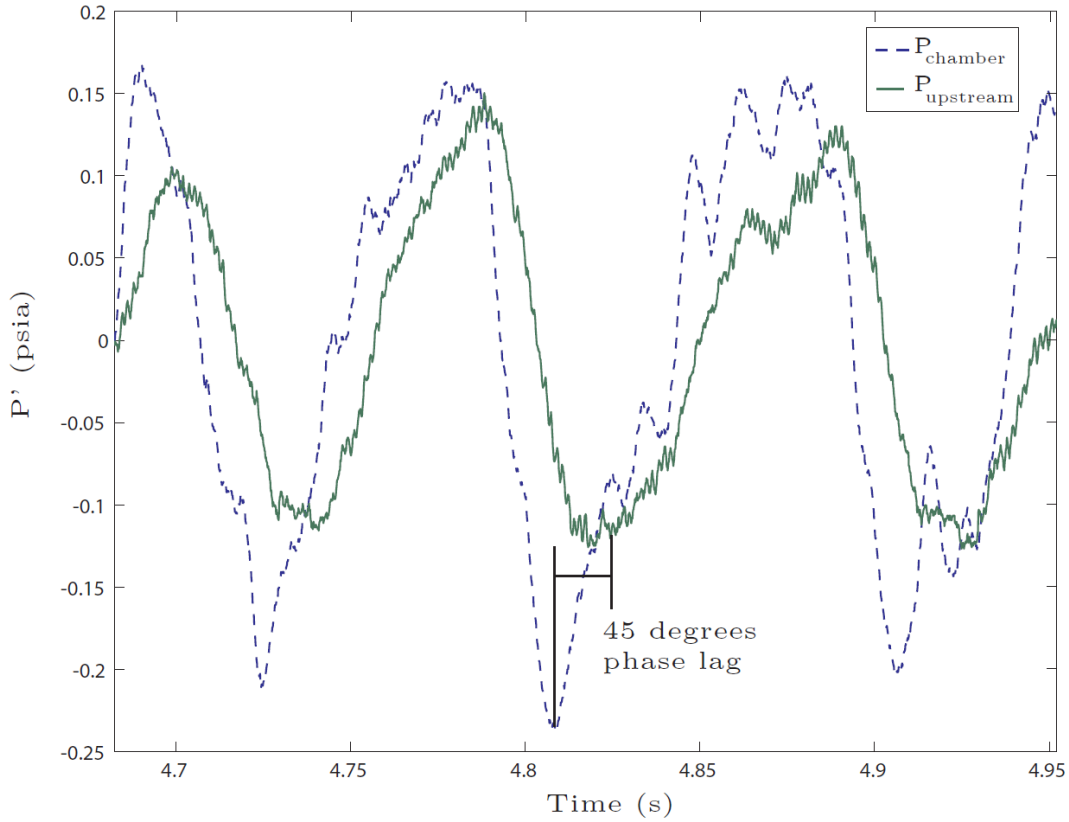

Figure 4.14: Phase lag between the pressure in the flame tube and the plenum. There is a constant 45 degree lag indicating a bulk mode type oscillation.

4.6 Effects of Physical Alteration of the Test Section

Two possible instability mechanisms exist which are directly related to the physical dimensions of the experimental setup: organ tone modes and Helmholtz modes. The frequencies of these two modes will shift readily due to any change in the physical dimensions which govern them. In order to ascertain if either mode had an effect on the low frequency oscillations of interest, a number of physical dimensions where changed in the combustor setup. These changes are summarized in Figure 4.15.

If an organ tone quarter wave mode is present, it would be governed by Equation 4.1 as discussed previously. The quarter wave must fit within the physical length of the pipe. With room temperature air and resulting speed of sound, the 80 Hz mode would require a pipe length of approximately two meters. However, this is the length of the whole experimental system from choked orifice to the downstream valve used to set the back pressure in the combustion chamber. In order to determine if a quarter wave mode was the source of the low frequency oscillations, this length was varied by separately removing the plenum and the downstream valve, which changed the length by 50 to 100%. In each case, no change was observed in the frequency of the oscillations of interest. Additionally, the length of the flame tube itself was varied by 30% and this too resulted in no frequency shift in the 80 and 160 Hz oscillations. Because there is no frequency change due to the changes in lengths, it can be concluded that the low frequency oscillations are not longitudinal organ tone modes. Radial and azimuthal organ tone modes were ruled out because the radius and the circumference of the rig were much too small to create 80 Hz or 160 Hz oscillations.

Helmholtz modes are bulk modes which are analogous to a simple harmonic os-

cillator. Inside of a constricted area, a mass of air oscillates. The important physical scales therefore are the potential volumes and their corresponding "necks" which have an area and length. Commonly in combustion experiments the plenum is identified as a source of a Helmholtz mode [67]. In the current experiment the volume of the plenum was changed by filling it with extra flow straightening beads as well as removing it entirely from the system. In all cases, this resulted in no frequency change. The other possible volumes of interest were varied as summarized in Figure 4.15. Again all of these changes resulted in no observed frequency shift. Thus while bulk mode behavior has been observed in the pressure traces, the obvious candidates for the volume associated with a Helmholtz resonator are not responsible.

Preheat temperatures were varied and separately gasoline was added to the fuel in order to determine if the spray characteristics had an effect on the oscillation frequency. They did not. Syred [70] showed that the frequency of the precession will vary linearly with the mass flow rate. In order to rule out precessing vortex core effects, the air mass flow rate was varied from 150 g/s to 400 g/s. This produced no change in the observed instability frequency.

Through the process of elimination, the only remaining part of the experiment which could affect the oscillation frequency was the TAPS injector itself. However, it was not possible to modify any interior dimensions of the TAPS fuel injector. A similar study of a twin annular premixed swirl burner using gaseous fuels [1] found that the outer swirler was necessary to produce the low frequency oscillations. Therefore experiments were run to vary the amount of air that went through the outer swirler. Figure 4.16 shows the frequency response of the system to the amount of blockage to the outer swirler. As the area of the outer swirler is blocked off, the frequency of the 80 and 160 Hz oscillations drops toward zero. Thus the outer swirler

area is one geometric factor that controls the frequency of the instability.

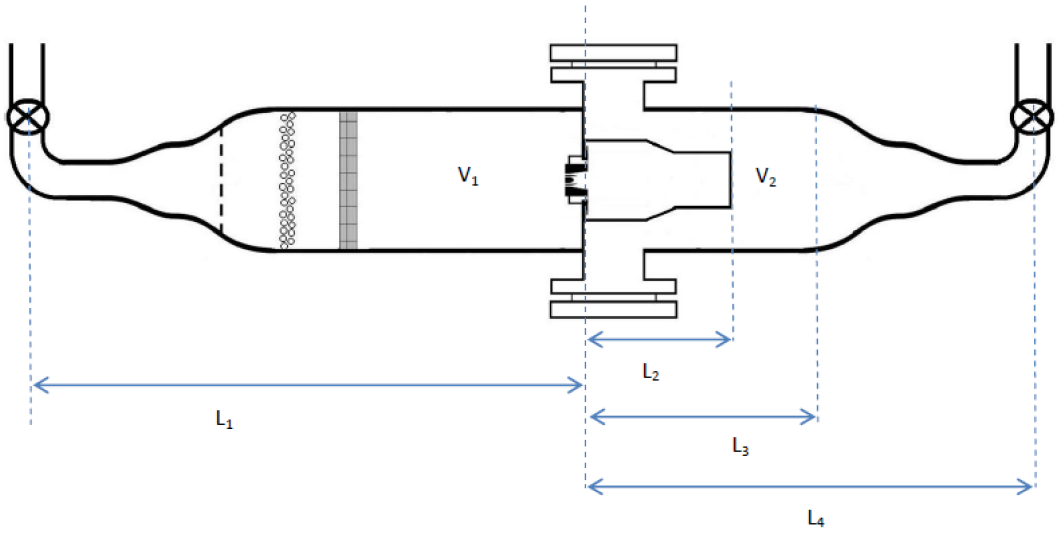

Figure 4.15: Physical parameters which were systematically varied to identify the source of the observed frequencies.

Parameter Varied	Original Condition	New Condition	Frequency Shift	Magnitude Shift
V_1	0.18 m^3	0.012 m^3	None	None
V_2	0.0065 m^3	0.027 m^3	None	Small reduction
L_1	1.57 m	0.94 m	None	None
L_2	0.17 m	0.10 m	None	Small reduction
L_3	0.36 m	0.99 m	None	Small reduction
L_4	0.76 m	1.91 m	None	None
Air Mass Flow Rate	150 g/s	400 g/s	None	Small increase
Preheat Temperature	460 K	500 K	None	Small reduction
Equivalence Ratio	0.38	0.2 to 0.54	None	Shifts possible
Pilot Fueling Ratio	0.5	0 to 1	None	Shifts possible
Gasoline Added	0%	up to 20% by vol.	None	Small increase
Outer Swirler Area	100% open	50% to 0%	Large Shifts Possible	Large Shifts Possible

Table 4.3: Results of variations of physical parameters

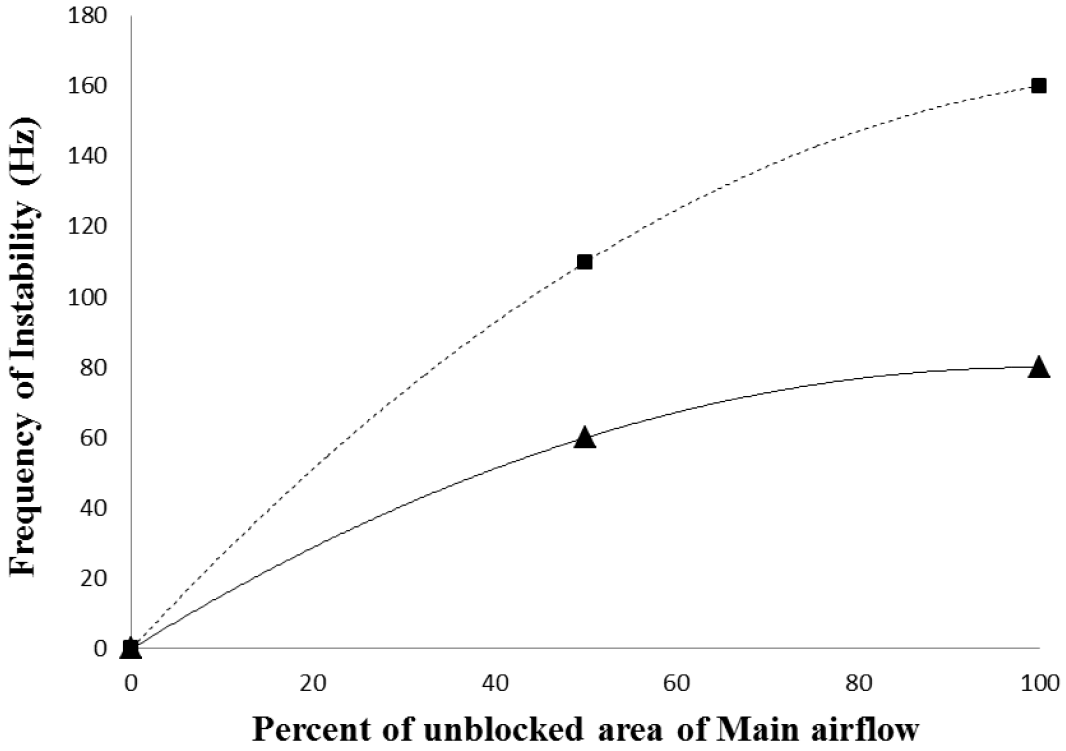

Figure 4.16: Frequency shift of the 80 Hz and 160 Hz instabilities due to physical changes to combustor dimensions. With the exception of the outer swirl cup none of the geometry variations produces any effect on the frequency of the instability.

In summary, twelve physical parameters were varied which are listed in Figure 4.15. Only one, the outer swirler area, caused changes in the frequency of the oscillations that occurred at less than 200 Hz. The spatial correlation data indicate that the source of the oscillations is a bulk mode (Helmholtz-like) mechanism. Developing a full model for the combustion instability is beyond the scope of the thesis, but the data provide a useful guide for future modeling of this combustion instability. In Chapter VI, a discussion of the acoustics is presented that is based on these measurements and results.

CHAPTER V

High Speed Videography of Combustion Instability

5.1 Introduction

While pressure field measurements can identify the existence of instabilities and characterize their frequency components, they do not provide information on how the flame itself is responding to these instabilities. An important question is whether the flame remains attached to the fuel injector and its length oscillates, or if the flame lifts off and flashes back during each cycle of the instability. For this it is necessary to directly observe the flame with optical techniques. In the current study this was done using the high speed videography system that was discussed in Section 2.3. The high speed images capture the flame's reaction to the pressure fluctuations and show that the low frequency pressure oscillations are integrally coupled with a large scale flame response.

5.2 High Speed Videography

Figure 5.1 shows a single frame of a movie taken at 1000 Hz with a 4 μs exposure. The run conditions are those for Case 4 "Maximum Growl" listed in Table 4.4. For comparison, the schematic seen in Section 2.1.3 is repeated in Figure 5.2. In the image, flow is from left to right and the flame shows a number of interesting behaviors. First, the flame is lifted some distance from the face of the injector.

While the lean premixed main flame is expected to be lifted, the rich pilot flame is not expected to be lifted. Second, the flame exhibits a conical shape as it is stabilized around the inner recirculation zone. Third, there exists a central spire of flame which is present throughout all of the videos. This is consistent with previous PIV results in a similar LPP burner [13] which found that there was a positive centerline velocity. This velocity is created when the flame pulled the inner recirculation zone apart into a toroidal shape. It was proposed that the flame acts as a partial blockage which redirects some amount of air to the inner swirler producing the positive centerline velocity.

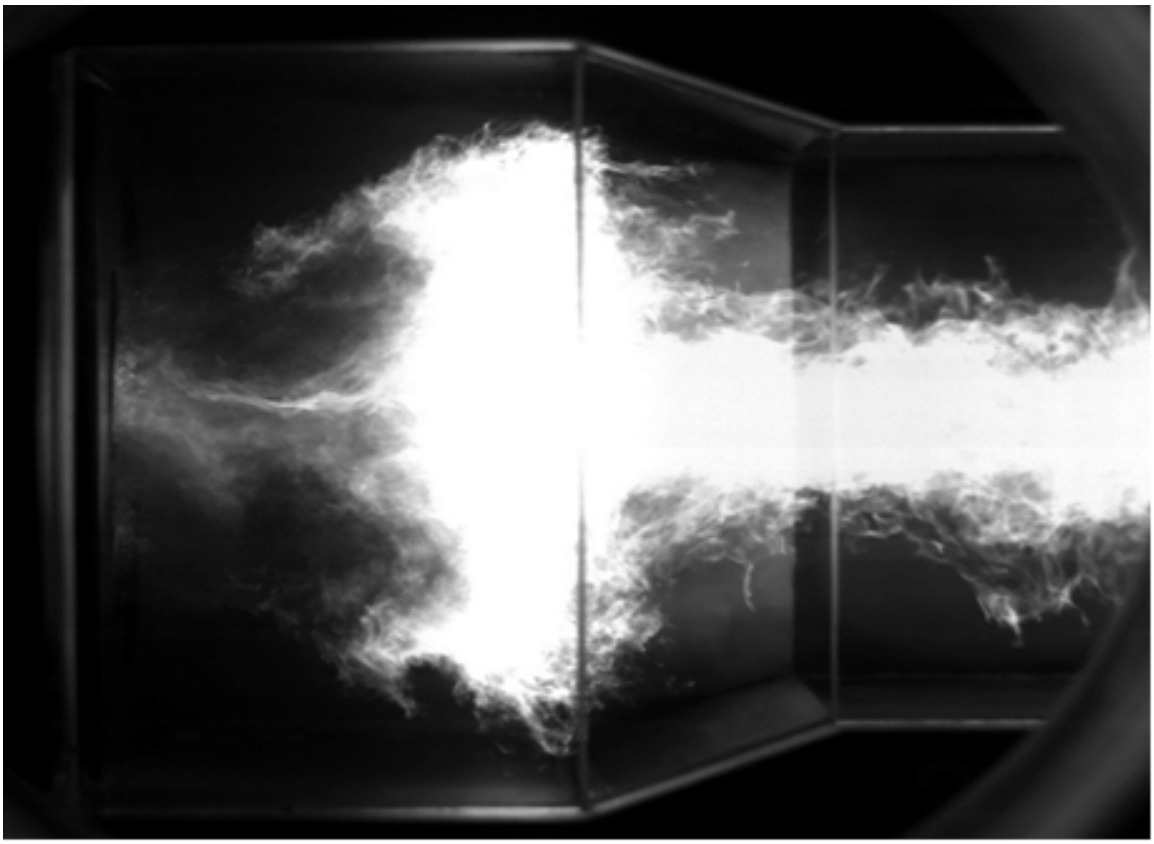

Figure 5.1: Selected image of the flame in the LPP combustor.

Figure 5.3 contains images and pressure data for one and a half cycles of the combustion instability. At times when the pressure is lowest (frames 2,3,8, and 9),

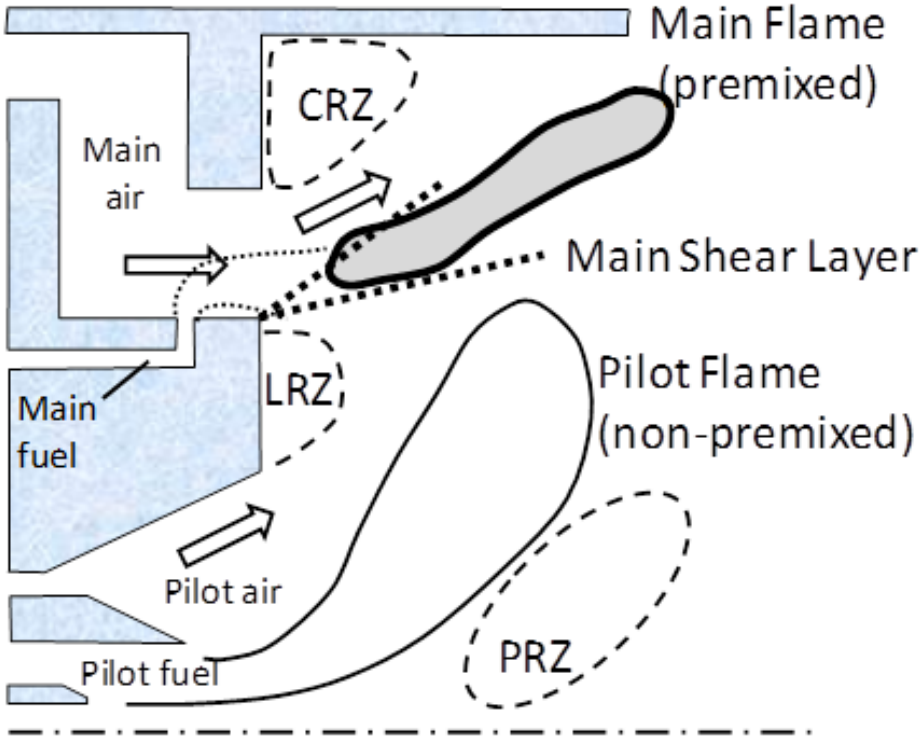

Figure 5.2: Illustration of the main components of the LPP fuel injector during operation. These features were measured using PIV and Formaldehyde PLIF and were published in[12]

the flame lifts off of the injector and compresses into a flat shape, shown in more detail in Figure 5.4. At times when the pressure is highest (frame 5), the flame reattaches and reforms into a conical, elongated structure, shown in more detail in Figure 5.5. Additionally the central thin spire of flame does not disappear at any point in the cycle, but does grow in width to fill the flame tube exit before shrinking again. These videos show that the flame exhibits large scale motion, changes in flame shape, and flame anchoring during the pressure oscillations.

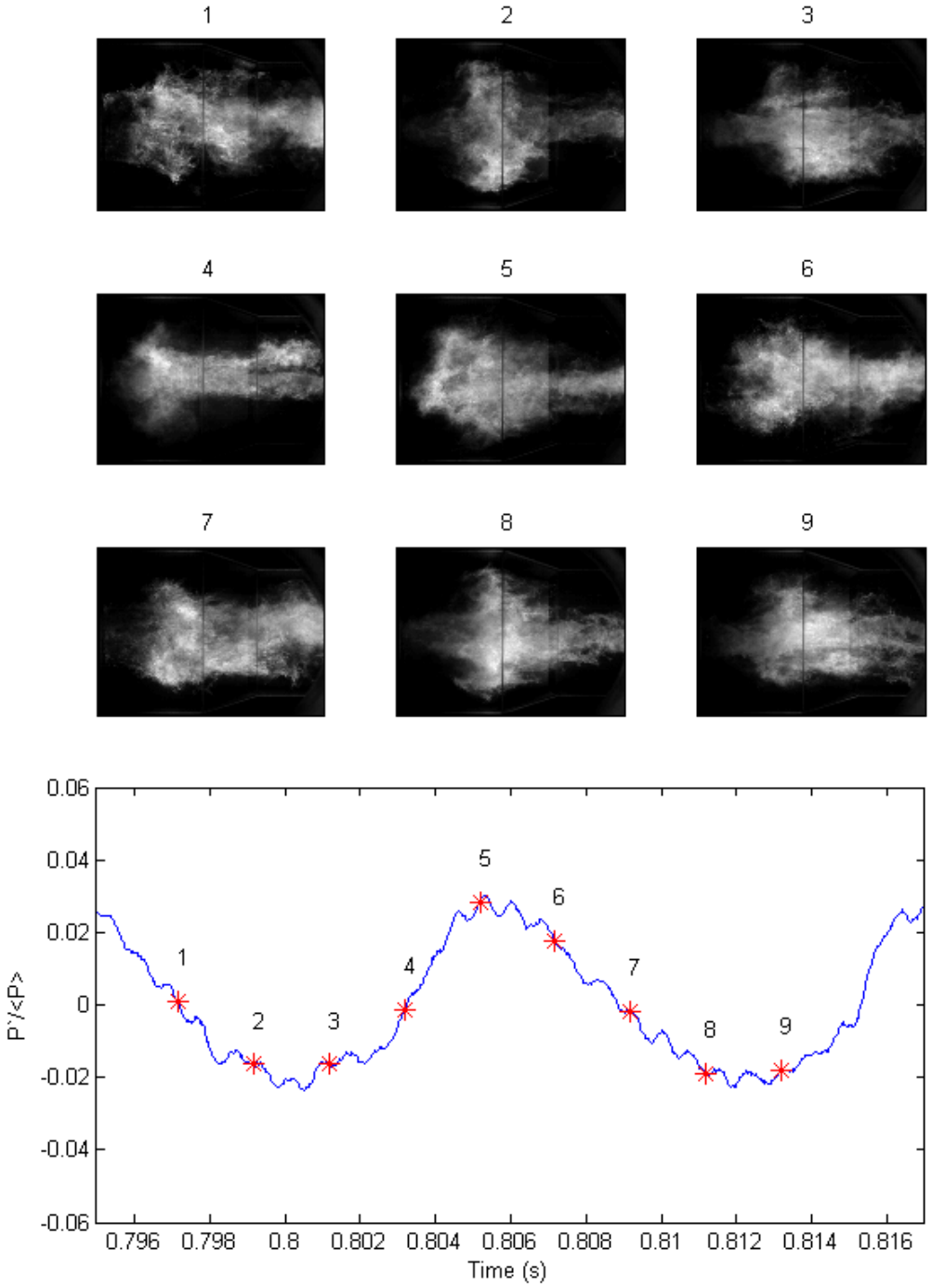

Figure 5.3: Simultaneous high speed video and pressure trace. At low pressure the flame lifts off and compresses. At high pressure the flame reattaches and forms a conical shape.

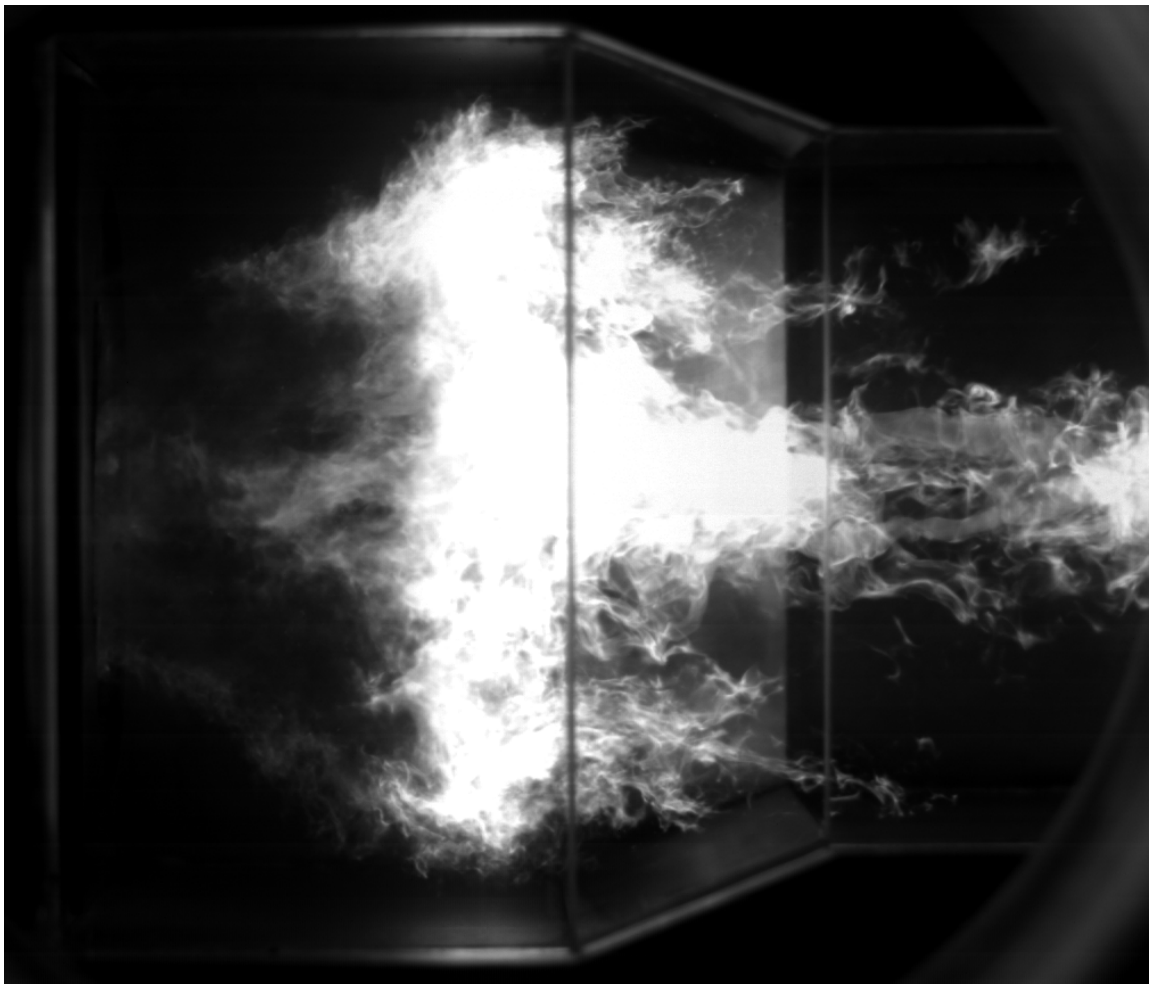

Figure 5.4: Closeup of representative video frame of a lifted flame at low pressure points in the combustion instability cycle. The flame exhibits a lifted flattened structure.

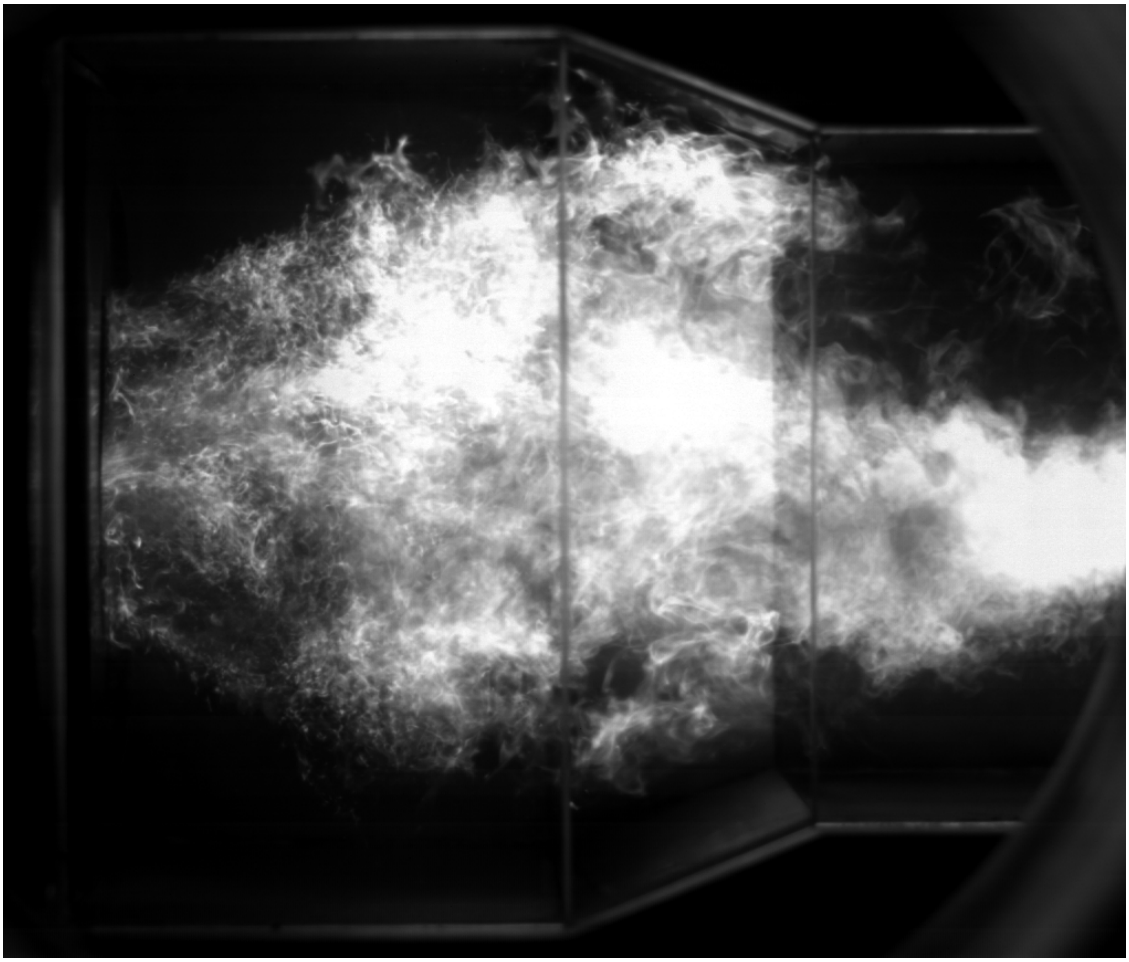

Figure 5.5: Closeup of representative video frame of an attached flame at high pressure points in the combustion instability cycle. The flame exhibits a conical, attached structure.

5.3 Other Quantities Measured from High Speed Videos

Visual inspection of the high speed video frames determined two quantities of interest which appeared to have a cyclical behavior: the flame liftoff height and the flame width at the exit of the flame tube. These parameters are shown in Figure 5.6 as visually determined for an example video frame.

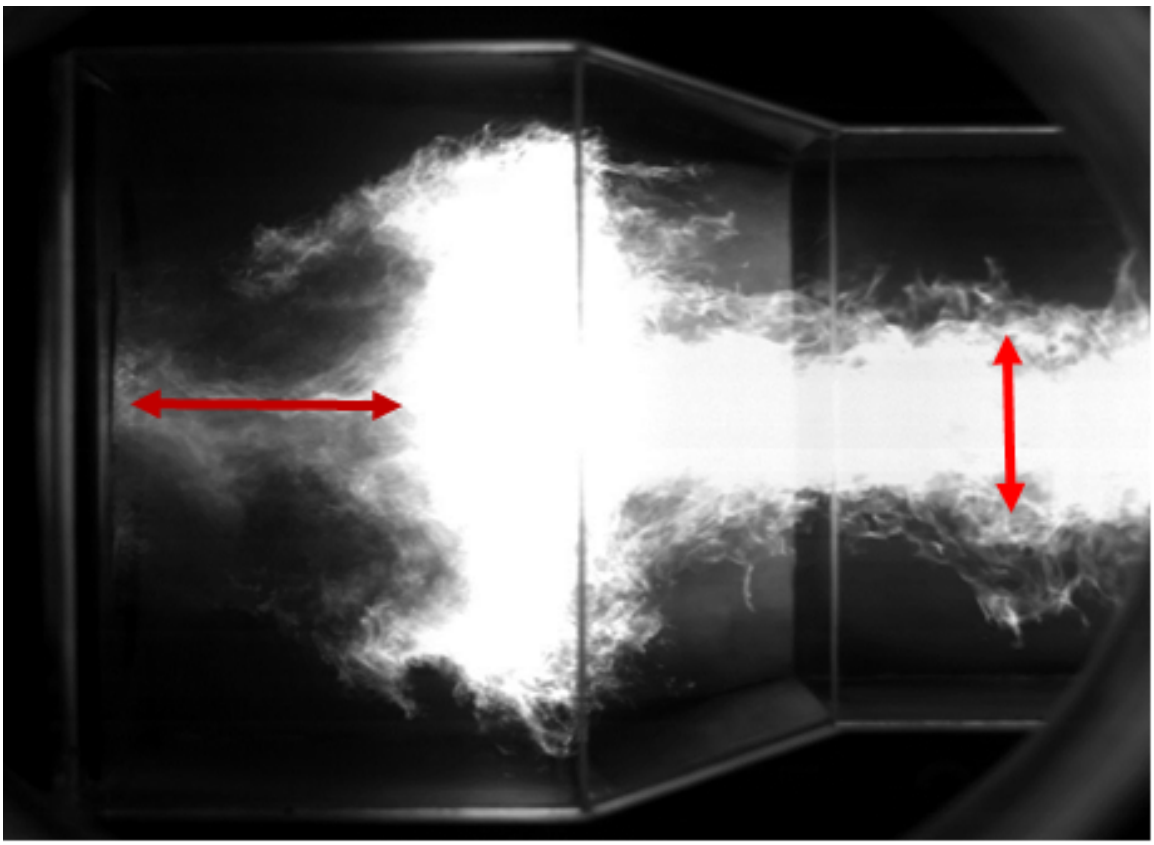

Figure 5.6: Flame liftoff height and the flame width indicated by red arrows on the example from Figure 5.1

The observed periodic motion can be quantified by measuring a these two quantities in each frame. First, the chemiluminescence in each image was integrated in the transverse (vertical) direction to obtain a plot of intensity versus the streamwise (horizontal) direction. The flame liftoff height is defined as the x-location where this curve has increased to 75% of its maximum value. Similarly, the width of the flame at

the flame tube exit was calculated by integrating in the streamwise direction within the final third of the combustor. The width is measured at 50% of the maximum resulting value. These calculations are shown visually for two example frames in Figure 5.7. Additionally, the total luminosity is integrated per frame. The result of these calculations is a time history of the flame behavior which can be analyzed to determine its frequency response.

Figure 5.8 shows simultaneous traces of pressure, flame lift off height and the intensity of the flame luminosity. The flame height is determined to be 180 degrees out of phase with the pressure oscillations, similar to the observations of the video frames earlier. The intensity of the flame chemiluminescence is included because it is proportional to the total heat release rate [30]. The intensity and thus the heat release rate lag behind the pressure but lead the flame height response. The mean liftoff height is 40.5 mm with an average fluctuation of $\pm$ 7.75 mm. The total distance of the flame motion is about 15% of the flame tube length. Additionally, the speed at which the flame moves away from the injector face is about 2.6 m/s, which is considerably less than the speed at which it returns (approximately 8.6 m/s). This is an indicator that flashback of the lifted flame base plays a role in accelerating the flame motion, which can alter the frequency of the oscillation.

Figures 5.3 and 5.8 give strong evidence that an "equivalence ratio" oscillation occurs due to the mass flow rate of air changing in time. This is different from the more common equivalence ratio oscillations studied in rockets where the fuel flow rate changes in time. In these rocket studies [2], the fuel flow rate reacts to large changes in the combustion chamber pressure and can be avoided by having fuel feed pressures large enough that the pressure drop across the fuel injector is greater than twice the pressure oscillations. In this study, the 6.9 to 13.8 kPa fluctuations are

much less than the pressure drop across the fuel injector. Additionally, the high speed images in Figure 5.3 show fast, large scale motion of the flame. The only logical way that the flame base would rapidly move downstream is if the air flow rate rapidly increased, which would cause an increase in the liftoff height. The rapid upstream movement of the flame is also logically explained by a decrease in the air flow rate, which allows the flame to flash back.

Frequency analysis was conducted on the measured flame width, flame liftoff height, and intensity of the flame luminosity. The resulting spectra are shown in Figure 5.9 along with the spectra of the simultaneous pressure trace. In all four plots, the 80 and 160 Hz peaks are present clearly indicating that the low frequency instability is coupled to the flame response.

To summarize the high speed video results, the videos show that the flame lifts off and flashes back over a large distance, which is best explained by an equivalence ratio oscillation. An equivalence ratio oscillation in this case must be due to large oscillations in air flow rate since the fuel flow rate does not oscillate. Air flow rate oscillations would cause the large scale flame motions that were observed. Further evidence of air flow oscillations from the phase averaged PIV data will be discussed in Section 7.3.

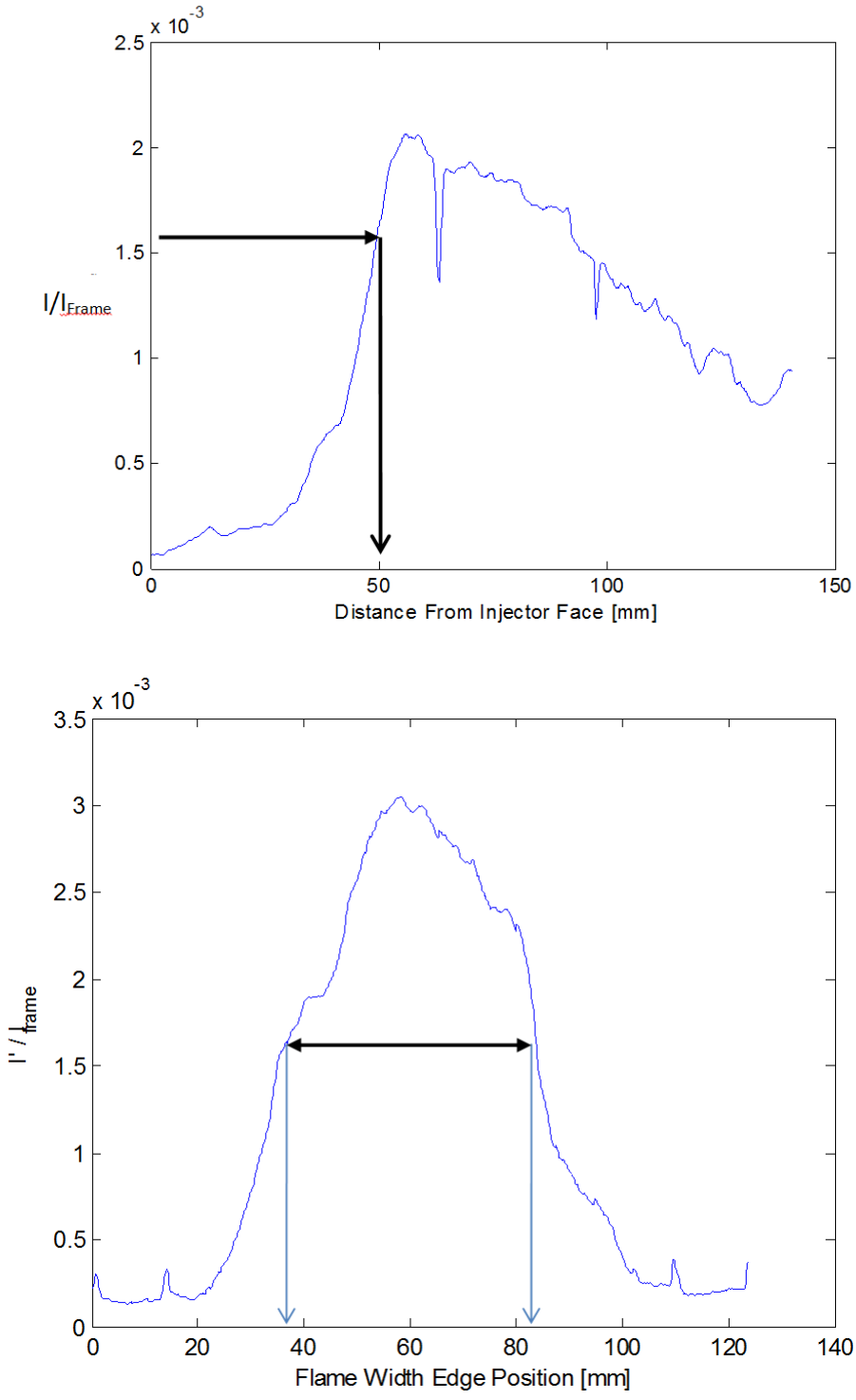

Figure 5.7: Example flame front location and width calculations from high speed video frame. A- Flame fronts were determined to occur at 75% of the rise in luminosity in the axial direction. B- Flame width is determined from a similar calculation but is taken to be at the full width half maximum (FWHM)

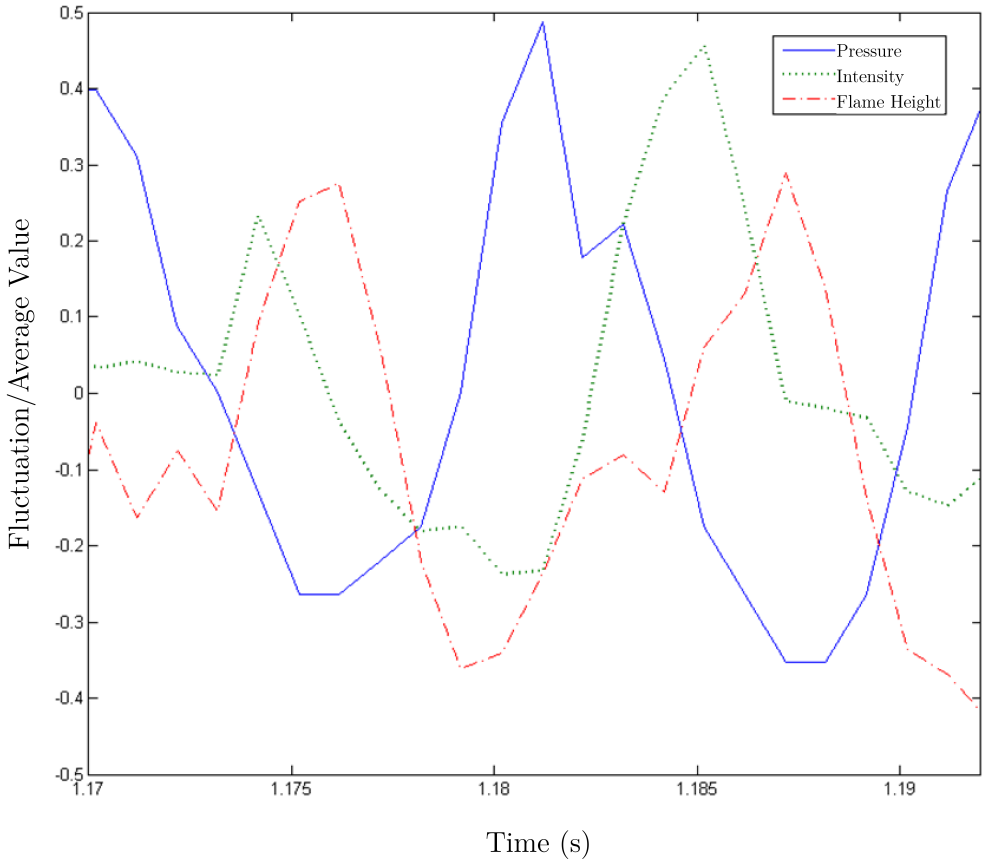

Figure 5.8: Resulting time history of flame liftoff height shown with pressure and intensity of the flame luminosity.

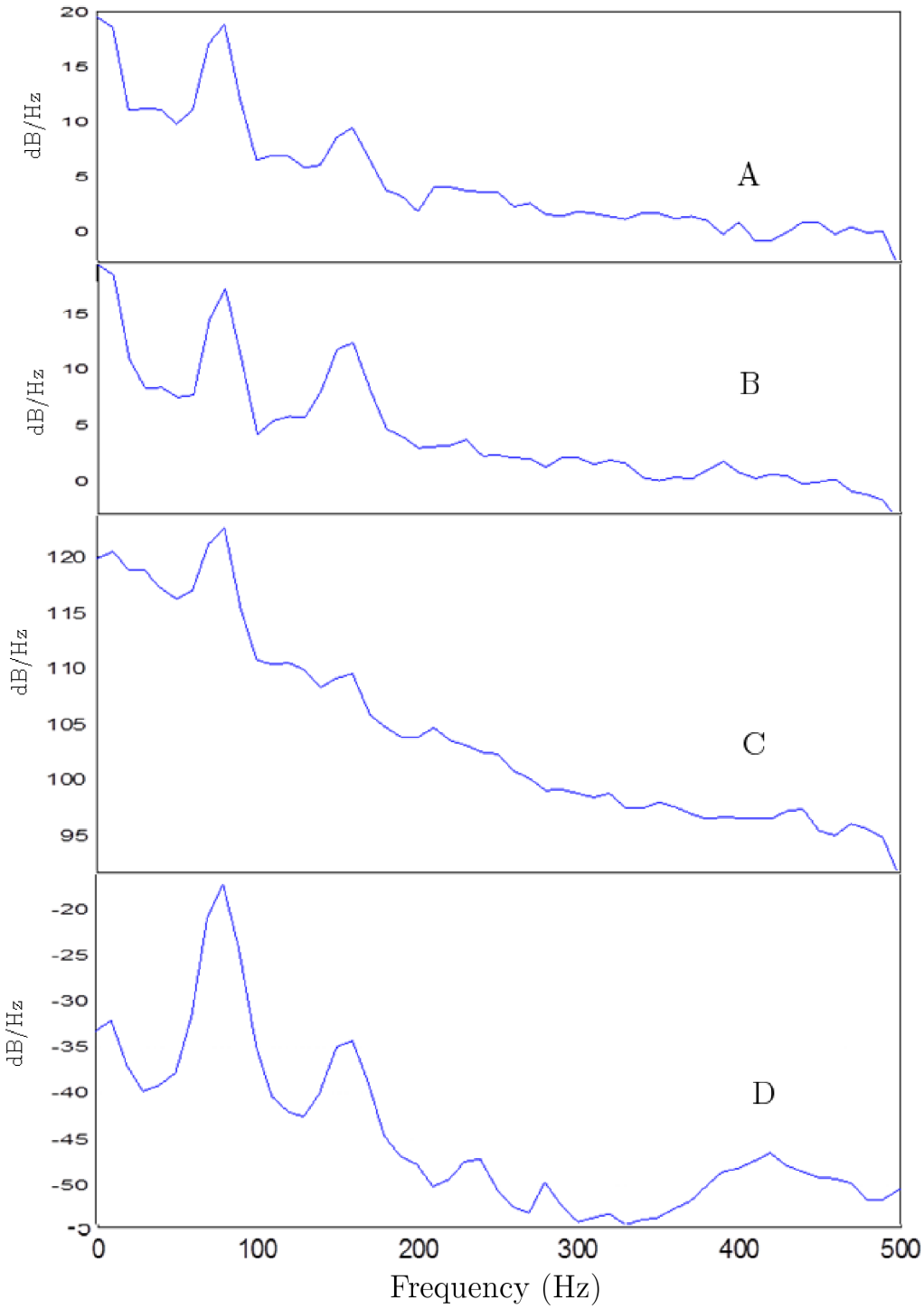

Figure 5.9: Spectra of four measured quantities showing similar 80 Hz peaks. Spectra correspond to A- Flame width, B- Flame liftoff height, C- Intensity of the flame luminosity, D- Pressure

5.4 Centroid of Heat Release and Rayleigh Index

Two quantities that are useful metrics which can be used to guide future simulations are the centroid of heat release and the Rayleigh Index. Both of these quantities provide information about the spatial and temporal distribution of the heat release and how it couples with the pressure field.

The weighted centroid of heat release was measured for each frame of the video. A time history is shown in Figure 5.10 and the corresponding PSD is shown in Figure 5.11. The centroid of heat release provides information about where the majority of heating from the flame occurs. The x location of the centroid displays 80 and 160 Hz oscillations. This is important because the Rayleigh criterion, which states that, at a location, if the pressure and heat release are in phase the instability will be amplified. This can be quantified in a Rayleigh Index [56] which is given by Equation 5.1. A 2D image of this index provides an indication of regions which are amplifying or dampening the oscillations and the relative strength of these effects.

$$RI = \frac{1}{T}\int_0^T \frac{p\prime q\prime}{p_{rms}\bar{q}}\,\mathrm{d}t \tag{5.1}$$

Figure 5.12 shows the Rayleigh Index determined using Equation 5.1 for the observed oscillations. The injector is at the left side of the image and flow is to the right. Three major features are observed which roughly correspond to the three sections of the flame tube. Near the injector there is a region of large positive values which is the main driver of the instability. In the neck down section there is a large region of dampening. And in the exit there is a small region of slightly positive values. The majority of the amplification is in the first section of the flame tube, as expected since this is the location of the flame motion discussed previously.

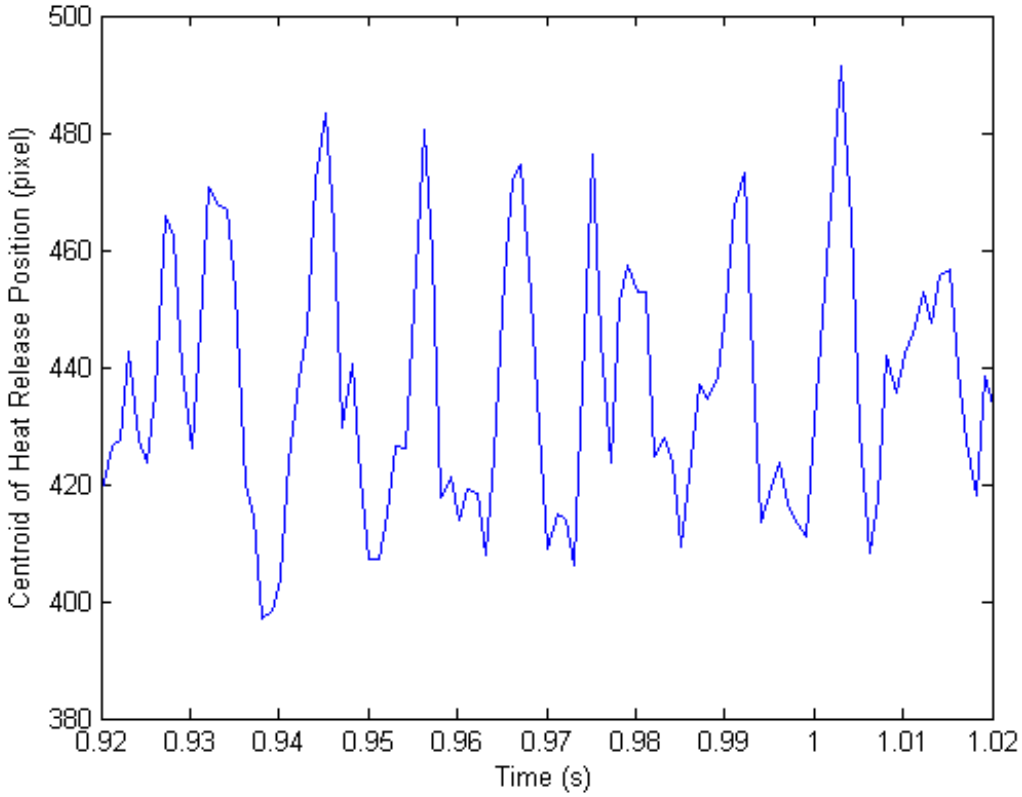

Figure 5.10: Time history of the centroid of heat release showing periodic behavior.

This can be compared to the low frequency instability previously studying with a similar injector [12]. The Rayleigh Index plot for the incipient blowout instability at the same chamber pressure and air mass flow rate, but with much less fuel, is shown in Figure 5.13. Note that this instability is near the lean blow-out and is partially dependent on the flame interaction between the pilot and the main flame. In this case there is no dampening anywhere in the system. Near the injector the values are much smaller than at the outer edges of the flame, especially in the region where the two flames interact. This is almost the direct opposite of the 80 and 160 Hz instability in Figure 5.12. Thus while flashback plays a role in both instabilities, the Rayleigh Index shows fundamental differences in how the instability arises. In

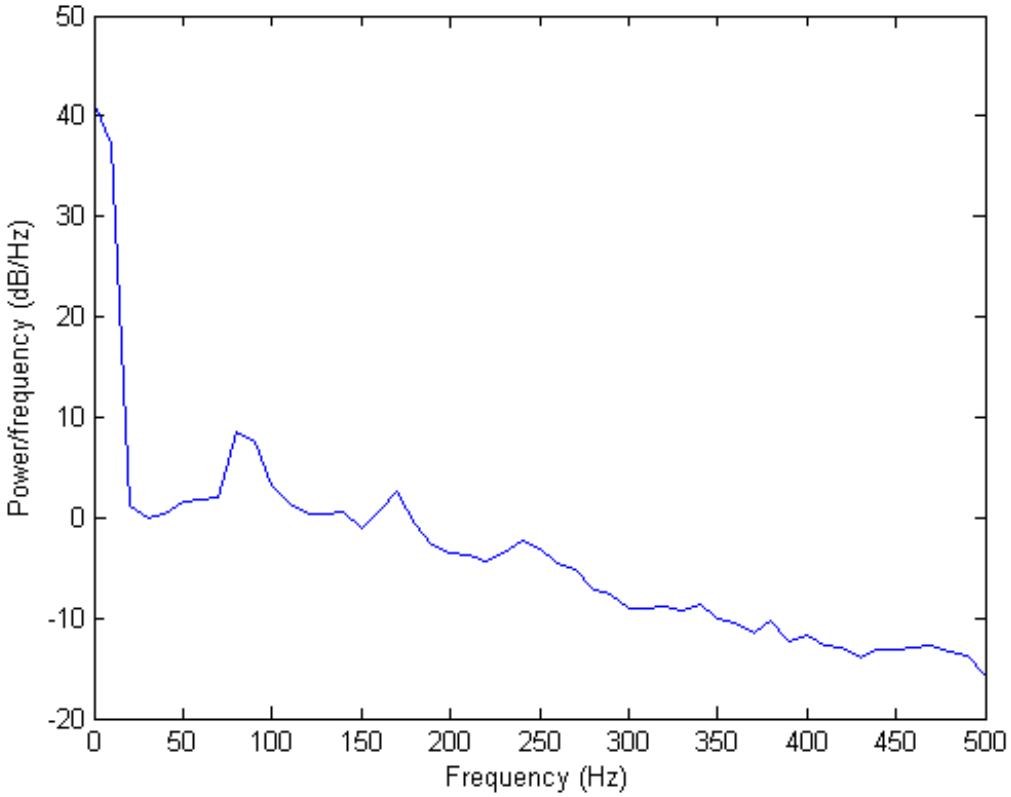

Figure 5.11: PSD of the centroid of heat release showing 80, 160 and 240 Hz peaks.

the case of the incipient blowout, the instability is initially forced at the outer edges of the flame and flashback occurs along the walls, as seen in the high speed video. In the low frequency instability, the flame motion is at the base of the flame and flashback occurs through the primary recirculation zone.

The centroid of heat release time history can also be used to filter the Rayleigh Index. A mean axial location of the centroid is determined. Frames of the movie are divided into two groups based on if the centroid for each frame is upstream or downstream of the mean location. The contribution to the Rayleigh Index for each of these groups is shown in Figures 5.14 and 5.15 respectively. The first group which has centroids upstream of the average is typical of an "attached" pilot flame. In this

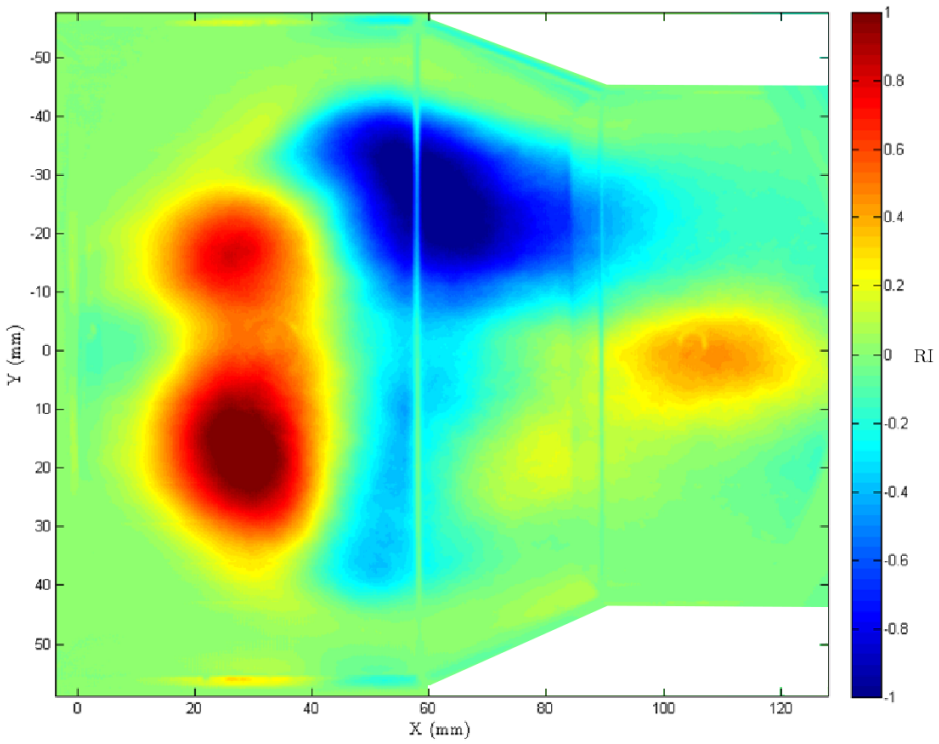

Figure 5.12: Rayleigh Index for the LPP combustor. The injector is at the left of the image and flow is to the right. There are three main features, a large positive region near the injector, a broad negative region near the neck down section and a small positive region in the exit of the flame tube.

case the flow features seen in the overall Rayleigh Index are present but at much lower magnitudes. The second "lifted flame" group also shows the same features but at magnitudes much closer to the total value. This indicates that the portion of time that the flame spends in a "lifted" mode of operation is the main contributor to the amplification of the instability mode.

Therefore, the measured oscillations of the centroid of heat release provide a useful metric to aid future simulations. This metric quantifies the observed distance of liftoff and flashback. Additionally, Rayleigh Index provides information about the locations within the burner which are driving the instability. The filtered Rayleigh Index shows

that the lifted flame portion of the instability cycle is the main contributor to the amplification of the oscillations.

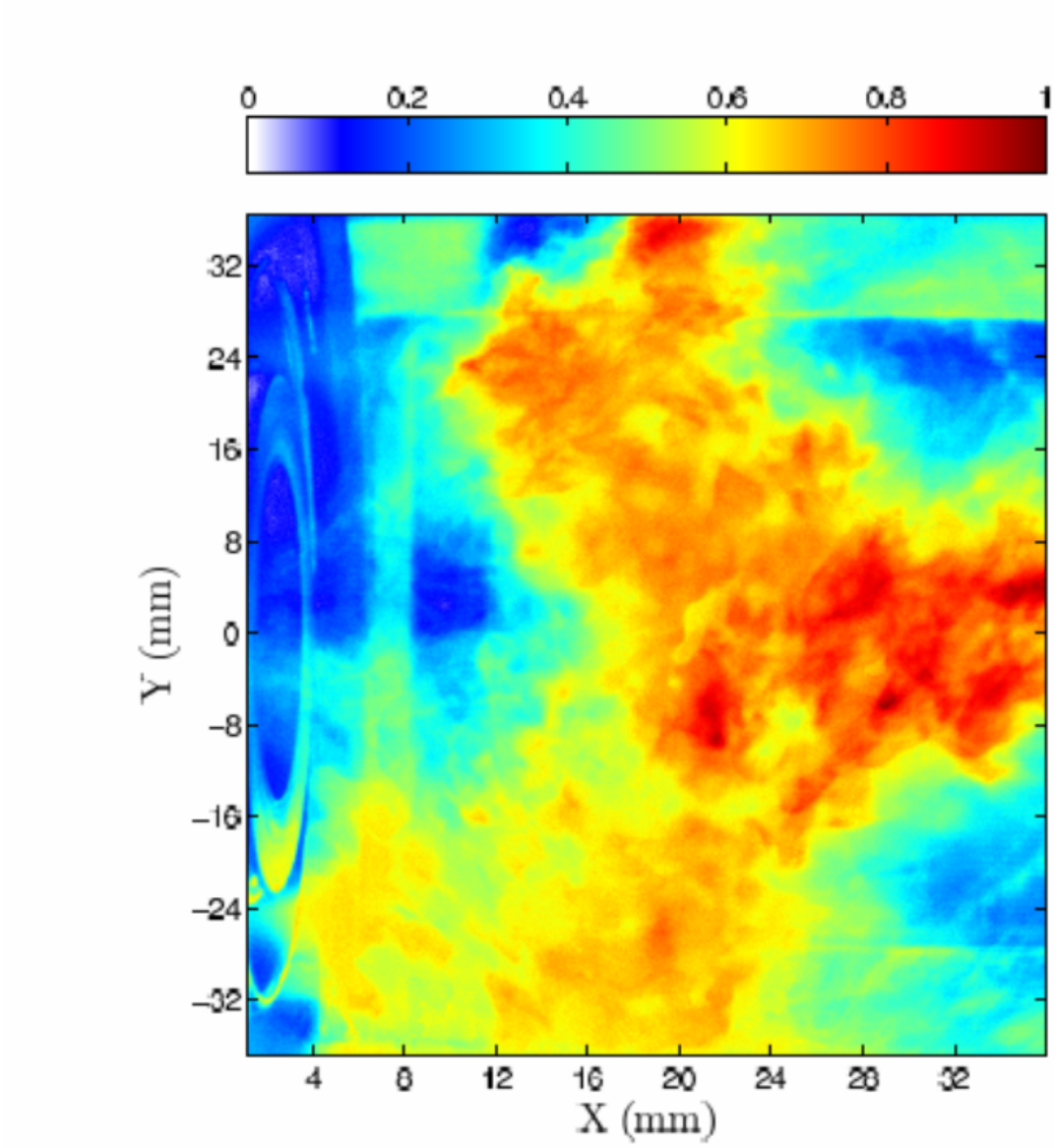

Figure 5.13: Rayleigh Index plot from (Dhanuka et al. [12]). This instability shows amplification everywhere and the highest amplification regions are at the outer edges of the flame, especially near the location of pilot/main flame interaction.

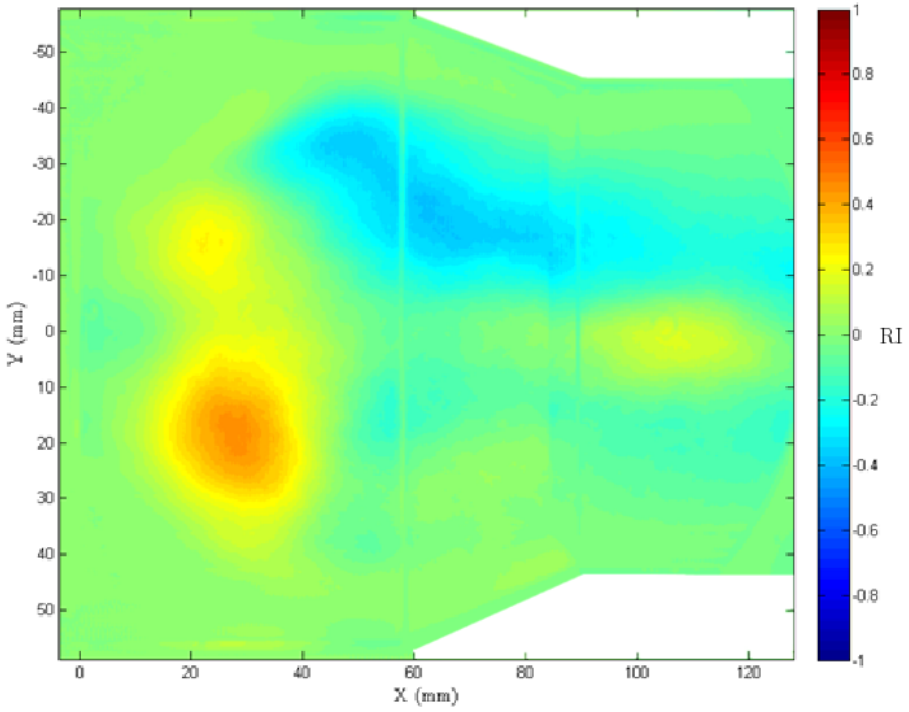

Figure 5.14: Contribution to Rayleigh Index from times when the flame's centroid of heat release is upstream of its time averaged location (i.e. it is "attached"). Note the overall smaller magnitudes. than in Figure 5.12.

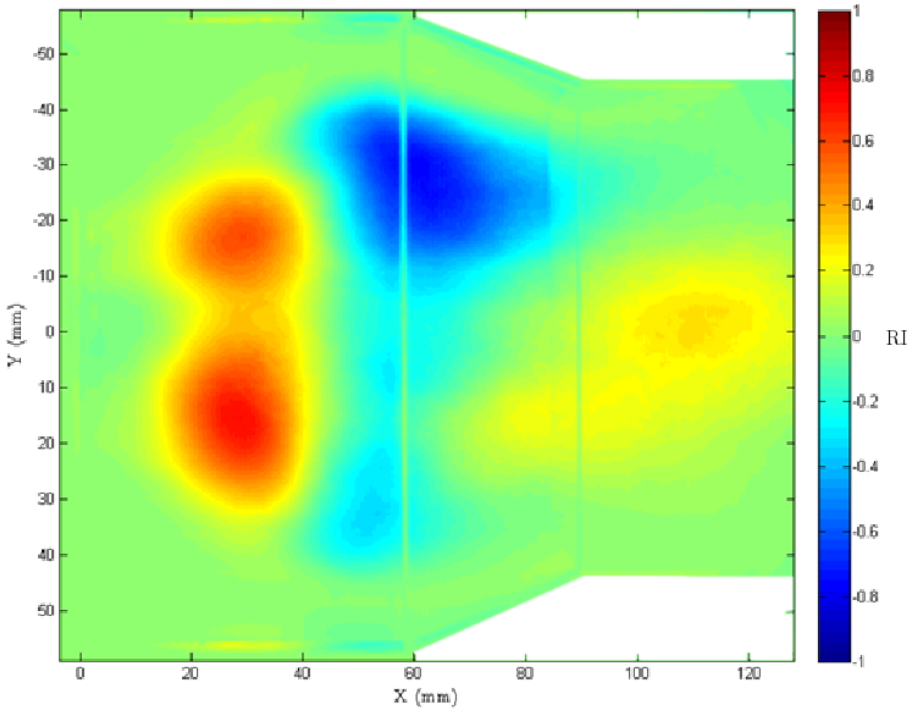

Figure 5.15: Contribution to Rayleigh Index from times when the flame's centroid of heat release is downstream of its time averaged location (i.e. it is "lifted"). Note that the values are only slightly smaller magnitudes than the full index values in Figure 5.12.

CHAPTER VI

Acoustic Analysis

6.1 Introduction

One of the goals of this thesis work was to determine which physical mechanism is the cause of the engine growl associated with the commercial LPP fuel injector. Based on the results of the simultaneous high speed video and pressure discussed in Chapters 4 and 5 the low frequency pressure and flame oscillations can be characterized as a bulk mode Helmholtz resonator. However, altering the physical geometry of the test section as discussed in 4.6 did not identify the source of these bulk Helmholtz modes. This section details an acoustic analysis of the source of the 80 and 160 Hz combustion instabilities. It was decided not to run an acoustic code such as COMSOL for two reasons. First, the flame was found to be necessary to excite any acoustics at the frequencies of interest and a flame cannot be properly simulated in commercial acoustic codes. Second, since the data proved that Helmholtz resonance was the source, the only unknown is what geometric dimensions (volume, neck area and length) are responsible.

6.2 Derivation of Governing Equation

The results discussed in 4.6 showed that the Helmholtz bulk mode must originate in the fuel injector and flame tube because the lengths and volumes of the surrounding

pressure vessel were varied and no changes were observed in the frequency of the instability. As seen in Figure 6.1 there are three possible throat areas for a Helmholtz mode corresponding to the three air swirlers. Additionally the flame tube serves as the volume for the Helmholtz mode.

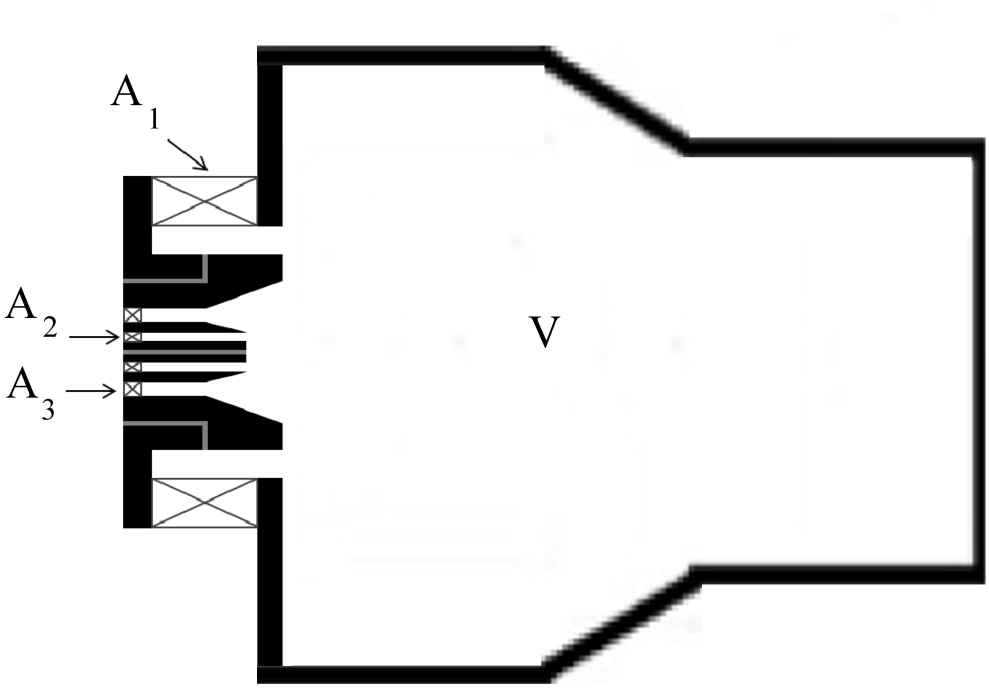

Figure 6.1: Possible physical parameters for a Helmholtz type oscillation.

A general multi-neck Helmholtz resonator is shown in Figure 6.2. This simple acoustic problem has been solved before; however it was re-derived and further simplified by a few assumptions which arise from the current problem. This analysis of a multi-neck Helmholtz resonator differs from the standard Helmholtz formulation in two ways. First, there is a mean flow through the system. As derived by Rienstra and Hirschberg [58], this mean flow will introduce a damping effect but will not affect the natural frequency of the oscillations. Second, this model has three neck openings rather than the standard one opening. Therefore, the following derivation is made

for the coupled system. As seen in Figure 6.2 there is a mass in each neck which is expressed in Equation 6.1 as the product of the density of the fluid in the neck and the cross sectional area A_i and the length L_i. Additionally, the initial unperturbed pressure is equal to the exterior pressure P_∞. When the fluid in the neck moves a distance x_i, it compresses or expands the interior volume by some amount given by Equation 6.2. Because the oscillations are an adiabatic process, the pressure change in the vessel is related to the volume change by Equation 6.3. Therefore the force balance on the mass in a given neck can be expressed as the pressure differential and therefore the volume change as in Equation 6.4.

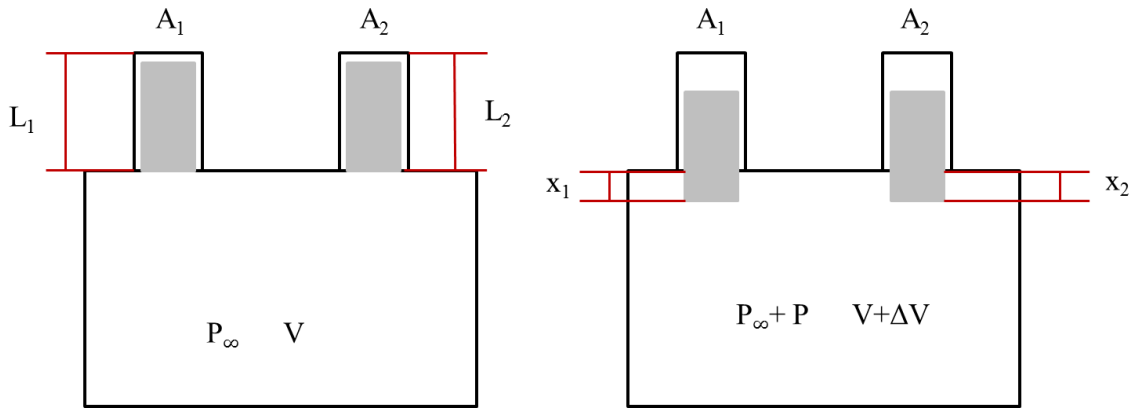

Figure 6.2: General multi-neck Helmholtz resonator

(6.1) $$m_i = \rho A_i L_i$$

(6.2) $$\Delta V = \sum A_i x_i$$

(6.3) $$\frac{P}{P_\infty} = -\gamma \frac{\sum A_i x_i}{V}$$

$$F_i = PA_i = (\frac{-\gamma P_\infty \sum A_i x_i}{V})A_i \tag{6.4}$$

For each neck, these relations are substituted into Newton's second law to obtain a governing equation for the motion of the mass of fluid in each neck. Because two major frequency peaks are observed in the pressure and flame oscillations, the system of equations was simplified to include only two necks.

$$F_i = m_i \frac{d^2 x_i}{dt^2} \tag{6.5}$$

$$\frac{d^2 x_i}{dt^2} = \frac{F_i}{m_i} = \frac{(\frac{-\gamma P_\infty \sum A_i x_i}{V})A_i}{\rho A_i L_i} \tag{6.6}$$

$$\frac{d^2 x_1}{dt^2} = \frac{-\gamma P_\infty}{\rho} \frac{A_1 x_1 + A_2 x_2}{L_1 V} \tag{6.7}$$

$$\frac{d^2 x_2}{dt^2} = \frac{-\gamma P_\infty}{\rho} \frac{A_1 x_1 + A_2 x_2}{L_2 V} \tag{6.8}$$

Noting that the definition of the speed of sound in Equation 6.9 and the definition of the natural frequency of a Helmholtz oscillator in Equation 6.10, the two coupled equations can be simplified to 6.11 and 6.12.

$$c^2 = \frac{\gamma P}{\rho} \tag{6.9}$$

$$\omega = c\sqrt{\frac{A}{LV}} \tag{6.10}$$

$$\frac{d^2x_1}{dt^2} + \omega_1^2 x_1 = -c^2 \frac{A_2 x_2}{L_1 V} \tag{6.11}$$

$$\frac{d^2x_2}{dt^2} + \omega_2^2 x_2 = -c^2 \frac{A_1 x_1}{L_2 V} \tag{6.12}$$

In the current system both necks have the same length which further simplifies the system to the following.

$$\frac{d^2x_1}{dt^2} = -(\omega_1^2 x_1 + \omega_2^2 x_2) \tag{6.13}$$

$$\frac{d^2x_2}{dt^2} = -(\omega_2^2 x_2 + \omega_1^2 x_1) \tag{6.14}$$

Therefore the system behaves as two coupled simple harmonic oscillators which will produce oscillations at the natural frequency of each neck ω_1 and ω_2. Additionally, there is an expected overtone which arises from the coupled nature of these equations. If a new variable z is defined as in Equation 6.15 then the coupled system can be rewritten in terms of z.

$$z = \omega_1^2 x_1 + \omega_2^2 x_2 \tag{6.15}$$

$$\frac{d^2z}{dt^2} = -(\omega_1^2 \frac{d^2x_1}{dt^2} + \omega_1^2 \frac{d^2x_2}{dt^2}) \tag{6.16}$$

Substituting in Equations 6.13, 6.14 and 6.15, a single second order differential is formed which has a natural frequency of $\sqrt{\omega_1^2 + \omega_2^2}$.

$$\frac{d^2z}{dt^2} = -(\omega_1^2 + \omega_1^2)\, z \tag{6.17}$$

A final correction is added for the length of the neck. Generally, the fluid in the neck moves past the ends of the channel and also induces some motion on a small amount of fluid outside the edges of the neck. Therefore a correction factor δ is added to the equation as follows:

$$\omega^2 = c\sqrt{\frac{A}{(L+\delta)V}} \tag{6.18}$$

Values for the end correction δ vary between 0.6 and 0.8 times the radius of the neck depending on the geometry [24]. For the current setup, a value of 0.6 time the radius was used.

6.3 Comparison to Experimental Results

Throughout all of the current experiments, an 80 and 160 Hz frequency oscillation was observed in the pressure field and flame response. Assuming these frequencies are ω_1 and ω_2, it would follow that the overtone of would be approximately 179 Hz and due to its proximity to the 160 Hz peak may not be seen as a distinct peak in the power spectral density plots. As discussed previously in Figure 6.1 there are three possible necks. Therefore natural frequencies for each were calculated based on their dimensions listed in Table 6.3. In all cases the volume is that of the entire flame tube and is equal to $1.7 * 10^{-3}\, m^3$ and the speed of sound is 432 m/s.

Table 6.3 shows that the neck area and length of the inner and outer pilot yield an expected Helmholtz resonance frequency of 84 and 174 Hz, respectively. This agrees with the measured frequencies. This coupled with the other results shown

Neck	Area	Length	Expected Frequency
	m^3	m	Hz
Main Swirler	$1.59 * 10^-3$	0.0416	326
Inner Pilot	$8.48 * 10^-5$	0.0335	84
Outer Pilot	$3.90 * 10^-4$	0.0356	174

Table 6.1: Calculated Helmholtz frequencies

in this dissertation strongly suggest that the pilot air supply is the source of the 80 and 160 Hz oscillations seen in the pressure field and combustion dynamics. This correlates well with the observed fact that the instability occurs with or without main fueling. Additionally, as discussed in Section 4.6, Figure 4.16 reducing the area of the main swirler to zero resulted in the disappearance of the 80 and 160 Hz peaks. As mentioned previously, having a mean through flow in the system produces a dampening effect [58]. As the velocity of the mean flow increase so does the amount of damping. Thus when the main swirler is completely blocked the system is over damped in regard to the 80 and 160 Hz oscillations. This analysis however does not explain the slight change in frequency observed when the main air swirler is only half covered.

CHAPTER VII

Simultaneous Particle Image Velocimetry , High Speed Chemiluminescence and Pressure Measurements

7.1 Introduction

The previous chapters describe the identification of a low frequency combustion instability at 80 and 160 Hz and show time resolved video of the flame response to the pressure oscillations at these frequencies. These results suggest that the oscillation of the air mass flow rate is the source of the equivalence ratio oscillations that amplify the combustion instability. In order to confirm this hypothesis, direct measurements of the velocity field, and thereby the air mass flow rate, were necessary. Additionally, a method was devised to phase average the PIV results. Phase-averaging was done in post-processing. Hundreds of PIV images were recorded at random times during the 80 Hz combustion oscillation and the phase angle was recorded for later data processing.

7.2 Time Averaged Field

In order to further investigate the cause of the low frequency instability, simultaneous PIV, high speed chemiluminescence and pressure measurements were performed. Figure 7.1 shows the mean velocity field and Figure 7.2 shows the mean field for a similar case measured in a previous work (Dhanuka et al. [13]). Both sets of data

clearly show the two separate air streams from the inner and outer swirlers. While the data of Dhanuka et al. show the flow features near the centerline, including the center recirculation zone and lip recirculation zone, the current data also includes the corner recirculation zone and tip of the jet where it impacted the flame tube wall. This larger field of view was made possible because a rectangular quartz flame tube replaced the previous flame tube which had small circular windows.

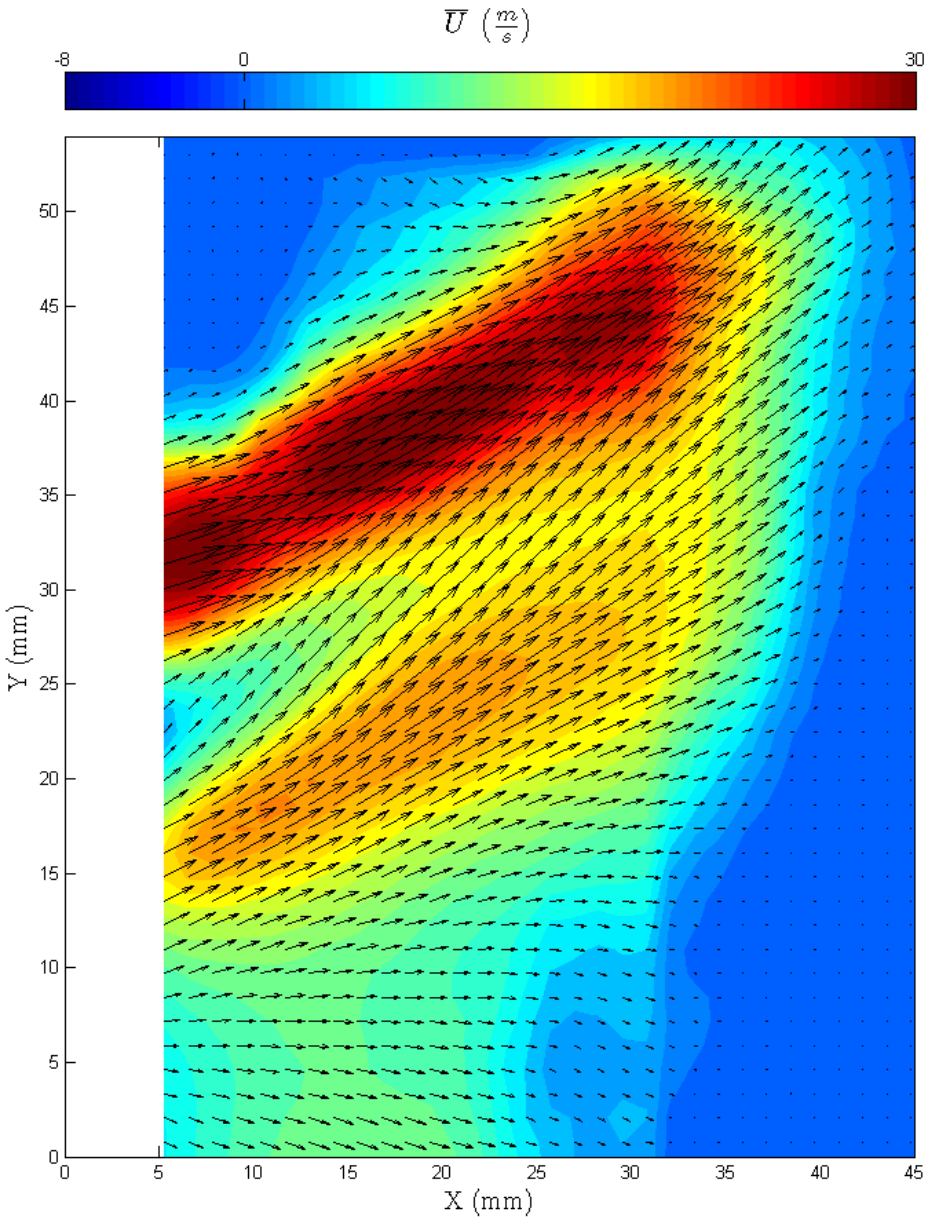

Figure 7.1: Mean velocity field for the current experiment in the vicinity of the main and pilot air streams. Flow is left to right and the top half of the symmetric flow is shown (the centerline is at Y = 0 mm). Of note are the separate main and pilot air streams with the main being much faster than the pilot.

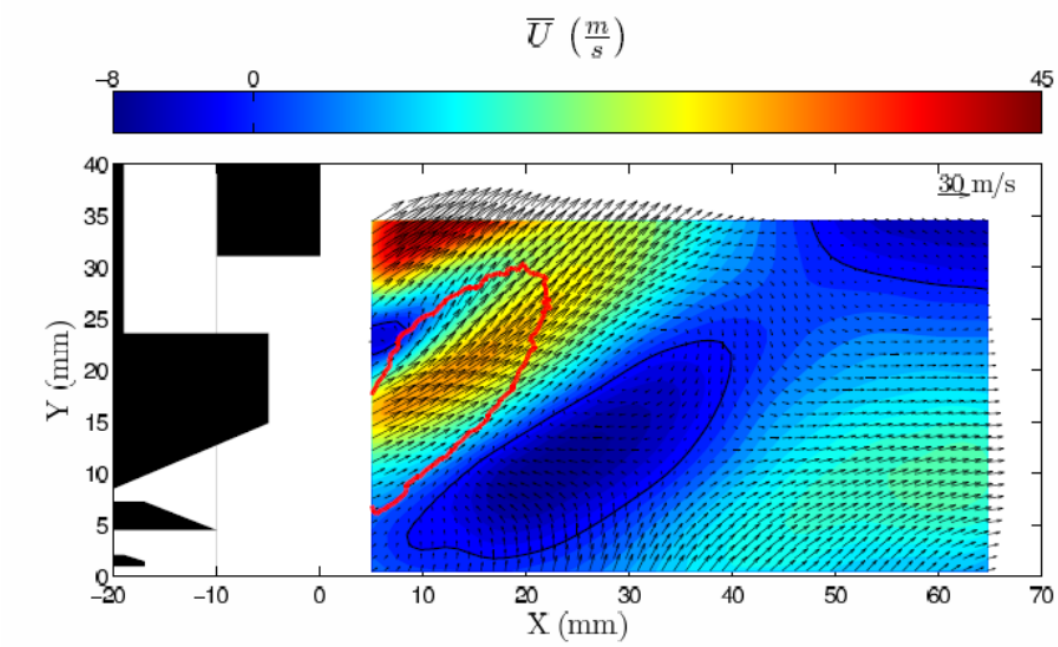

Figure 7.2: Mean Velocity field from Dhanuka et al. [13] with overlaid Pilot flame position shown in red.

7.3 Phase Averaged Results

The PIV results were phase averaged based on the phase angle of the pressure trace for each PIV velocity field. Initially, all of the PIV images were phase averaged. However, this produced inconsistent results because the instability is intermittent. Analysis of the simultaneous high speed video taken at 675 Hz indicated that the low frequency flame motion occurred in 60% of the PIV fields. Thus the PIV data was selectively filtered in order to investigate only those times at which the flame is clearly undergoing a cycle. A phase angle was determined for each vector field as illustrated in Figure 7.3. The red symbols indicate locations at 90 degrees phase angle and the green symbol is at 270 degrees phase angle. Then velocity fields were grouped into 20 degree bins and averaged within each bin.

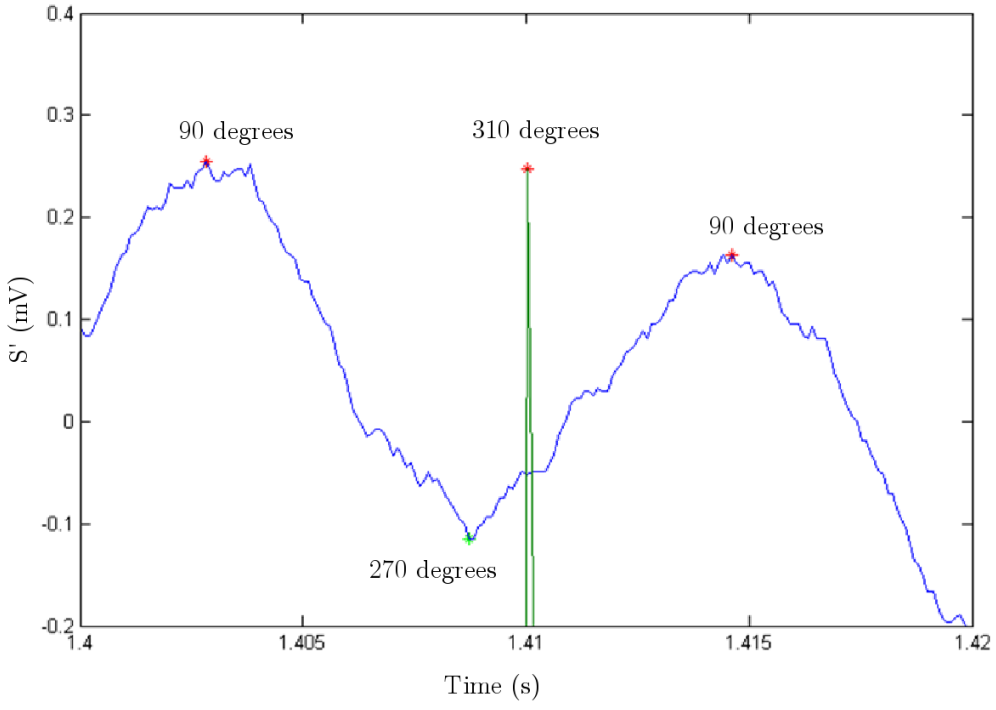

Figure 7.3: Example of the method to determine phase angle of the PIV vector field. The sinusoidal curve is the pressure trace and the single spike indicates when the PIV measurement was made.

Figure 7.5 shows the phase averaged velocity fields. The velocity fields at 0°, 180° and 360° generally match the mean velocity field shown in Figure 7.1. However, at 90° the speed within the main air stream slows significantly. Also, at 270° the main air stream speeds up significantly. These effects are shown in more detail in Figure 7.6. This indicates that the air flow rate through the outer main swirler is varying cyclically with the pressure and flame and agrees with the results discussed in Chapters IV and V. These effects can be quantified by calculating an average axial velocity in the region of the base of the main jet, denoted <U>. The region used for this average is shown in Figure 7.4. Figure 7.7 shows <U> as a function of pressure phase angle. The x-axis is the phase angle determined by the pressure trace. The green line is an 80 Hz sine wave with a 5 m/s amplitude and a 140 degree offset from the pressure phase angle. Therefore, the velocity of the main jet base appears to exhibit a sinusoidal behavior and lag the pressure by 140°.

Figure 7.8 shows phase averaged velocity profiles at an x location of 15 mm downstream of the injector face, which corresponds to the base of the jet. As a first approximation, the system is assumed to be fully symmetric. While the injector is designed to be symmetric, the presence of the mounting sting inherently adds a small amount of asymmetry to the injector. Therefore these profiles are then integrated using Equation 7.1 to determine a phase averaged air mass flow rate which is shown in Figure 7.9.

$$\dot{m} = \int_0^{2\pi} \int_0^R \rho\, U(r) r \, \mathrm{d}r \, \mathrm{d}\theta \tag{7.1}$$

The green line is a sine wave with an amplitude of 50 g/s and an offset of 150 degrees from the pressure phase angle. Aside form the one outlier at 105 degrees pressure phase angle, the air mass flow rate shows a cyclical pattern which lags the

pressure phase angle by 150°. From these results, it is concluded that the PIV data show that the bulk motion of the flame is causing an equivalence ratio oscillation that is due to oscillations in the air mass flow rate. This is in agreement with the analysis of the previous section; a Helmholtz resonance occurs which leads to oscillations in air velocity through the two annular pilot air openings. This finding is different from most previous studies. Many papers which cite equivalence ratio oscillations [35] [31] [29], find that they occur due to the oscillations influencing the incoming fuel stream. However, most of these tests were also done with gaseous fuels and laboratory type fuel injectors. While the current findings are important for the specific industrial injector investigated, they also can provide insight into similar industrial type designs and help to translate the results of the laboratory scale devises into industrial applications.

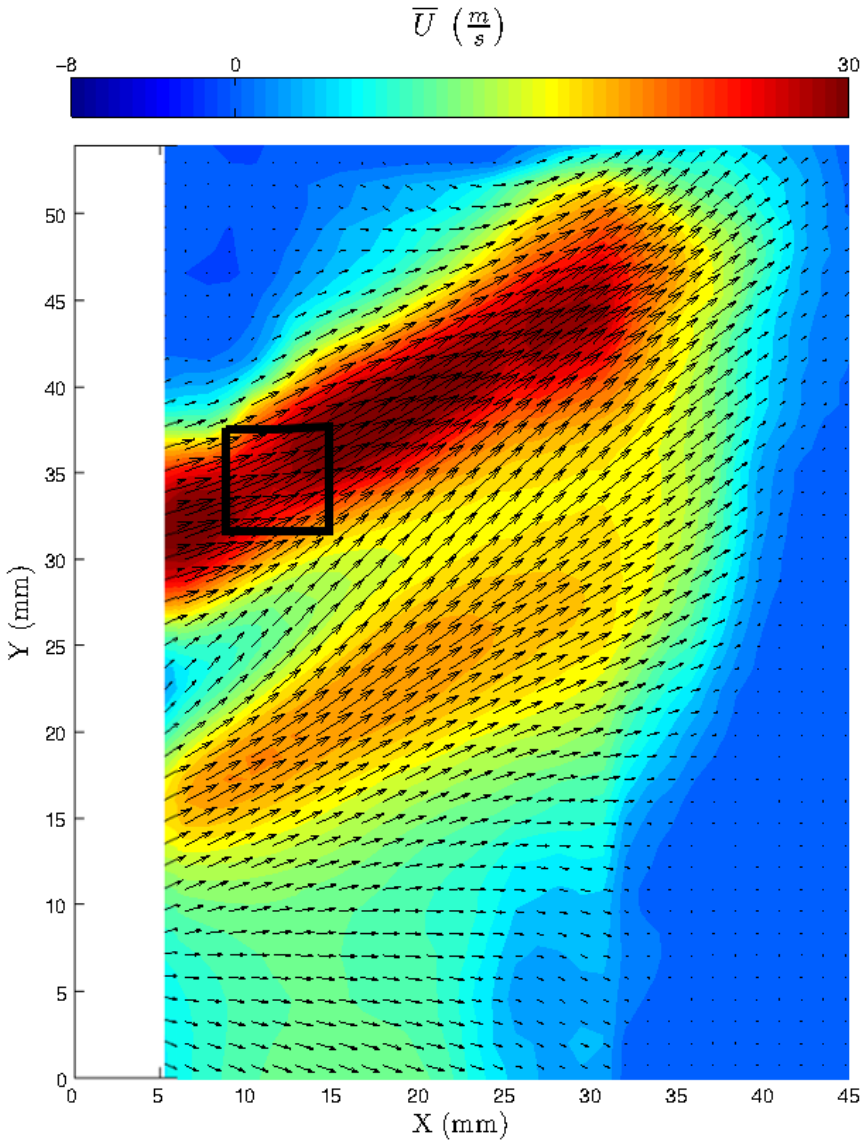

Figure 7.4: Region over which Local Velocity <U> is measured.

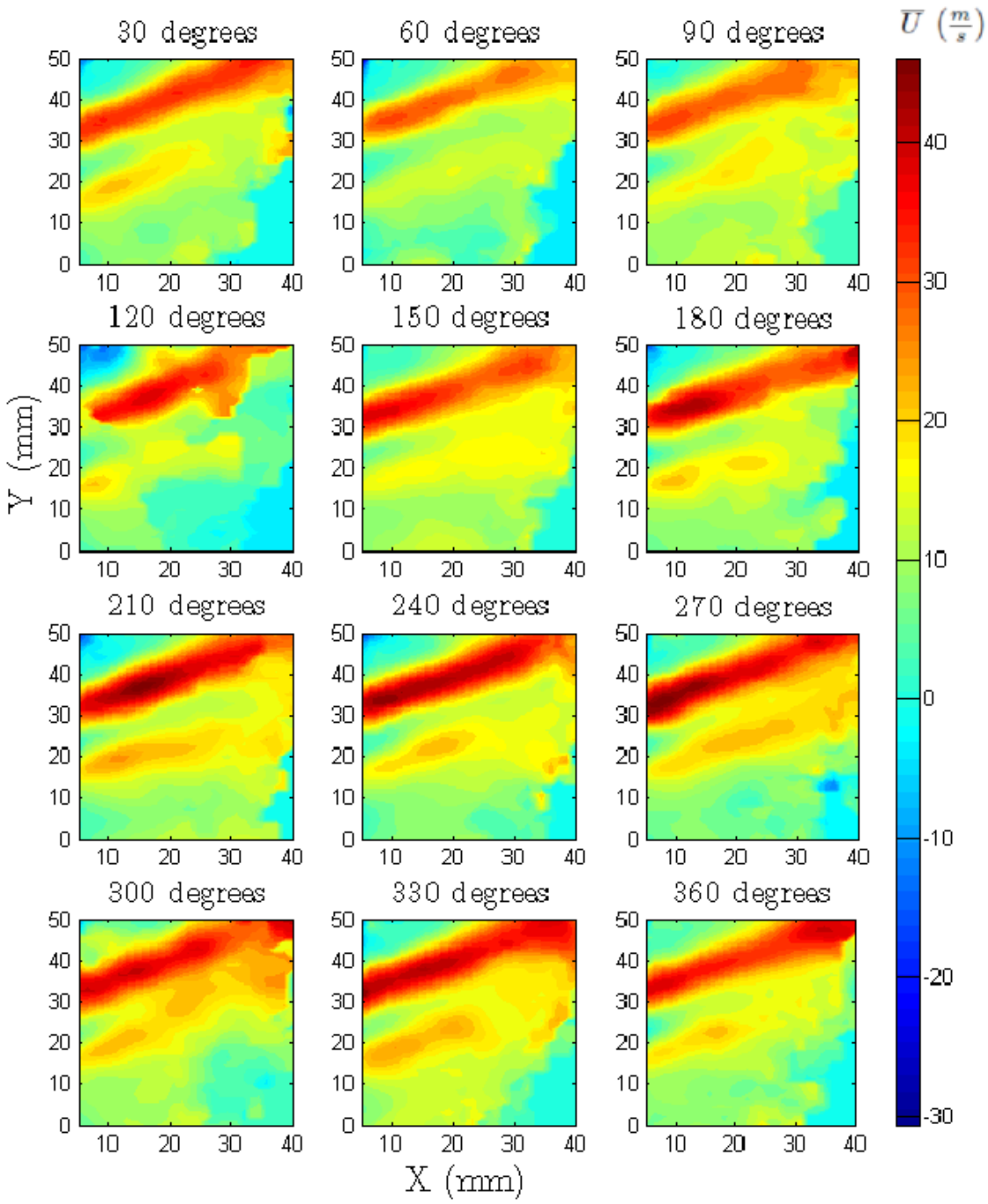

Figure 7.5: Phase averaged velocity fields with values of phase angle marked. Note the low velocity at a phase angle of 90 degrees and the high velocity at a phase angle of 270 degrees.

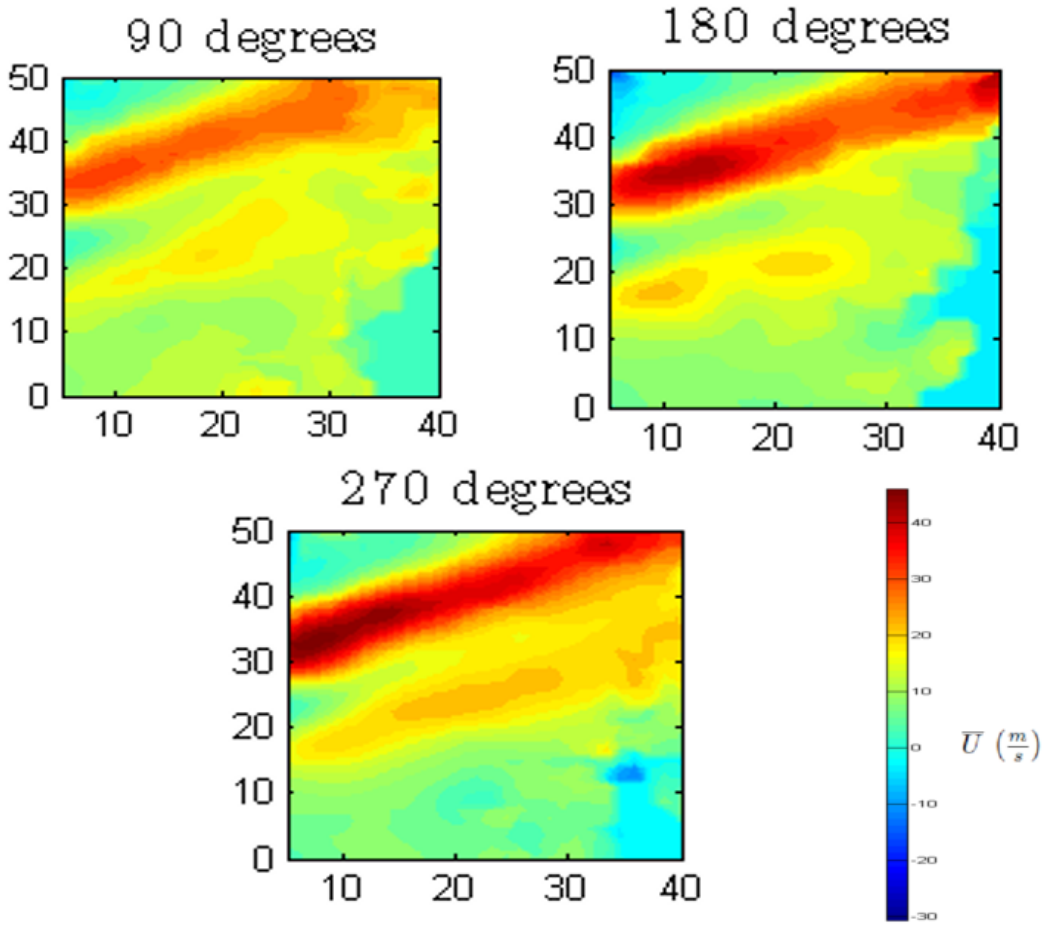

Figure 7.6: Detailed view of lower flow velocity at 90 degrees and higher flow velocity at 270 degrees relative to the mean flow shown here at 180 degrees.

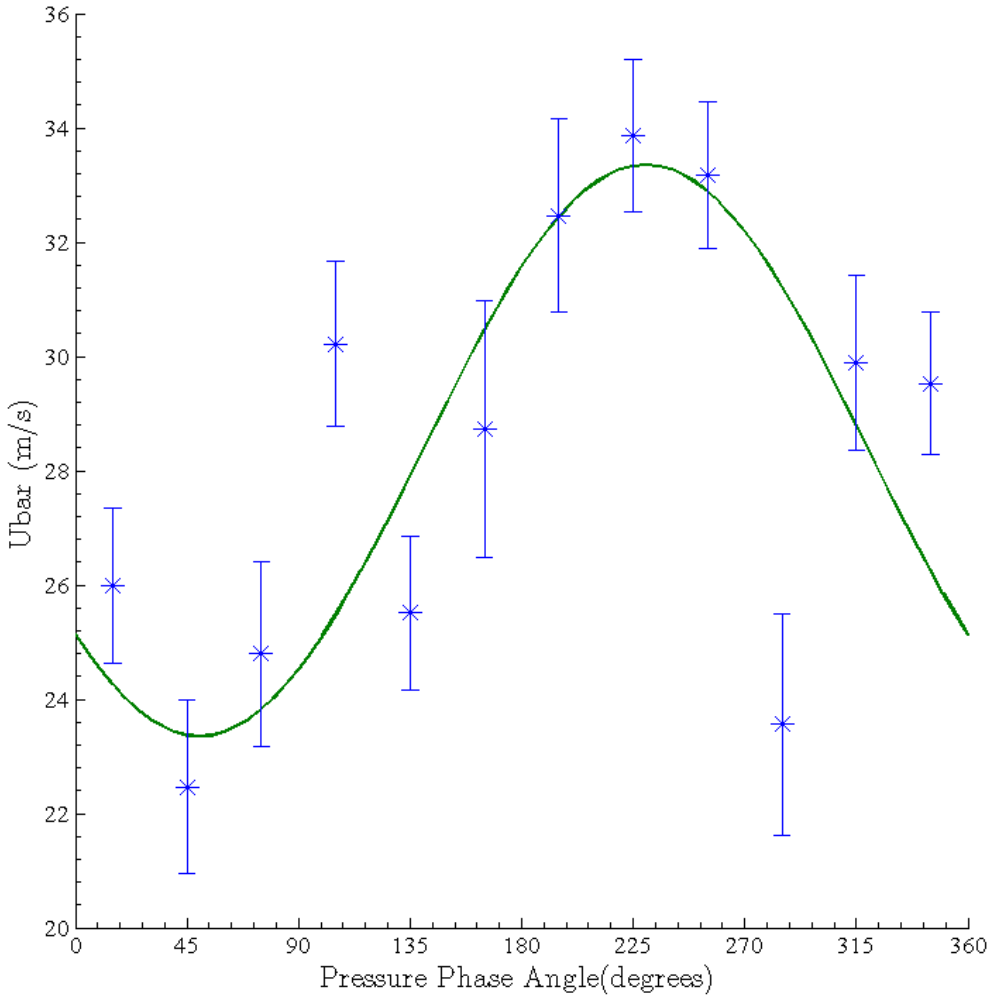

Figure 7.7: Phase averaged velocity at the base of the main jet (shown in Figure 7.4) as a function of the phase angle associated with the pressure oscillation. The velocity exhibits a sinusoidal behavior and appears to lag the pressure by about 140 degrees.

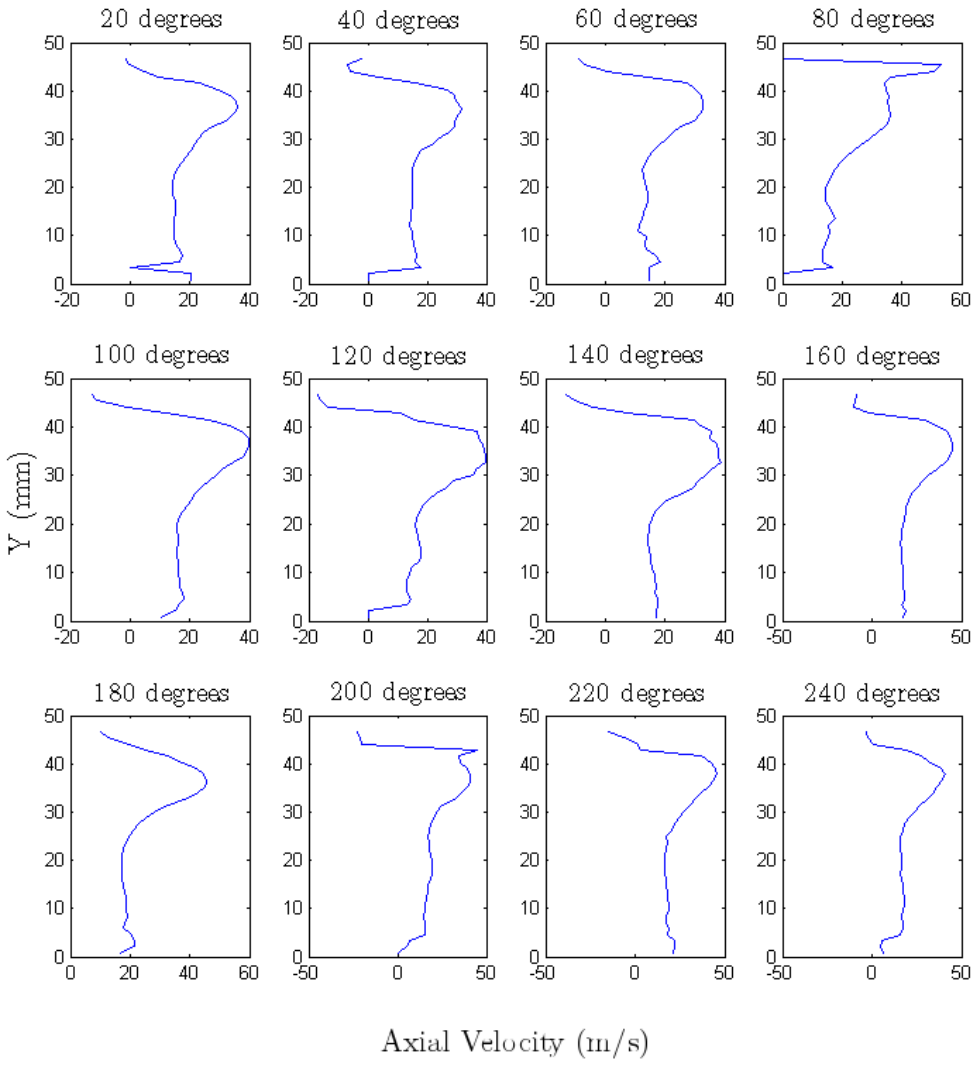

Figure 7.8: Phase averaged profiles of axial velocity at x=15mm downstream of the injector. Pressure phase angle is marked.

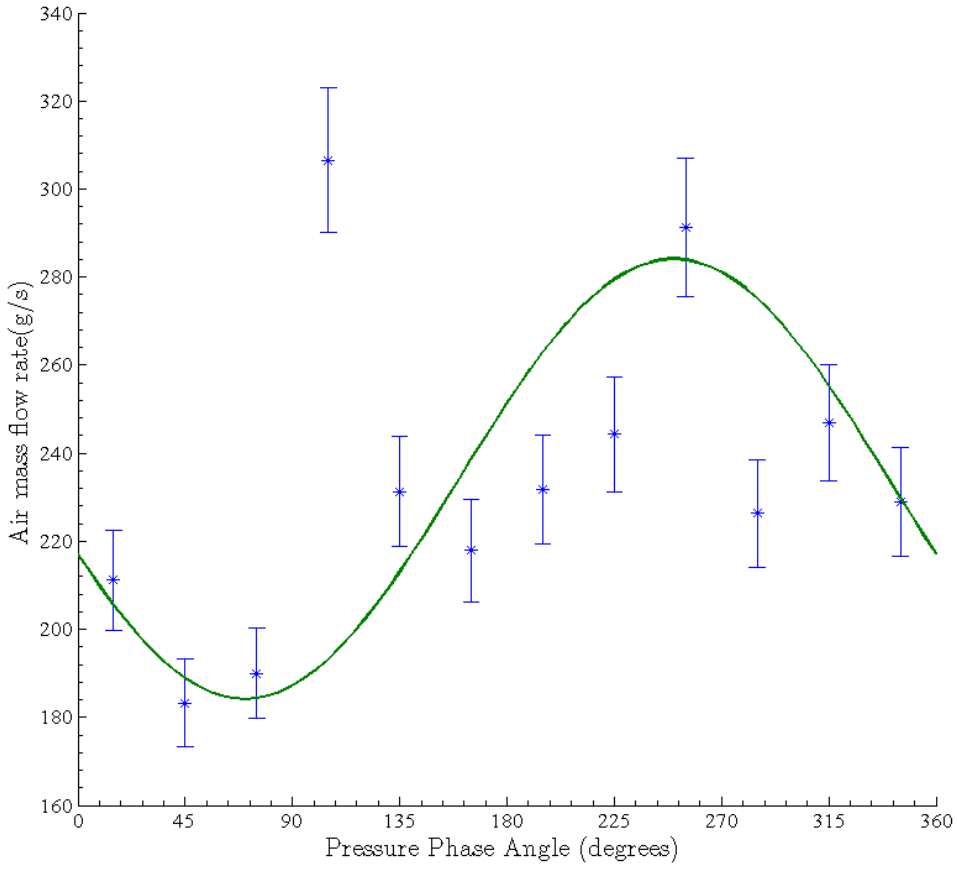

Figure 7.9: Phase averaged air mass flow rate at x=15 mm downstream of the injector. The air mass flow rate is cyclical and lags the pressure by 160 degrees

CHAPTER VIII

Conclusions

8.1 Summary

This study is one of the first to record simultaneous high speed video, phase averaged PIV, and pressure data of a combustion instability in a large, realistic gas turbine model combustor operated with liquid Jet-A fuel at elevated pressures and preheat temperatures. Only two other similar studies were reported [3] [33]. Of these large scale studies, this work is the first to systematically vary many of the governing parameters and physical dimensions (air mass flow rate, equivalence ratio, chamber dimensions) and record the pressure spectra. Also, This is the first study to apply phase-averaged PIV to determine if an equivalence ratio oscillation occurs due to a time varying air flow. Previous work in the UMGTC by Dhanuka [15] did not operate at "growl" conditions and did not investigate the 80 and 160 Hz instabilities studied in this work. The previous efforts also did not use phase-averaged PIV diagnostics.

The University of Michigan Gas Turbine Combustor was modified to accept a commercial fuel injector and provide even more optical access than in previous studies. Elevated pressures, preheat temperatures and liquid Jet-A fuel replicated realistic conditions at which low frequency instabilities are known to occur. Pressure traces identified the main frequencies of combustion instability present in the com-

bustor. Two dominant frequencies, 80 and 160 Hz, were identified. Simultaneous high speed chemiluminescence videography, phase-averaged particle image velocimetry and pressure traces characterized these low frequency oscillations of the flame and determined their effects on the flow field. Based on the current data, the inner and outer pilot air swirlers were found to be the most likely cause of the 80 and 160 Hz Helmholtz modes. The flame coupling with these acoustic modes was determined to be due to equivalence ratio oscillations due to fluctuations in the air mass flow rate, as confirmed by the phase averaged PIV data.

Based on the results in this study a basic description of this low frequency mechanism is shown in Figure 8.1. Arbitrarily beginning at the attached state, the flame experiences a distributed heat release resulting in lowered flame tube pressure. This results in an increase in air mass flow rate and velocity to the base of the flame. The flame then lifts off and compresses. The concentrated heat release results in an increase in flame tube pressure. The air mass flow rate and velocity relax and the flame re-attaches to the injector.

A separate instability phenomena also was investigated near the Lean Blowout Limit. This instability was studied in collaboration with Sulabh Dhanuka and was determined to be caused by the inability of the pilot to fully stabilize the main flame. The main flame then lifted off and flashed back into the corner of the combustor section. A mathematical model was developed to predict the frequency of this instability.

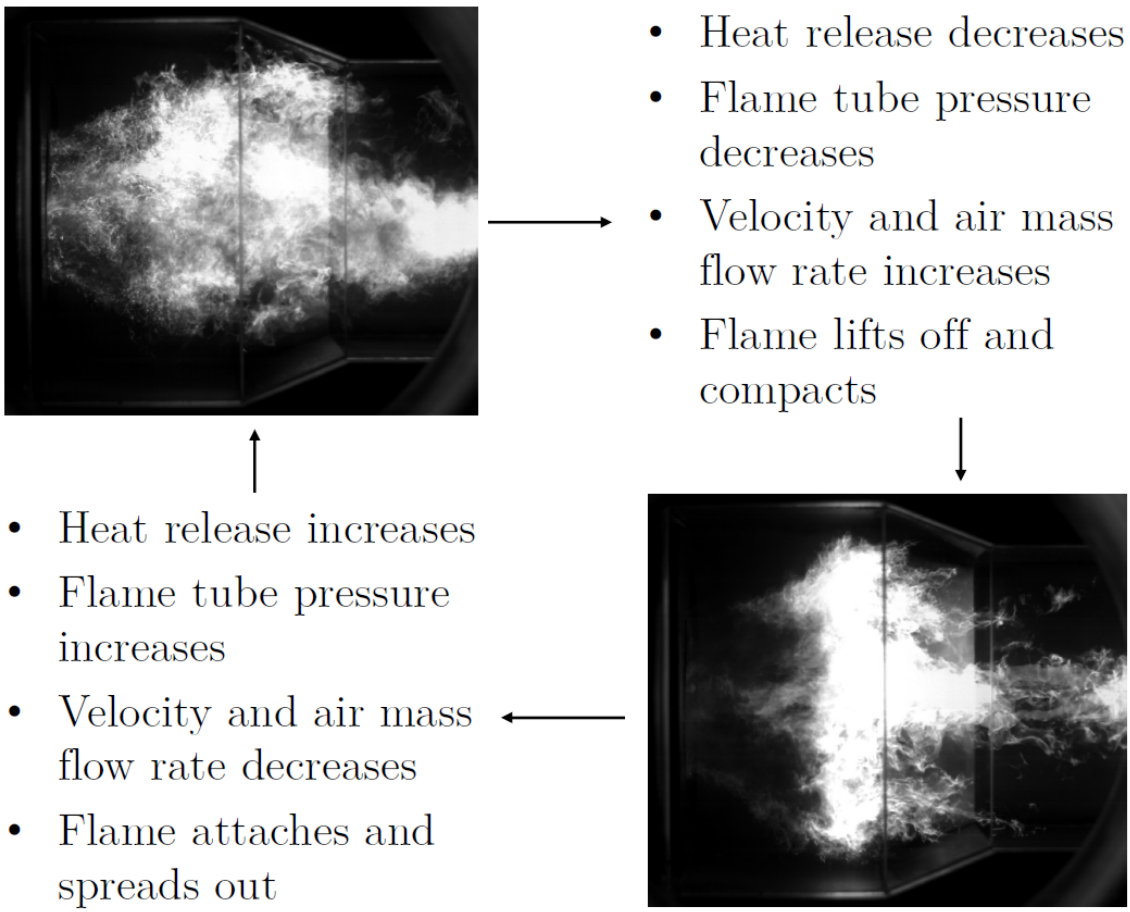

Figure 8.1: A simplified explanation of the cycle during the low frequency oscillations.

8.2 Incipient Blowout Conclusions

- Under fueling conditions near to lean blowout limits, very low frequency instabilities were observed at frequencies less than 20 Hz.
- These instabilities were very violent and consisted of cycles of flashback, extinction and re-ignition.
- A model was developed to predict the frequency of the instability. The main components of the model are two time lags. The first is associated with the time to fill the corner recirculation zone with fuel and the second with the time it takes to the flame flashback through this mixture.

8.3 Pressure Field Conclusions

- Combustion instabilities were found to occur at 80, 160, 460, 650, and 1300 Hz. They can be separated into two groups based on their magnitude. The higher frequency group (460, 650, and 1300 Hz) had a small magnitude (-40 dB). The low frequency group (80, 160 Hz) were much stronger (-20 dB).
- The low frequency instabilities do not depend on modes of fuel injection. There was no frequency change when the amount of main or pilot fuel was altered. Therefore it seems the conventional industry practice of instability control by secondary fuel addition would be ineffective in correcting this oscillation.
- The magnitude of the oscillation scaled linearly with the equivalence ratio. The instability can be reduced to non-combusting levels by maintaining a global equivalence ratio of less than 0.225.
- The combustor exhibited evidence of a bulk mode oscillation rather than a standing wave in the plenum.

- Physical changes to the dimensions of the outer pressure vessel produced no change in the frequency of the 80 and 160 Hz oscillations. However changing the dimensions of the fuel injector did change the frequency. The only dimension of the fuel injector that was physically possible to change was the area of the outer air swirler. This did cause a large change in the frequencies of the low frequency oscillations.

- It is concluded that the strong 80 and 160 Hz combustion instability modes are due to a Helmholtz-like bulk acoustic resonance that is associated with the dimensions of the fuel injector and the flame tube and not the outer pressure vessel.

8.4 Video Conclusions

- High speed video shows that the flame undergoes a large scale cyclical motion. Previous theory predicted that flames remain attached and only their length oscillated. Videos dispute that prediction and show that the flame base periodically lifts off and flashes back.

- This flame motion exhibits the same 80 and 160 Hz frequencies found in the pressure traces.

- A variety of flame features show low frequency oscillations including the lift off height of the flame, the flame width at the exit of the flame tube, and the overall intensity and thus heat release.

- The flame lift off height is 180 degrees out of phase with the pressure oscillation and the chemiluminescence lags behind pressure but leads the lift off height.

- The downstream motion of the flame occurs slower than the return upstream

motion indicating air flow speeds and flame speeds play a role in this mechanism.

- The centroid of heat release exhibits a cyclical motion in the combustor at 80 and 160 Hz.
- The Rayleigh Index shows a region of forcing near the injector face where the flame motion occurs and a dampening region in the neck of the flame tube.
- These measured oscillations in flame dimensions provide good metrics for assisting future LES simulations of this type of combustion instability.

8.5 Acoustic Analysis Conclusions

- A model for a Helmholtz resonator with two necks was simplified and applied to this experiment.
- Of the many possible dimensions associated with this experiment, only one set of dimensions yielded a Helmholtz frequency of 80 Hz and only one other set of dimensions yielded a Helmholtz frequency of 160 Hz, which were the two dominant frequencies measured. These dimensions were found to be associated with the inner and outer pilot air swirlers. Therefore, these are most likely the source of the observed instability mode.

8.6 PIV Conclusions

- A phase-averaged PIV diagnostic method was developed specifically to determine how the velocity varies with the phase angle of the pressure field.
- The pressure phase averaged results show a cyclical variation in flow speed in the main and pilot air jet. Velocity oscillations were +/- 5.5 m/s where the mean velocity is 28 m/s.

- This local velocity oscillation lags the pressure oscillation by 140 degrees.
- Air mass flow rates also show an oscillating behavior of +/- 50 g/s and lag the pressure by 150 degrees.
- It is concluded that the PIV and Rayleigh Index data provide strong evidence that the amplification of the natural Helmholtz resonance is most likely due to a mechanism that is commonly known as an "equivalence ratio oscillation". A bulk mode oscillation of the air provided to the flame occurs which causes the periodic liftoff and flashback of the flame that is observed in the high speed movies.
- Time averaged flow fields have similar features to previous results in a similar TAPS burner (Dhanuka et al. [13]).

8.7 Recommendations for Future Work

This study provides useful information on how a realistic scale combustor will preferentially select specific frequencies of combustion oscillation and how results from smaller scale experiments can scale to larger systems. The current setup is not however suited to fundamental studies of acoustic phenomena. The current data set can provide some guidance to LES model development, but in order to serve as model validation further measurements would be necessary. Inlet and outlet boundary conditions, swirl number, and at least an estimate of chemical composition would be the minimum amount of data that would need to be added to the current data in order to create a model validation set.

The current setup would be very useful for a study on NO_X production and the potential reduction promised by LPP technology. High speed PIV and laser based thermometry would give information on the temperature field and residence times,

two key parameters in NO_X production. Candidates for the laser thermometry include OH and indium two-line PLIF. CARS is unlikely to work well in this system due to the double window panes and high amount of soot and poly-aromatic hydrocarbon (PAH) interference.

APPENDICES

APPENDIX A

Two Cycles of a 80 Hz Combustion Instability from High Speed Video

Figure A.1: Single frame from 1000 Hz high speed video of flame chemiluminescence at t= 47 ms. Run conditions listed in Table 4.4

Figure A.2: Single frame from 1000 Hz high speed video of flame chemiluminescence at t= 48 ms.

Figure A.3: Single frame from 1000 Hz high speed video of flame chemiluminescence at t= 49 ms.

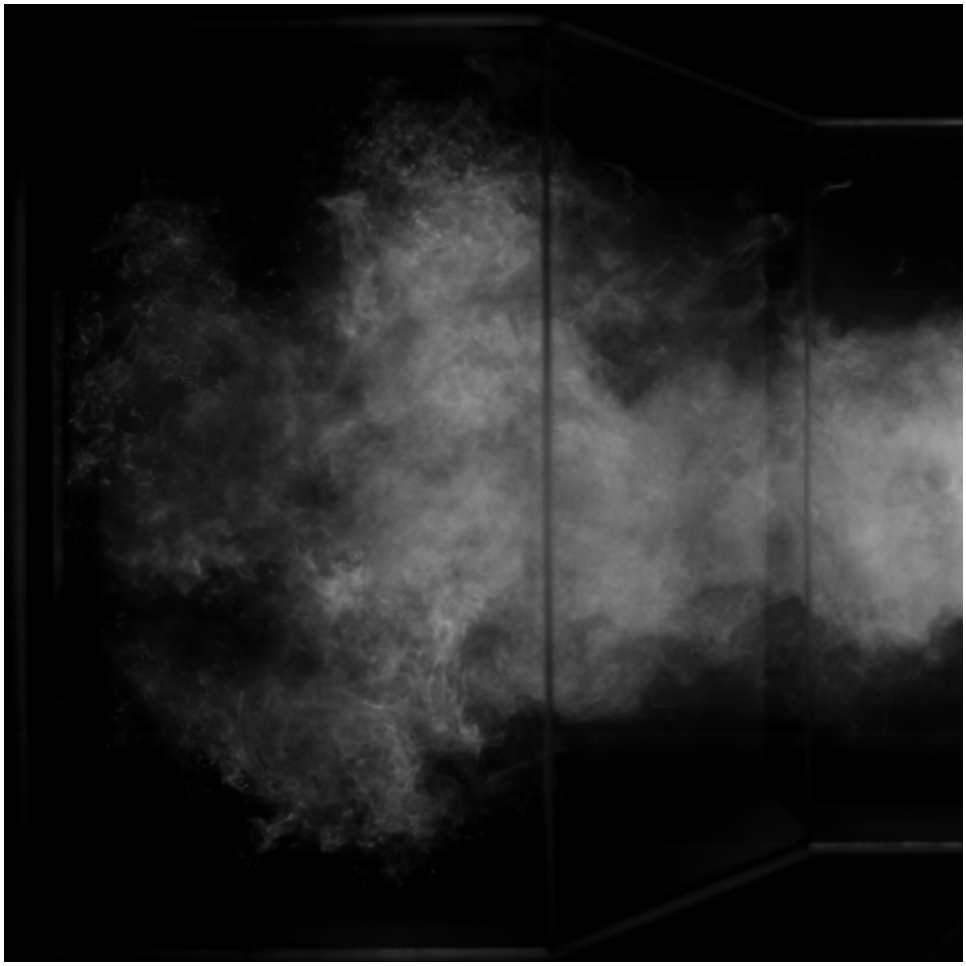

Figure A.4: Single frame from 1000 Hz high speed video of flame chemiluminescence at t= 50 ms.

Figure A.5: Single frame from 1000 Hz high speed video of flame chemiluminescence at t= 51 ms.

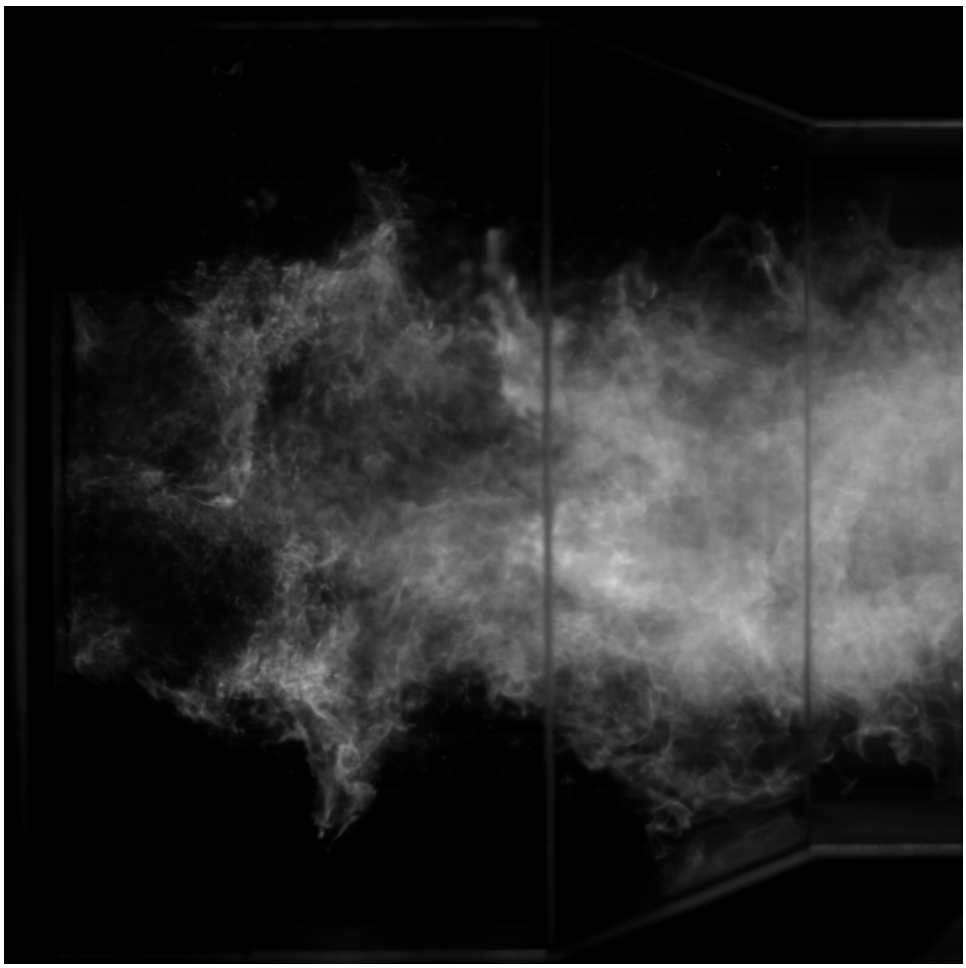

Figure A.6: Single frame from 1000 Hz high speed video of flame chemiluminescence at t= 52 ms.

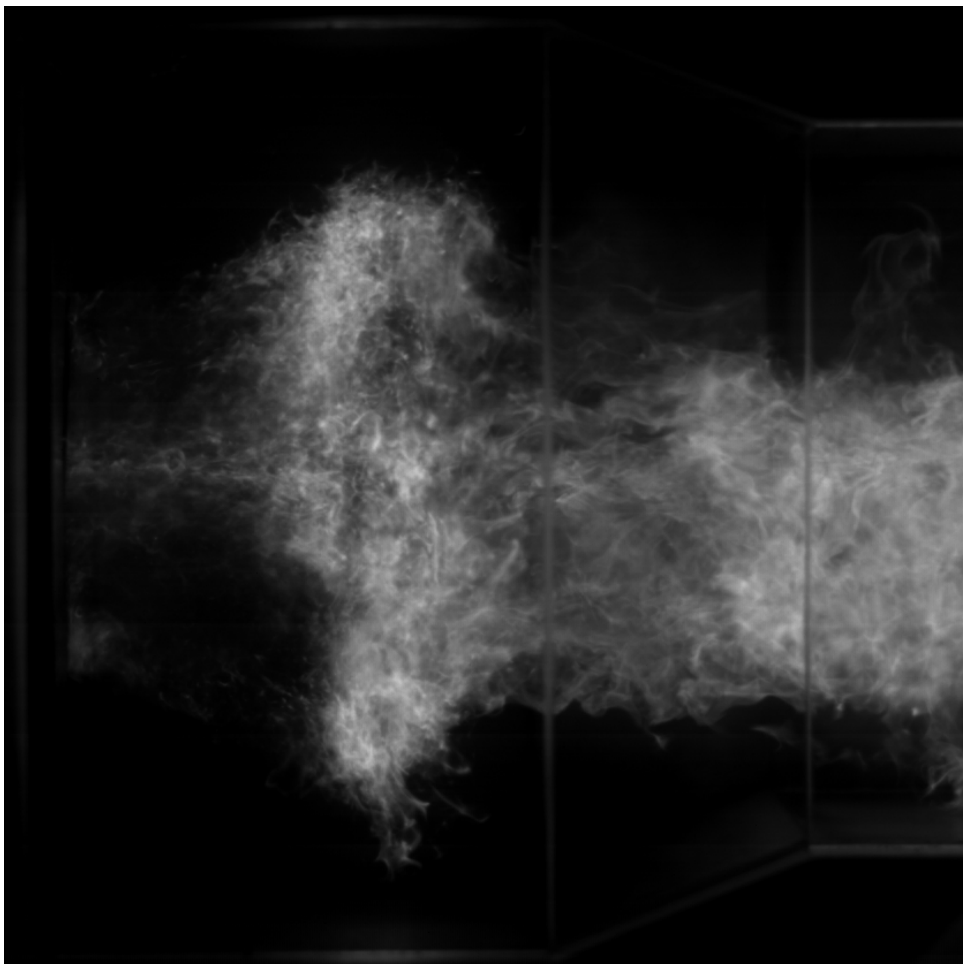

Figure A.7: Single frame from 1000 Hz high speed video of flame chemiluminescence at t= 53 ms.

Figure A.8: Single frame from 1000 Hz high speed video of flame chemiluminescence at t= 54 ms.

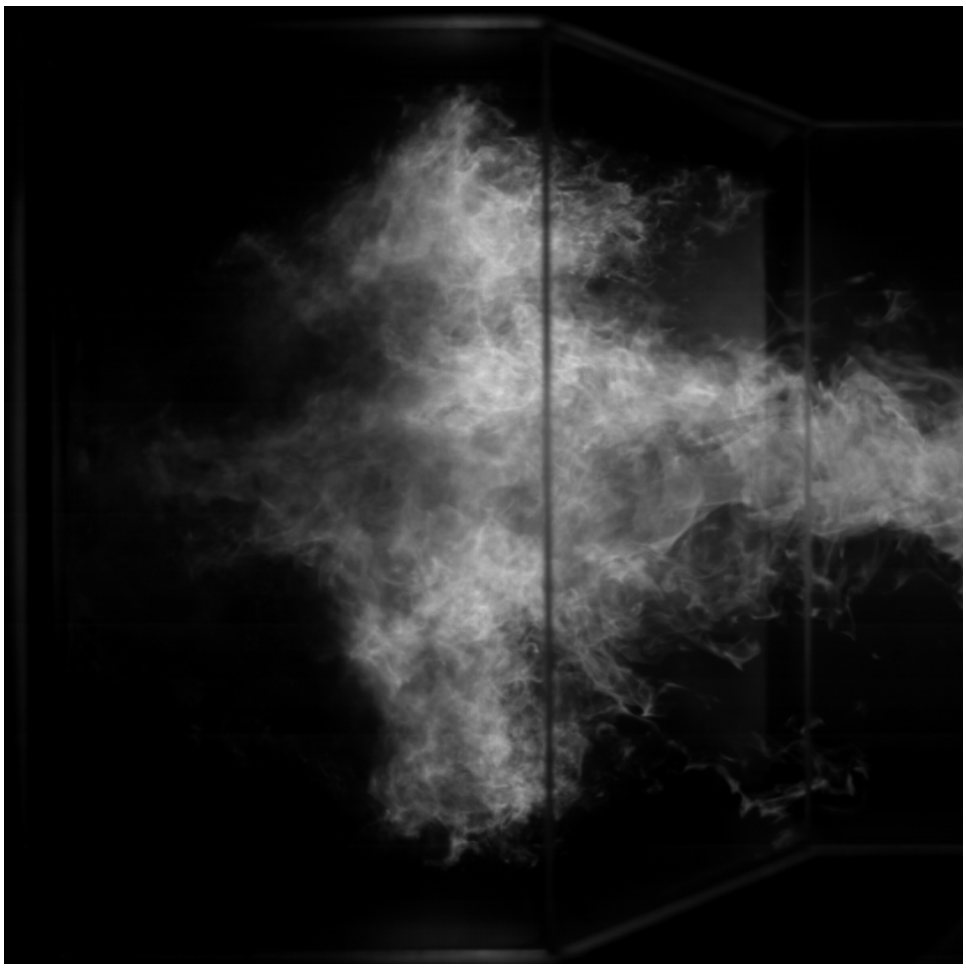

Figure A.9: Single frame from 1000 Hz high speed video of flame chemiluminescence at t= 55 ms.

Figure A.10: Single frame from 1000 Hz high speed video of flame chemiluminescence at t= 56 ms.

Figure A.11: Single frame from 1000 Hz high speed video of flame chemiluminescence at t= 57 ms.

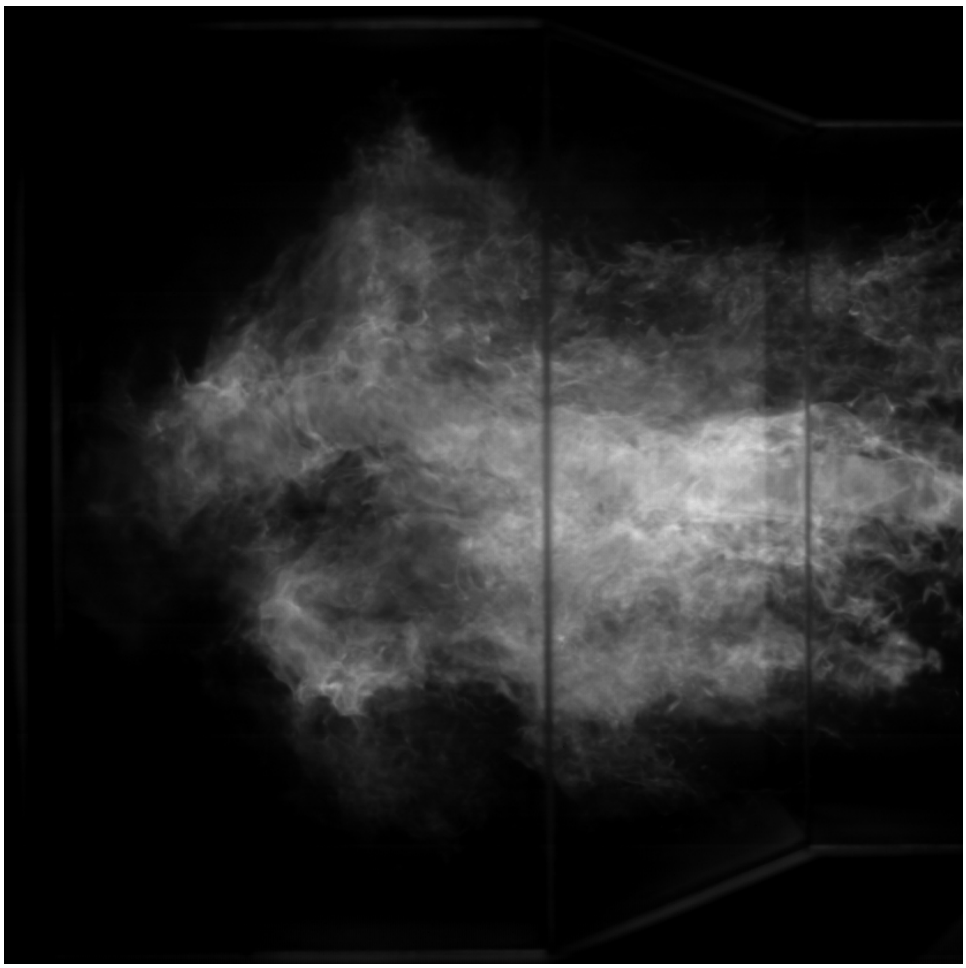

Figure A.12: Single frame from 1000 Hz high speed video of flame chemiluminescence at t= 58 ms.

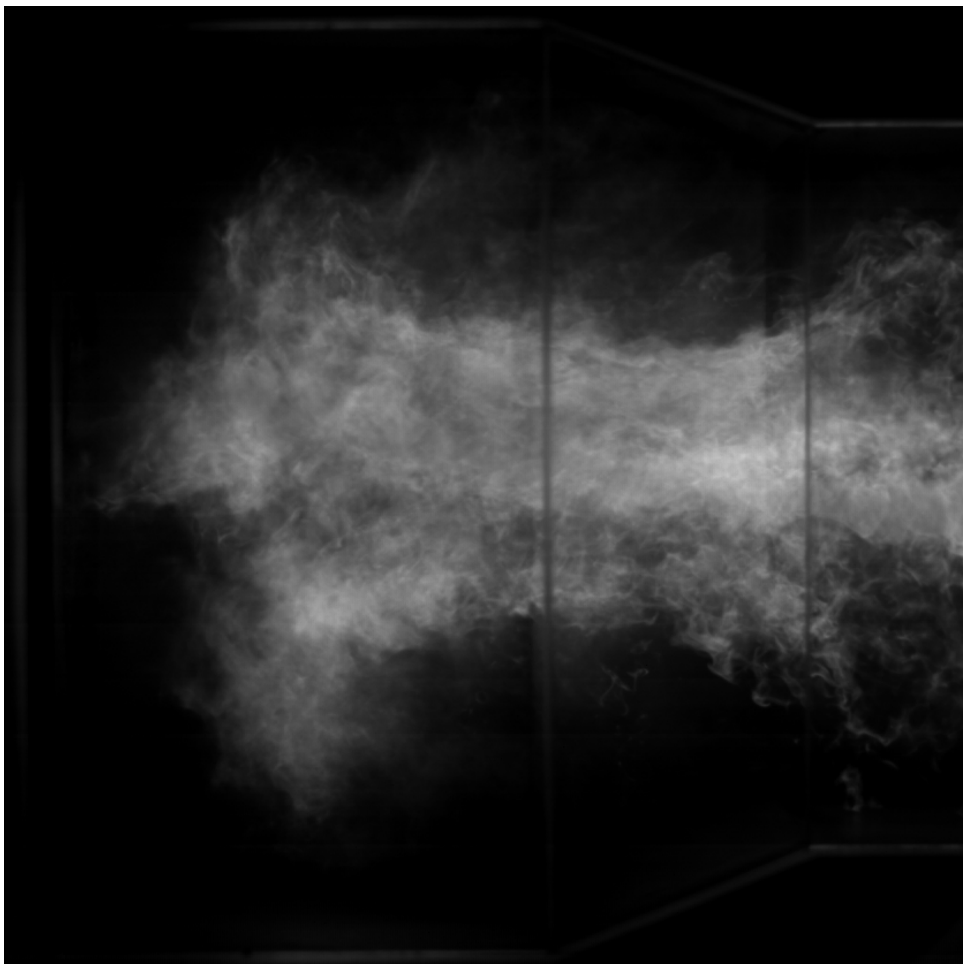

Figure A.13: Single frame from 1000 Hz high speed video of flame chemiluminescence at t= 59 ms.

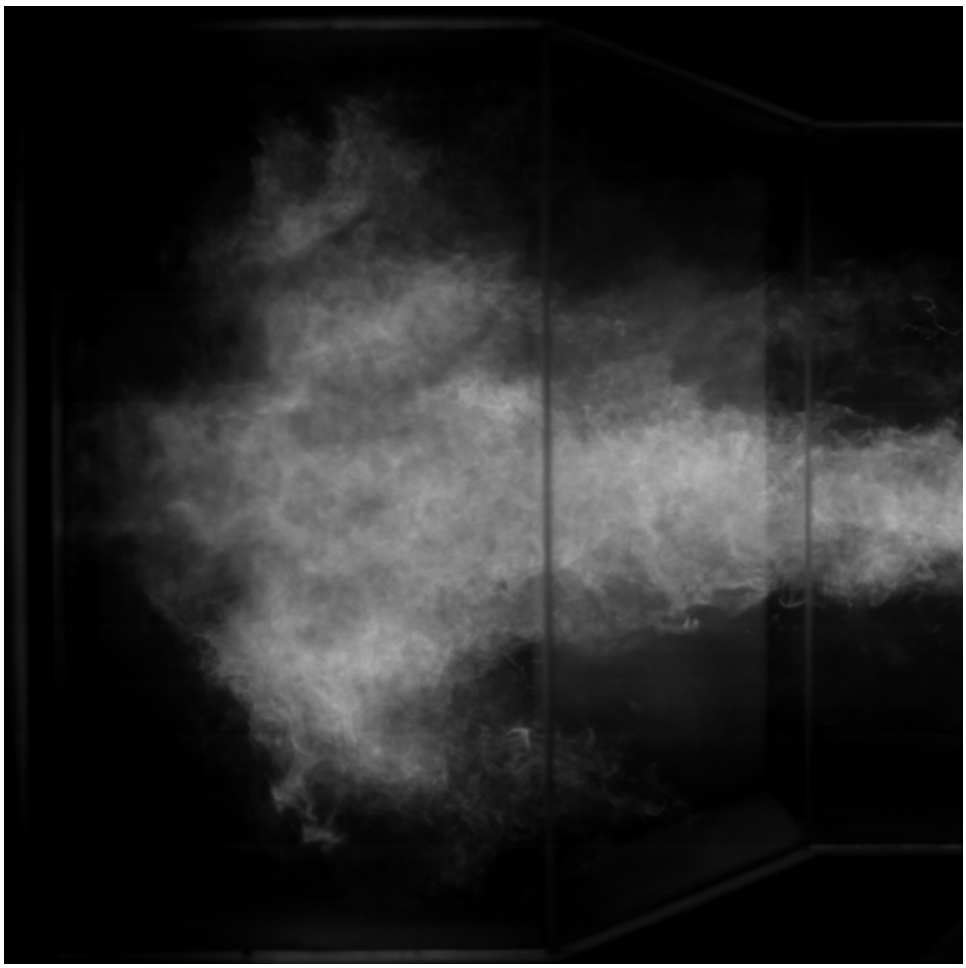

Figure A.14: Single frame from 1000 Hz high speed video of flame chemiluminescence at t= 60 ms.

Figure A.15: Single frame from 1000 Hz high speed video of flame chemiluminescence at t= 61 ms.

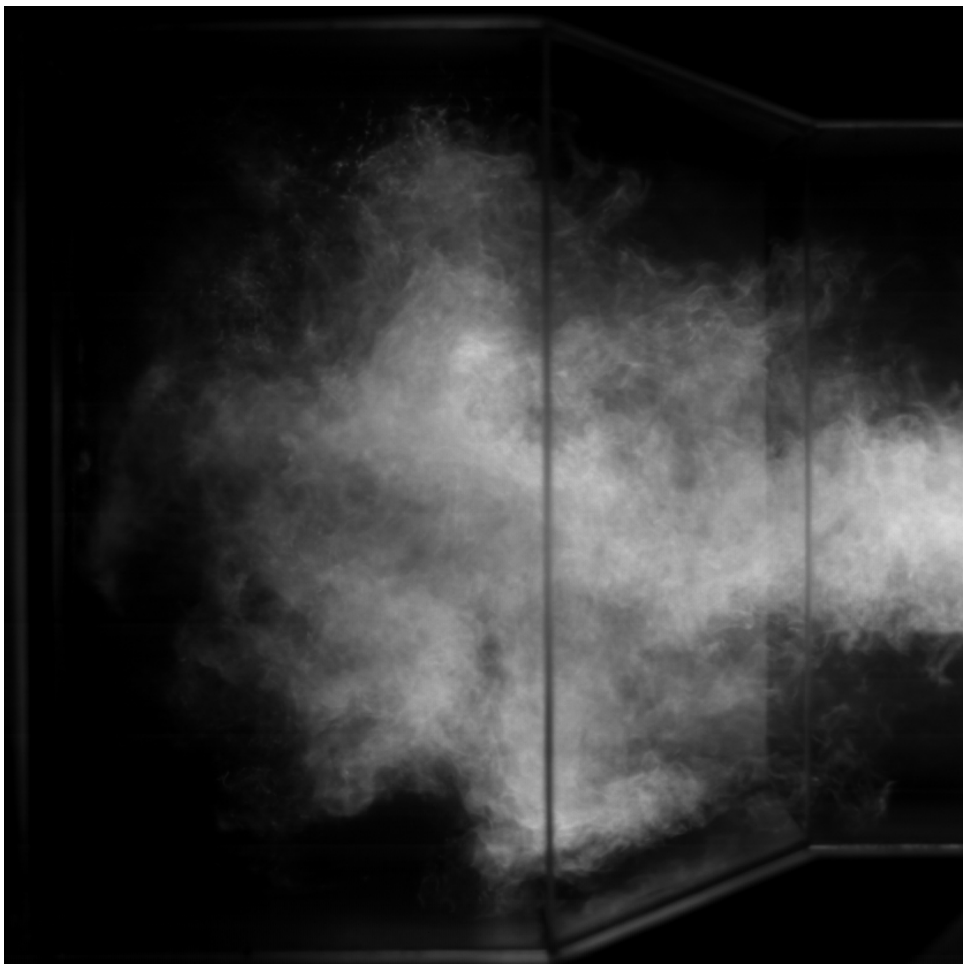

Figure A.16: Single frame from 1000 Hz high speed video of flame chemiluminescence at t= 62 ms.

Figure A.17: Single frame from 1000 Hz high speed video of flame chemiluminescence at t= 63 ms.

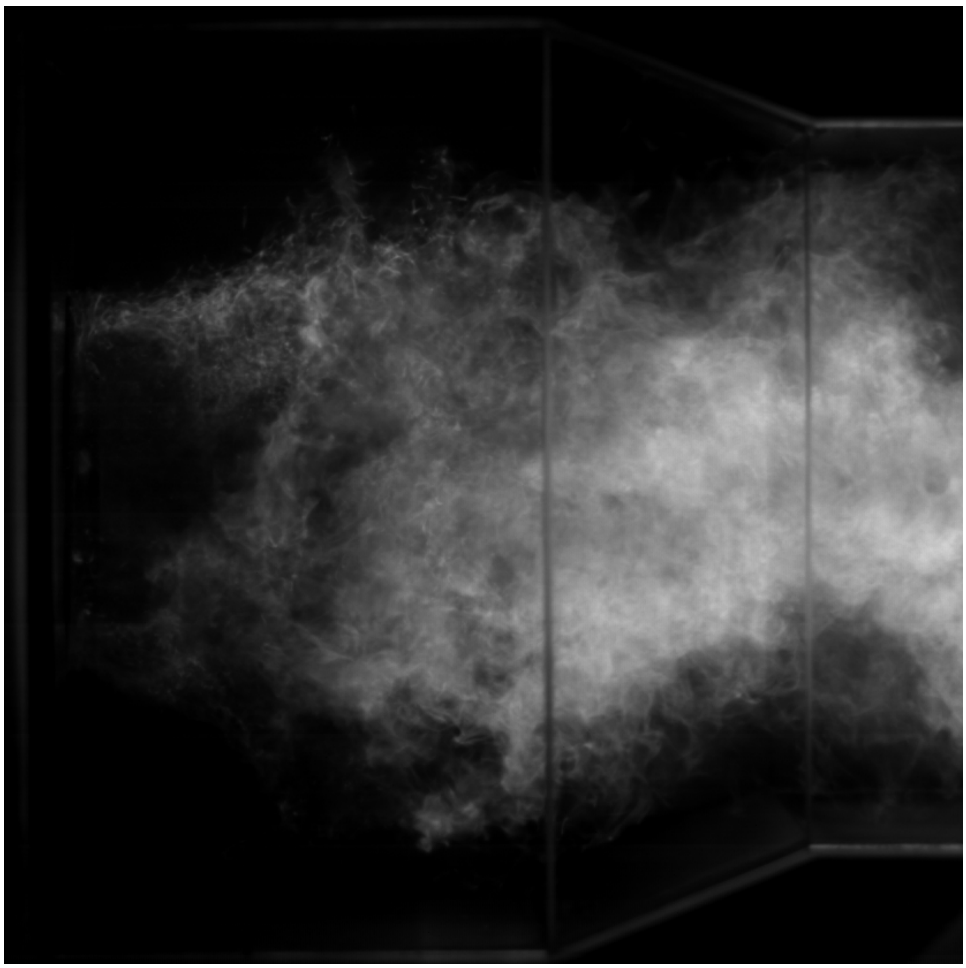

Figure A.18: Single frame from 1000 Hz high speed video of flame chemiluminescence at t= 64 ms.

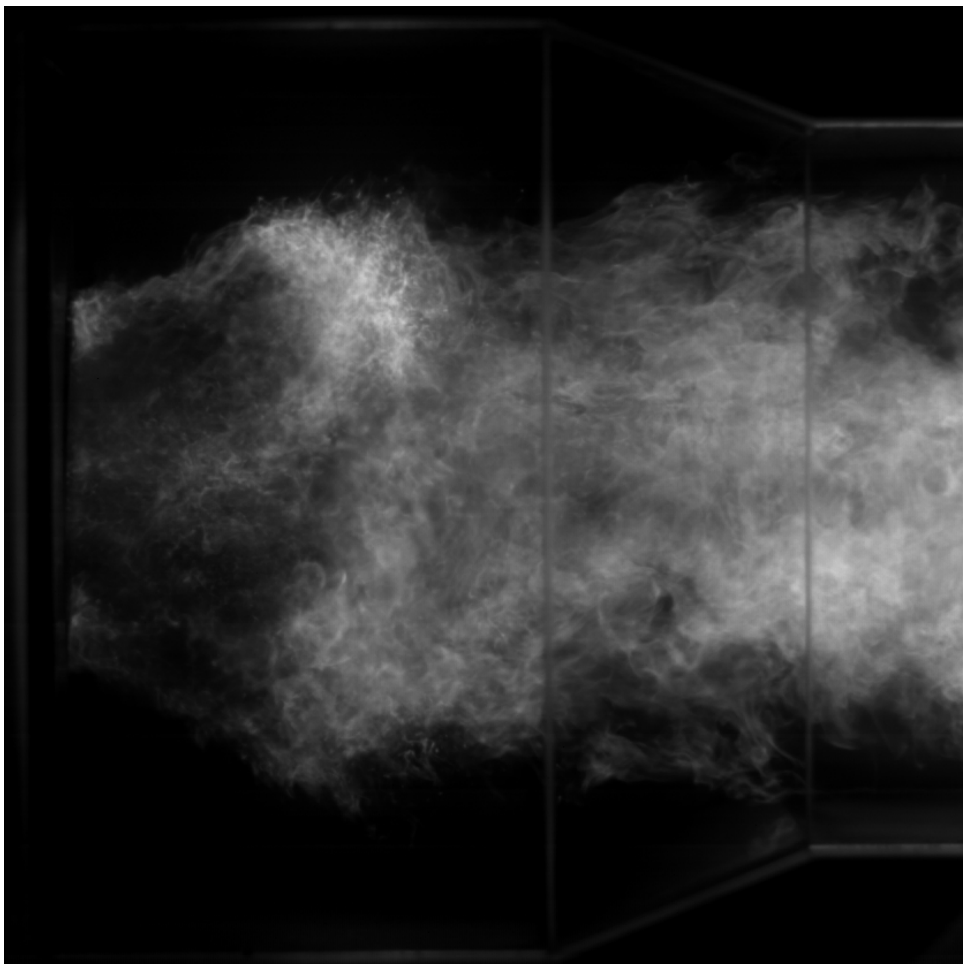

Figure A.19: Single frame from 1000 Hz high speed video of flame chemiluminescence at t= 65 ms.

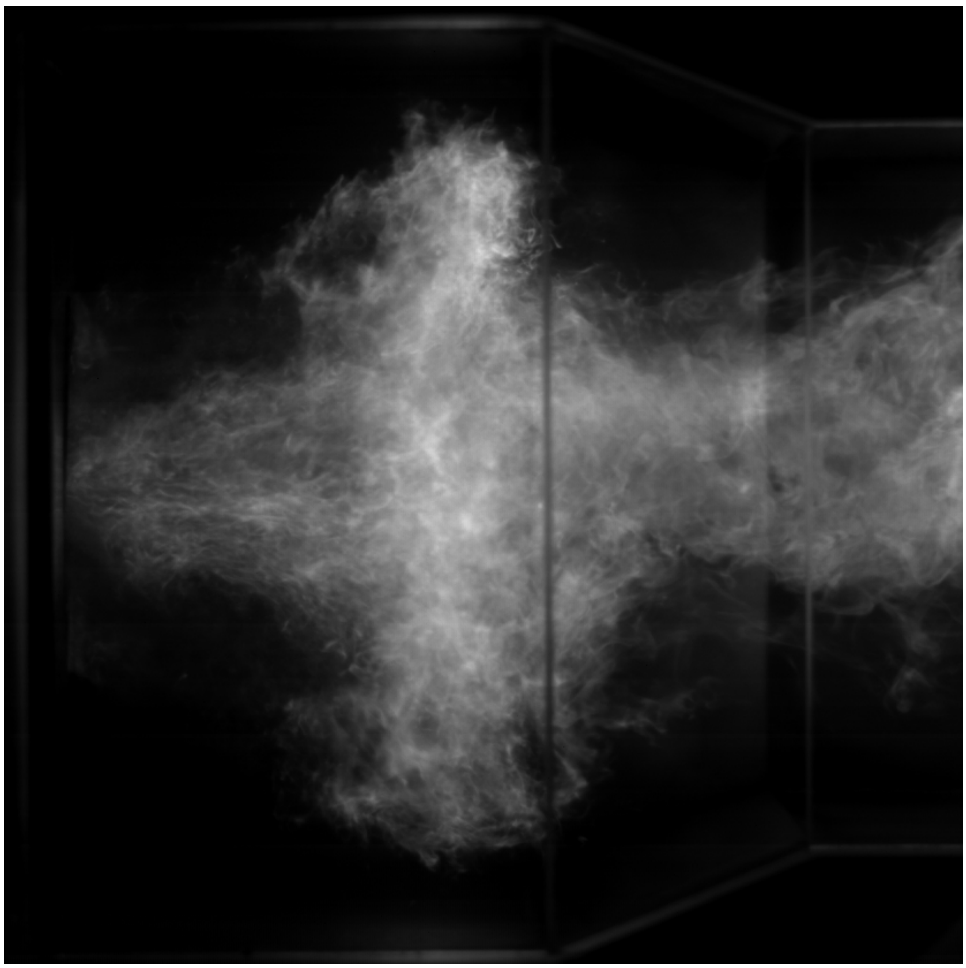

Figure A.20: Single frame from 1000 Hz high speed video of flame chemiluminescence at t= 66 ms.

Figure A.21: Single frame from 1000 Hz high speed video of flame chemiluminescence at t= 67 ms.

Figure A.22: Single frame from 1000 Hz high speed video of flame chemiluminescence at t= 68 ms.

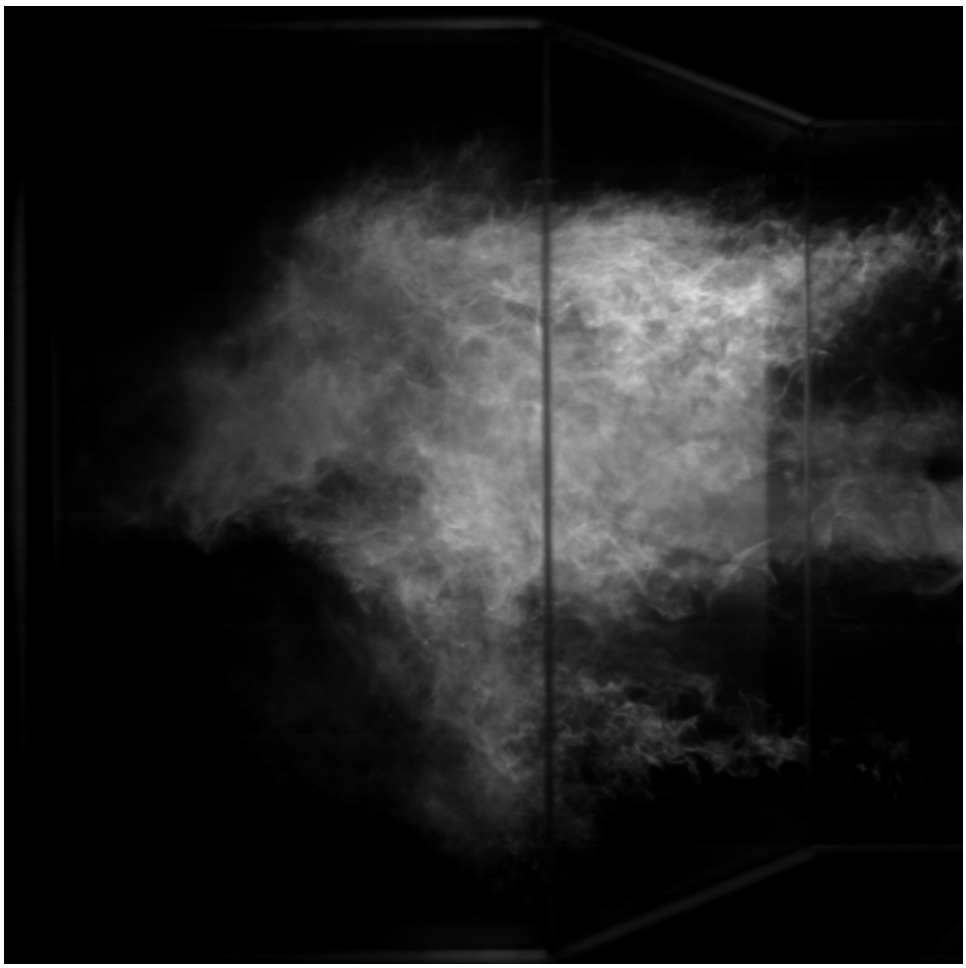

Figure A.23: Single frame from 1000 Hz high speed video of flame chemiluminescence at t= 69 ms.

Figure A.24: Single frame from 1000 Hz high speed video of flame chemiluminescence at t= 70 ms.

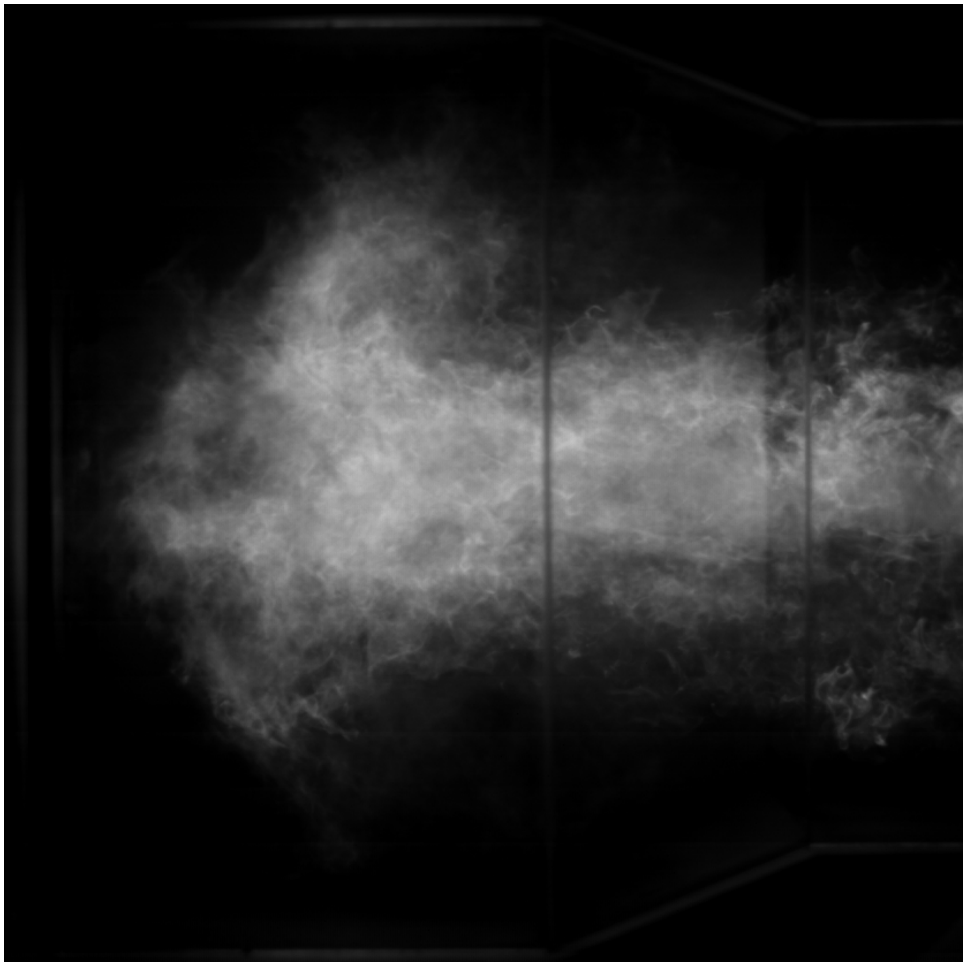

Figure A.25: Single frame from 1000 Hz high speed video of flame chemiluminescence at t= 71 ms.

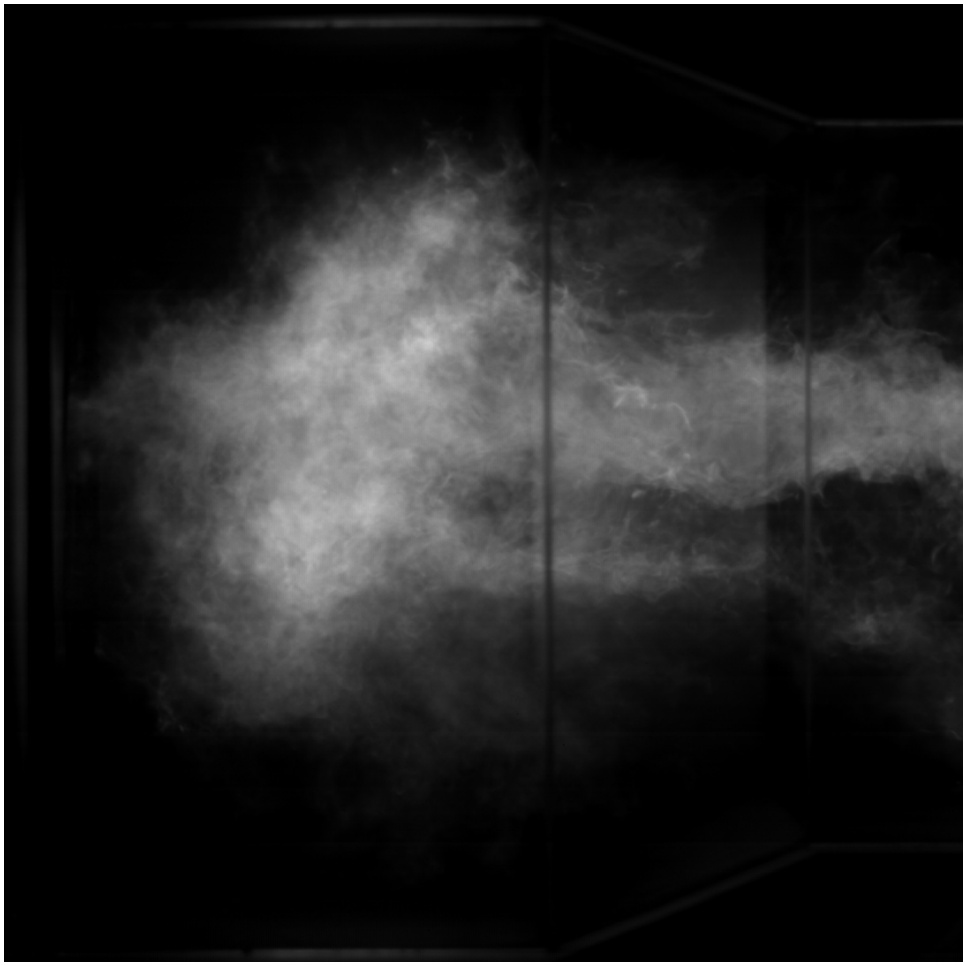

Figure A.26: Single frame from 1000 Hz high speed video of flame chemiluminescence at t= 72 ms.

BIBLIOGRAPHY

BIBLIOGRAPHY

[1] P. Allison, J. F. Driscoll, and M. Ihme. Acoustic behavior of a partially-premixed gas turbine model combustor. In *AIAA paper 2012-0504*. 50th AIAA Aerospace Sciences Meeting including the New Horizons Forum and Aerospace Exposition 09, 2012.

[2] M. Barrère. Analysis of rocket-engine transient regimes. *Acta Astronautica*, 4(5-6):641 – 670, 1977.

[3] D. Bernier, S. Candel, and F. Lacas. Instability mechanisms in a premixed prevaporized combustor. *Journal of Propulsion and Power*, 20(4):648–656, July 2004.

[4] F. Boudy, D. Durox, T. Schuller, and S. Candel. Nonlinear mode triggering in a multiple flame combustor. *Proceedings of the Combustion Institute*, 33(1):1121 – 1128, 2011.

[5] I. Boxx, M. Stöhr, C. Carter, and W. Meier. Temporally resolved planar measurements of transient phenomena in a partially pre-mixed swirl flame in a gas turbine model combustor. *Combustion and Flame*, 157(8):1510 – 1525, 2010.

[6] S.M. Candel. Combustion instabilities coupled by pressure waves and their active control. *Symposium (International) on Combustion*, 24(1):1277 – 1296, 1992.

[7] D. S. Chamberlin and A. Rose. The flicker of luminous flames. *Industrial & Engineering Chemistry*, 20(10):1013–1016, 1928.

[8] J.H. Cho and T. Lieuwen. Laminar premixed flame response to equivalence ratio oscillations. *Combustion and Flame*, 140(1-2):116 – 129, 2005.

[9] N.T. Clemens and M.G. Mungal. A planar Mie scattering technique for visualizing supersonic mixing flows. *Experiments in Fluids*, 11:175–185, 1991.

[10] J. M. Cohen and A. Banaszuk. Factors affecting the control of unstable combustors. *Journal of Propulsion and Power*, 19(5):811 – 821, 2003.

[11] M. de la Cruz García, E. Mastorakos, and A.P. Dowling. Investigations on the self-excited oscillations in a kerosene spray flame. *Combustion and Flame*, 156(2):374 – 384, 2009.

[12] S. K. Dhanuka, J. E. Temme, and J. F. Driscoll. Lean-limit combustion instabilities of a lean premixed prevaporized gas turbine combustor. *Proceedings of the Combustion Institute*, 33(2):2961 – 2966, 2011.

[13] S. K. Dhanuka, J. E. Temme, and J. F. Driscoll. Unsteady aspects of lean premixed prevaporized gas turbine combustors: Flame-flame interactions. *Journal of Propulsion and Power*, 27(3):631 – 641, 2011.

[14] S. K. Dhanuka, J. E. Temme, J. F. Driscoll, and H. C. Mongia. Vortex-shedding and mixing layer effects on periodic flashback in a lean premixed prevaporized gas turbine combustor. *Proceedings of the Combustion Institute*, 32(2):2901 – 2908, 2009.

[15] S.K. Dhanuka. *An Experimental Study of the Stable and Unstable Operation of an LPP Gas Turbine Combustor*. PhD thesis, University of Michigan, 2008.

[16] A. P. Dowling and S Hubbard. Instability in lean premixed combustors. *Proceedings of the Institution of Mechanical Engineers, Part A: Journal of Power and Energy*, 214(4):317–332, 2000.

[17] A. P. Dowling and S. R. Stow. Acoustic analysis of gas turbine combustors. *Journal of Propulsion and Power*, 19(5):751–764, 2003.

[18] D. Durox, T. Schuller, and S. Gandel. Self-induced instability of a premixed jet flame impinging on a plate. *Proceedings of the Combustion Institute*, 29(1):69 – 75, 2002.

[19] D. Durox, T. Schuller, N. Noiray, A.L. Birbaud, and S. Candel. Rayleigh criterion and acoustic energy balance in unconfined self-sustained oscillating flames. *Combustion and Flame*, 156(1):106 – 119, 2009.

[20] J. Eckstein, E. Freitag, C. Hirsch, and T. Sattelmayer. Experimental study on the role of entropy waves in low-frequency oscillations in a rql combustor. *Journal of Engineering for Gas Turbines and Power*, 128(2):264, 2006.

[21] C. Fureby, F.F. Grinstein, G. Li, and E.J. Gutmark. An experimental and computational study of a multi-swirl gas turbine combustor. *Proceedings of the Combustion Institute*, 31(2):3107 – 3114, 2007.

[22] Y. Huang and V. Yang. Bifurcation of flame structure in a lean-premixed swirl-stabilized combustor: transition from stable to unstable flame. *Combustion and Flame*, 136(3):383 – 389, 2004.

[23] Y. Ikeda, J. Kojima, and H. Hashimoto. Local chemiluminescence spectra measurements in a high-pressure laminar methane/air premixed flame. *Proceedings of the Combustion Institute*, 29:1495–1501, 2002.

[24] K.U. Ingard. *On the Theory and Design of Acoustic Resonators*. 1953.

[25] S. Kato, T. Fujimori, A.P. Dowling, and H. Kobayashi. Effect of heat release distribution on combustion oscillation. *Proceedings of the Combustion Institute*, 30(2):1799 – 1806, 2005.

[26] K.T. Kim, J.G. Lee, B.D. Quay, and D.A. Santavicca. Response of partially premixed flames to acoustic velocity and equivalence ratio perturbations. *Combustion and Flame*, 157(9):1731 – 1744, 2010.

[27] K.T. Kim, J.G. Lee, B.D. Quay, and D.A. Santavicca. Spatially distributed flame transfer functions for predicting combustion dynamics in lean premixed gas turbine combustors. *Combustion and Flame*, 157(9):1718 – 1730, 2010.

[28] K.K. Kuo. *Principles of combustion*. John Wiley, 2005.

[29] D. S. Lee and T. J. Anderson. Measurements of fuel/air-acoustic coupling in lean premixed combustion systems. In *37th AIAA Aerospace Sciences Meeting and Exhibit*, 1999.

[30] J. G. Lee and D. A. Santavicca. Experimental diagnostics for the study of combustion instabilities in lean premixed combustors. *Journal of Propulsion and Power*, 19(5):735–750, September 2003.

[31] J.G. Lee, K. Kim, and D.A. Santavicca. Measurement of equivalence ratio fluctuation and its effect in heat release during unstable combustion. *Proceedings of the Combustion Institute*, 28:415–421, 2000.

[32] A.H. Lefebvre. *Gas Turbine Combustion*. Taylor and Francis, 1999.

[33] G. Li and E. J. Gutmark. Manifestations of combustion instability in a multi-swirl stabilized gas turbine combustor. pages 4385 – 4398, Reno, NV, United states, 2005.

[34] T. Lieuwen and K. McManus. Combustion dynamics in lean-premixed prevaporized (LPP) gas turbines. *Journal of Propulsion and Power*, 19:721–721, 2003.

[35] T. Lieuwen, H. Torres, C. Johnson, and B. T. Zinn. A mechanism of combustion instability in lean premixed gas turbine combustors. *Journal of Engineering for Gas Turbines and Power*, 123(1):182, 2001.

[36] T. Lieuwen and B.T. Zinn. The role of equivalence ratio oscillations in driving combustion instabilities in low NO_x gas turbines. *Proceedings of the Combustion Institute*, 27:1809–1816, 1998.

[37] T.C. Lieuwen. Phase drift characteristics of self-excited, combustion-driven oscillations. *Journal of Sound and Vibration*, 242(5):893 – 905, 2001.

[38] M.A. Macquisten and A.P. Dowling. Low-frequency combustion oscillations in a model afterburner. *Combustion and Flame*, 94(3):253 – 264, 1993.

[39] F. Magagnato, B. Pritz, H. Büchner, and M. Gabi. Prediction of the resonance characteristics of combustion chambers on the basis of large-eddy simulation. *Journal of Thermal Science*, 14:156–161, 2005.

[40] F.E. Marble and S.M. Candel. An analytical study of the non-steady behavior of large combustors. *Symposium (International) on Combustion*, 17(1):761 – 769, 1979.

[41] W. Meier, P. Weigand, X.R. Duan, and R. Giezendanner-Thoben. Detailed characterization of the dynamics of thermoacoustic pulsations in a lean premixed swirl flame. *Combustion and Flame*, 150:2–26, 2007.

[42] A. Melling. Tracer particles and seeding for particle image velocimetry. *Measurement Science and Technology*, 8:1406–1416, 1997.

[43] H. C. Mongia. TAPS - A 4^{th} generation propulsion combustor technology for low emissions. *AIAA Paper*, pages 2003–2657, 2003.

[44] H. C. Mongia, T. J. Held, G. C. Hsiao, and R. P. Pandalai. Challenges and progress in controlling dynamics in gas turbine combustors. *Journal of Propulsion and Power*, 19(5):822–829, 2003.

[45] A.S. Morgans and A.P. Dowling. Model-based control of combustion instabilities. *Journal of Sound and Vibration*, 299(1-2):261 – 282, 2007.

[46] S. Murugappan, E.J. Gutmark, S. Acharya, and M. Krstic. Extremum-seeking adaptive controller for swirl-stabilized spray combustion. *Proceedings of the Combustion Institute*, 28(1):731 – 737, 2000.

[47] H.N. Najm, O.M. Knio, P.H. Paul, and P.S. Wyckoff. A study of flame observables in premixed methane-air flames. *Combustion Science and Technology*, 140:369–403, 1998.

[48] R.D. Park. Factors affecting combustion stability. *Third Symposium on Combustion and Flame, and Explosion Phenomena*, 3(1):714 – 718, 1949.

[49] F. Parsinejad, C. Arcari, and H. Metghalchi. Flame structure and burning speed of JP-10 air mixtures. *Combustion Science and Technology*, 178:975–1000, 2006.

[50] C.O. Paschereit, E. Gutmark, and W. Weisenstein. Control of thermoacoustic instabilities and emissions in an industrial-type gas-turbine combustor. *Symposium (International) on Combustion*, 27(2):1817 – 1824, 1998.

[51] C.O. Paschereit and E.J. Gutmark. Enhanced performance of a gas-turbine combustor using miniature vortex generators. *Proceedings of the Combustion Institute*, 29(1):123 – 129, 2002.

[52] A. A. Peracchio and W. M. Proscia. Nonlinear heat-release/acoustic model for thermoacoustic instability in lean premixed combustors. *Journal of Engineering for Gas Turbines and Power*, 121(3):415–421, 1999.

[53] T. Poinsot, D. Veynante, F. Bourienne, S. Candel, E. Esposito, and J. Surget. Initiation and suppression of combustion instabilities by active control. *Symposium (International) on Combustion*, 22(1):1363 – 1370, 1989.

[54] T.J. Poinsot, A. Trouvé, D. Veynante, S. Candel, and E. Esposito. Vortex driven acoustically coupled combustion instabilities. *Journal of Fluid Mechanics*, 177:265–292, 1987.

[55] B. Pritz, F. Magagnato, and M. Gabi. Stability analysis of a coupled helmholtz resonator with large eddy simulation. In Wolfgang E. et al. Nagel, editor, *High Performance Computing in Science and Engineering '09*, pages 343–354. Springer Berlin Heidelberg, 2010.

[56] W. Pun, S. L. Palm, and F. E. C. Culick. Combustion dynamics of an acoustically forced flame. *Combustion Science and Technology*, 175(3):499–521, 2003.

[57] M. Raffel, C. Willert, and J. Kompenhans. *Particle Image Velocimetry: A Practical Guide (Experimental Fluid Mechanics)*. Springer, 2002.

[58] S.W. Rienstra and A. Hirschberg. *An Introduction to Acoustics*. 2012.

[59] V. Rodriguez-Martinez, J. Dawson, T. O'Doherty, and N. Syred. Low-Frequency combustion oscillations in a swirl Burner/Furnace. *Journal of Propulsion and Power*, 22(1):217–221, January 2006.

[60] J.M. Samaniego, F.N. Egolfopoulos, and C.T. Bowman. CO_2^* chemiluminescence in premixed flames. *Combustion Science and Technology*, 109:183–203, 1995.

[61] J.M. Samaniego, B. Yip, T. Poinsot, and S. Candel. Low-frequency combustion instability mechanisms in a side-dump combustor. *Combustion and Flame*, 94(4):363 – 380, 1993.

[62] M. Samimy and S.K. Lele. Motion of particles with inertia in a compressible free shear layer. *Physics of Fluids A*, 3:1915–1923, 1991.

[63] K.C. Schadow and E. Gutmark. Combustion instability related to vortex shedding in dump combustors and their passive control. *Progress in Energy and Combustion Science*, 18(2):117 – 132, 1992.

[64] T. Schuller, D. Durox, and S. Candel. Dynamics of and noise radiated by a perturbed impinging premixed jet flame. *Combustion and Flame*, 128(1-2):88 – 110, 2002.

[65] T. Schuller, D. Durox, P. Palies, and S. Candel. Acoustic decoupling of longitudinal modes in generic combustion systems. *Combustion and Flame*, 159(5):1921 – 1931, 2012.

[66] W.P. Shih, J.G. Lee, and D.A. Santavicca. Stability and emissions characteristics of a lean premixed gas turbine combustor. *Symposium (International) on Combustion*, 26(2):2771 – 2778, 1996.

[67] A.M. Steinberg, I. Boxx, M. Stöhr, C. D. Carter, and W. Meier. Effects of flow structure dynamics on thermo-acoustic instabilities in swirl-stabilized combustion. *AIAA Journal*, 50(4):952–967, 2012.

[68] A.M. Steinberg, I. Boxx, M. Stöhr, C.D. Carter, and W. Meier. Flow-flame interactions causing acoustically coupled heat release fluctuations in a thermo-acoustically unstable gas turbine model combustor. *Combustion and Flame*, 157(12):2250 – 2266, 2010.

[69] S.D. Stouffer, D.R. Ballal, J. Zelina, D.T. Shouse, R.D. Hancock, and H.C. Mongia. Development and combustion performance of a high pressure WSR and TAPS combustor. *AIAA Paper*, pages 2005–1416, 2005.

[70] N. Syred. A review of oscillation mechanisms and the role of the precessing vortex core (pvc) in swirl combustion systems. *Progress in Energy and Combustion Science*, 32(2):93 – 161, 2006.

[71] J. O. Uhm and S. Acharya. Role of low-bandwidth open-loop control of combustion instability using a high-momentum air jet-mechanistic details. *Combustion and Flame*, 147(1-2):22 – 31, 2006.

[72] Jong Ho Uhm and Sumanta Acharya. Control of combustion instability with a high-momentum air-jet. *Combustion and Flame*, 139(1-2):106 – 125, 2004.

[73] P. Weigand, W. Meier, X. Duan, and M. Aigner. Laser-Based investigations of thermoacoustic instabilities in a lean premixed gas turbine model combustor. *Journal of Engineering for Gas Turbines and Power*, 129(3):664, 2007.

[74] J. Westerweel. Fundamentals of digital particle image velocimetry. *Measurement Science and Technology*, 8:1379–1392, 1997.

[75] T. Yi and E.J. Gutmark. Online prediction of the onset of combustion instability based on the computation of damping ratios. *Journal of Sound and Vibration*, 310(1-2):442 – 447, 2008.

[76] K. H. Yu, A. Trouvé, and J. W. Daily. Low-frequency pressure oscillations in a model ramjet combustor. *Journal of Fluid Mechanics*, 232:47–72, 1991.

[77] K.H. Yu, T.P. Parr, K.J. Wilson, K.C. Schadow, and E.J. Gutmark. Active control of liquid-fueled combustion using periodic vortex-droplet interaction. *Symposium (International) on Combustion*, 26(2):2843 – 2850, 1996.